Non-linear finite element modelling of prestressed slab-between-girder bridge

using a 3D non-planar mesh of shell elements

M. Scheer

TU Delft

Non-linear finite element modelling of prestressed slab-between-girder bridge

using a 3D non-planar mesh of shell elements

by

M. Scheer

M. Scheer 4175530

Thesis committee:

Chair of the Committee, Supervisor	Prof. Dr. ir. M. A.N. Hendriks
Supervisor	Prof. Dr. ir. E.O.L.Lantsoght
Member of committee	ir. C. Kasbergen
Faculty:	Faculty of Civil Engineering and Geosciences, Delft

TU Delft

Preface

I would like to express my gratitude to my wife for her unconditional and endless love, patience, support and motivation. You are awesome!

I would like to thank the thesis committee for all their support and encouragement despite having so many other duties. Professor Lantsoght took up the role as daily supervisor. She gave me invaluable feedback on many different parts of the research and writing the thesis. Professor Hendriks took over as head of the thesis committee. His instructions helped me understand the difficult parts of the finite element analysis which allowed me to construct the numerical models and solve or work around certain problems. The brainstorming sessions with mr Kasbergen greatly helped with many parts of the thesis work besides being a great source of motivation for me.

Many thanks to soon to be doctor Shozab Mustafa. Supporting me was not part of your assigned work load yet you found time to give me invaluable advice and instructions on working with DIANA.

M. Scheer
Delft, June 2023

Abstract

Across the Netherlands close to 70 prestressed concrete T-beam bridges with cast-in-between slabs and transverse prestressing built in the 60's and are still in service. The current code NEN-EN 1992-1-1+C2:2011 assesses the shear capacity more conservatively. In addition, the NEN-EN 1991-2+C1:2015 prescribes an increased traffic load. This results in this type of bridge not complying with the current codes and the shear capacities are considered insufficient. However, upon inspection these bridges do not show signs of distress. This suggests the presence of additional load-carrying capacity, which is not considered in the current Eurocode.

Non-linear finite element analysis (NLFEA) can be used to accurately approximate the structural behaviour. This includes yielding of steel, cracking and crushing of concrete, the development of alternative load paths as well as snap-back and snap-through behaviour. However, performing each load step requires a great amount of computational effort depending on the amount of degrees of freedom of the model. In FEA a continuous shape is divided into discrete elements which together form a mesh. These meshes can be volumes, surfaces or lines.

To describe the geometry of the prestressed concrete T-beam bridges with cast-in-between slabs either volume elements or multiple surface meshes in different planes are required. Using a mesh of solids would result in system with such a high number of degrees of freedom which might even exceed the available computational capabilities or result in a very long duration of the analysis at best. Using shell elements to construct the mesh reduces the number of degrees of freedom by at least two thirds.

In this thesis I investigate to which extent we can simulate the structural behaviour of a prestressed T-beam slab bridge deck using a non-linear finite element model with a 3D non-planar mesh of shell elements. The Vechtbrug bridge near Muiden was a bridge of this type. A team of researchers from TU Delft have performed several collapse tests on this bridge. This includes extensive measurements of all the experiments as well as material testing on concrete and steel samples. For my own research, a single case study is conducted by recreating collapse tests performed on the Vechtbrug in which both isolated beams and unmodified spans have been loaded past failure. The results of the material tests provide accurate material properties as input for my numerical models. The results of the collapse tests allow for verification and validation of the outcome of the performed finite element analyses.

The results of the numerical analyses show a close approximation of the true collapse load with an overestimation of 15% for the isolated beam model and 12% for the cooperative beams model. The deflection again is overestimated with 18 and 56%. The deflection of the adjacent beams relative to the loaded beam is too low. The numerical model is underestimating the transverse load distribution by ± 25% for the adjacent beams and ± 34% for the beams adjacent to those. The Guyon Massonnet method was applied to estimate the transverse load distribution with the supplied material properties and including the two cross beams. By contrast, the results were an overestimation of approximately 70% for the immediate adjacent beams. In the third numerical analysis the complete bridge deck and ultimate limit state verification is performed by applying the prescribed traffic load with all safety factors applied. The bridge can withstand 234% of the prescribed load which agrees with the lack of damage present on the Vechtbrug after experiencing over 50 years of traffic load.

The results show that a non-planar shell mesh can generate a realistic structural response considering the collapse load approximates the actual one found in the collapse tests. However, this is somewhat limited for decks consisting of multiple beams since the implementation of the transverse load distribution in the numerical model was inaccurate. The structural response of the structure was too ductile in the numerical analysis with the deflection being overestimated and the strain under the loading plate double the value of the collapse test. Both Mustafa and Ensink have performed a numerical analysis of the isolated beam model using a mesh of solid elements prior to my thesis work. The results of the

isolated beam model match closely in both the results of the NLFEA performed by Mustafa and Ensink. The solid mesh does yield more realistic cracking patterns. The isolated beam model showed the required evidence to demonstrate the activation of arching action: An increase in the horizontal reaction force required to lateral restrain the beam with the bending crack occurring under the loading plate so the arch action phenomenon could be activated. In the complete deck model evidence of compressive membrane action in the transverse direction was detected. In both the complete deck models, evidence of lateral confinement was demonstrated, increasing the maximum compressive stress of the concrete.

Finally we can conclude that a NLFEA with a 3D non-planar mesh of shell elements yields accurate results when considering a single strip of the bridge deck. However, the model with a the mesh representing the complete bridge deck, the capacity of the transverse load distribution is underestimated and the structure shows overly ductile behaviour. The model is capable of including the load-carrying mechanisms arch-action, compressive membrane action and fixed boundary action as well as the effect of lateral confinement.

Contents

List of Figures

List of Tables

1 Introduction

1.1. Background and motivation

Across the nation, close to 70 prestressed concrete T-beam bridges with cast-in-situ decks are still in service today [10]. A partial typical cross section of the bridge is presented in Figure 1.1 depicting beams and prestressing in both directions. These bridges were designed to withstand the traffic loads defined in the code VOSB 1963 class 60 [28] but the current code NEN-EN 1991-2+C1:2015 [8] prescribes greater loads. In addition, the current Eurocode design code NEN-EN 1992-1-1+C2:2011 [9], is more conservative in assessing the shear resistance capacity than the the Dutch design code N 1009:1950 nl [22]. This results in bridges not complying with the current codes and the shear capacities are considered to be insufficient. However, upon inspection these bridges do not show signs of distress [10]. Evidently, the load-carrying capacity of the bridges is sufficient as has been proven in practice. This means there is a residual load-carrying capacity present which has not been taken into account by the Eurocode assessment excluding the safety margins. To determine the load-carrying capacity, a bridge deck can be loaded either to a certain threshold or till failure and it's structural response measured. Another option is to perform a (non-linear) finite element analysis to simulate the structural behaviour of the bridge.

In a non-linear analysis the load (force or displacement) is applied in steps which allows for adjusting the stiffness during the loading process. In this way, non-linear material behaviour such as yielding, cracking or crushing can be incorporated into the analysis as well as the development of additional load paths within the structure. However, performing each load step requires a significant computational effort. The time required to complete the analysis is dependant on the number of degrees of freedom of

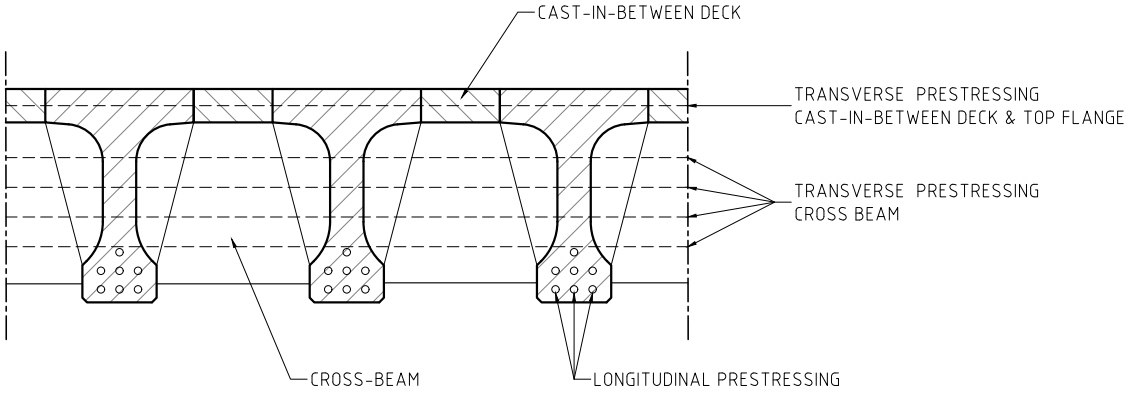

Figure 1.1: Typical cross section of prestressed T-beam bridge with cast in between deck

the mesh representing the structure. Several types of elements can be employed in creating a mesh, differing in properties such as the amount of degrees of freedom per node, the amount of nodes per element and the amount of elements required to represent the structure adequately in a numerical model.

The perpendicular beams and the slab of the bridge deck of a prestressed concrete T-beam bridges with cast in between deck cannot be represented in one single plane, requiring a non-planar mesh. The geometry of this type of bridge deck can be reproduced in detail using solid elements. The size and the amount of detail would require a high amount of elements resulting in a very high number of degrees of freedom of the system. This results in a very computationally intensive and long analysis at best, or even exceeding the available computational capacity making it impossible to run the analysis at all. With the use of shell elements, the geometry of the structure can also be approximated with a much lower amount of elements and degrees of freedom.

Performing a non-linear finite element analysis is often a complex task and sometimes a small modelling error can have significant impact on the results. The Vechtbrug bridge near Muiden was a prestressed concrete T-beam bridges with cast in between deck. A team of researchers from TU Delft have performed several collapse tests including extensive measurements of all the performed experiments [10]. Choosing this bridge for a non-linear finite element analysis (NLFEA) allows for verification of the results of the performed analysis with the results of the collapse tests.

1.2. Research objective, questions and methodology

For this thesis' research, a non-planar mesh will be constructed of shell elements representing the Vechtbrug bridge deck. The goal is to generate an accurate and realistic structural response of the Vechtbrug bridge deck under load using non-linear finite element analysis to determine the load bearing capacity. This brings us to the main research question:

To which extent can we a simulate the structural behaviour of a prestressed T-beam slab bridge deck using a non-linear finite element model with a 3D non-planar mesh of shell elements?

To perform the intended research the methodology presented in Figure 1.2 has been defined. I have chosen to do one single case study of a bridge, specifically the Vechtbrug. The main reason is that an extensive series of collapse tests and material testing has been performed on this bridge deck before being decommissioned and demolished. This allows for verification and potentially validating the results of the non-linear finite element analysis. All the numerical analyses are performed using the computer program DIANA. This advanced NLFEA software is capable of meeting all the requirements to perform a correct, numerical simulation of the structural response of the bridge deck. In addition, a literature review (see Section 2) has been performed in order to be able to correctly create the numerical models as well as interpret the results.

1.2.1. Sub-questions & methodology

To help answering the main research question, these sub-questions have been defined:

1. What are the benefits of model with a mesh of 3D solids compared to a non-planar mesh of shell elements?

   As mentioned in Section 1.1, the solid and shell elements are the options to construct the non-planar mesh. Both mr Mustafa [21] and Ensink [12] have numerically recreated the collapse test number seven of the isolated beam using a different mesh than a non-planar one using shells. As part of his master thesis research, Mustafa has created a planar mesh using plane stress elements, a planar mesh with curved shell elements, and also a non-planar mesh with solid elements. The research performed by mr Ensink also used a mesh of solid elements. By comparing the following results of their analyses and the one performed for this thesis, any (major) differences/limitations should become apparent.

- Collapse load
- Deflection
- Failure modes
- Cracking pattern

2. Which evidence of activation of the confinement effect, arch action or compressive membrane action is present?

   Confinement is the effect when principal stresses σ_2 and σ_3 both exceed the uniaxial compressive strength in the same node of the material. This causes an increase in load-carrying capacity and will be discussed in more detail in section 2.4. Arch action and compressive membrane action (see section 2.3.1) are load-carrying mechanisms. They can be activated by lateral restraint and shifting of the neutral axis towards the compressive zone of the concrete cross section which causes the formation of a compressive arch. These effects increase the load-carrying capacity of the beam/slab. The results of the numerical analysis will be investigated for sign of activation of the named phenomenons.

3. What are the effects of transverse load distribution?

   With transverse load distribution, a portion of the load is transferred to adjacent beams through the slab concrete and the cross beams. This is perhaps the most important load-carrying mechanism of the deck and if incorrectly implemented will greatly disturb the end results. The NLFEA results will be investigated to verify the implementation of this mechanism. Also, the transverse load spreading can activate compressive membrane action (see section 2.3). Finally, the transverse load distribution can be predicted by applying the Guyon Massonnet method. In addition, the transverse distribution will be verified by comparing the deflection at certain points of the adjacent beams.

4. What is the structural response of the bridge deck subjected to a full ULS traffic load?

   The current codes imply an increased load and a reduced load-carrying capacity which raises the question whether the bridge deck can carry the load with all the prescribed safety incorporated. An analysis will be performed with all the partial safety factors and modifiers of the material properties applied.

1.3. Thesis outline

The flowchart in Figure 1.2 shows the structure of the research work of this thesis as well as it's documentation.

Chapter 1 Introduction
In the first chapter the background and motivation, research objectives and methodology is addressed.

Chapter 2 Literature review
In the chapter "Literature review" the theoretical preparation is documented. The properties of elements to be used in the meshes are discussed. The implementation of the GRF safety format for Eurocode ultimate limit state verification is documented. Other included topics are the development of snap-back mechanisms that can introduce alternative load paths, the lateral confinement effect and structural failure mode.

Chapter 3 Vechtbrug
In this chapter illustrates the geometry of the Vechtbrug bridge deck. Also, the performed collapse load test experiments are discussed as well as the determination of material properties of the concrete and steel used in the structure.

Chapter 4 Non-linear finite modelling
The process of creating the different numerical models is presented including the motivations of design choices. This includes the different analysis configurations and creation of loading sequences. The structure of the guidelines [13] is followed in this chapter in order to demonstrate the compliance for the analyses.

Chapter 5 Results
This section details the processing and analysis of the results of the performed numerical analyses using the non-planar shell mesh. The results are both verified/validated using the experimental data of the recreated tests and are also compared with the numerical analyses performed by Mustafa and Ensink which make use of different meshes.

Chapter 6 Conclusions
The determined answers to the research questions are presented and recommendations for further research will be given.

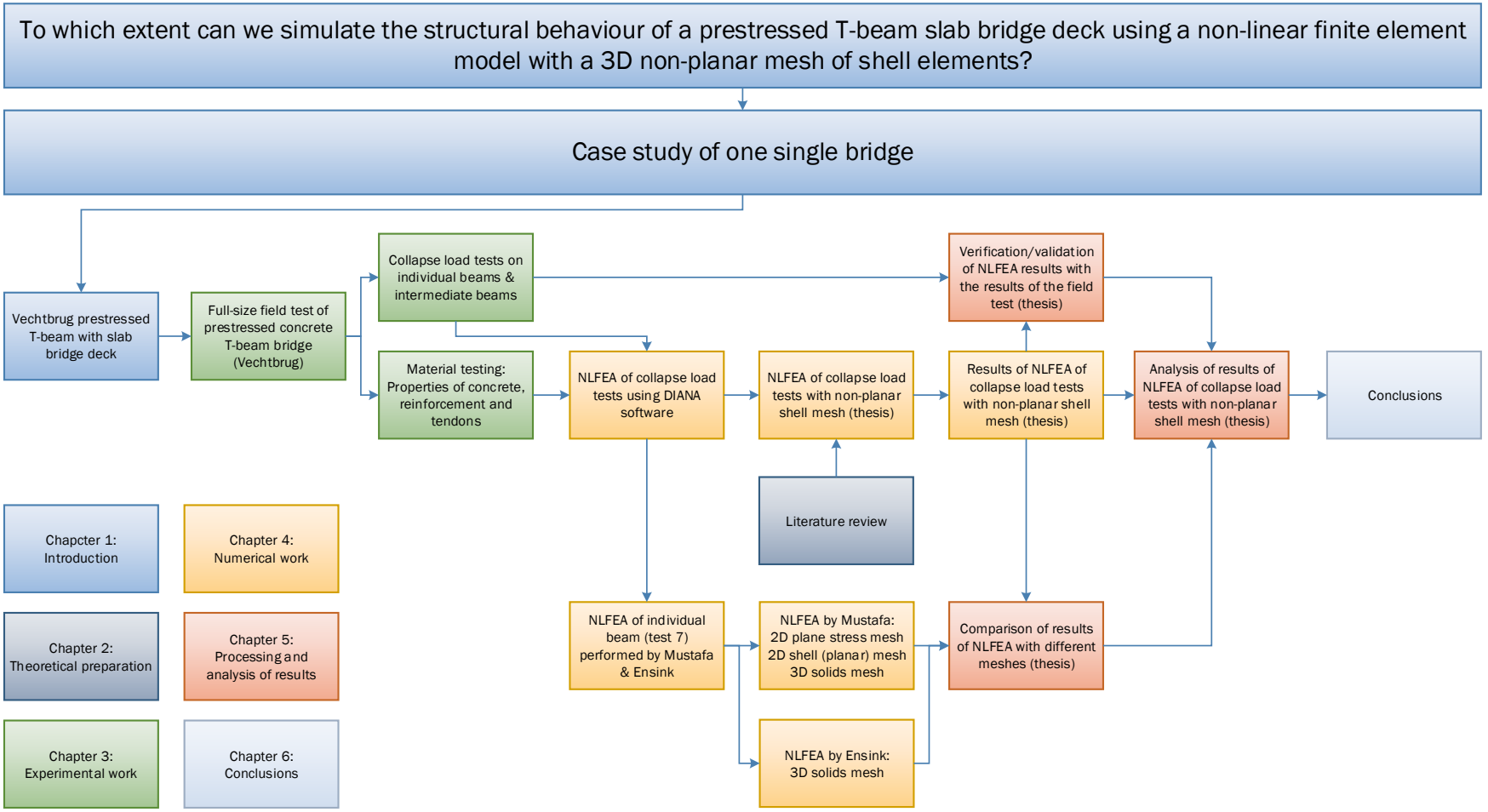

Figure 1.2: Flowchart of the research methodology.

2

Literature review

A literature review has been conducted to address the knowledge, results and conclusions of other studies relevant for this research.

2.1. Properties of solid and shell elements

Two type of elements are suitable to construct the non-planar mesh which are shell and solid elements.

2.1.1. Regular curved shells elements

Flat and curved shell elements are available in DIANA. Flat shell elements cannot be used because they can only accommodate linear elasticity [20] and not non-linear elasticity, plasticity or cracking. The regular curved shell element is selected because the other options do not suit this type of analysis. The nodes of a regular curved shell element have five variables/degrees of freedom: the translations u_X, u_Y and u_Z in the global XYZ directions and the rotations ϕ_x and ϕ_y respectively around the local $+x$ and $+y$ axes in the tangent plane [11]. See equation 2.1 and figure 2.1 [11].

$$\mathbf{u}_e = \begin{pmatrix} u_X \\ u_Y \\ u_Z \\ \phi_x \\ \phi_y \end{pmatrix} \tag{2.1}$$

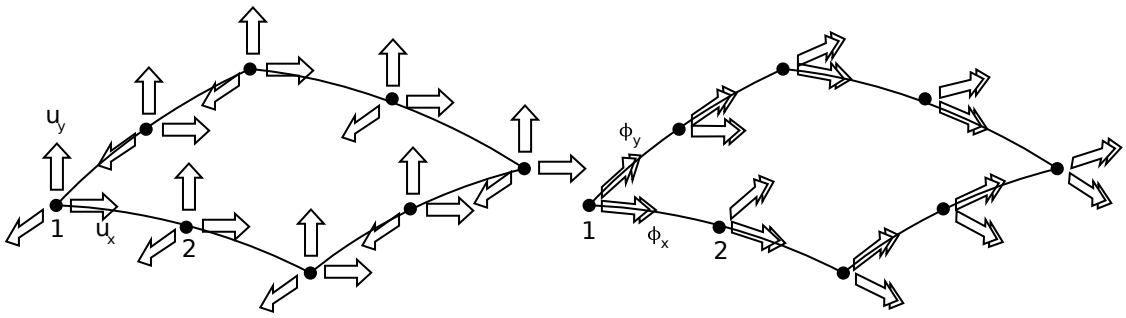

(a) Displacements **(b)** Rotations

Figure 2.1: Degrees of freedom of a curved shell element [11]

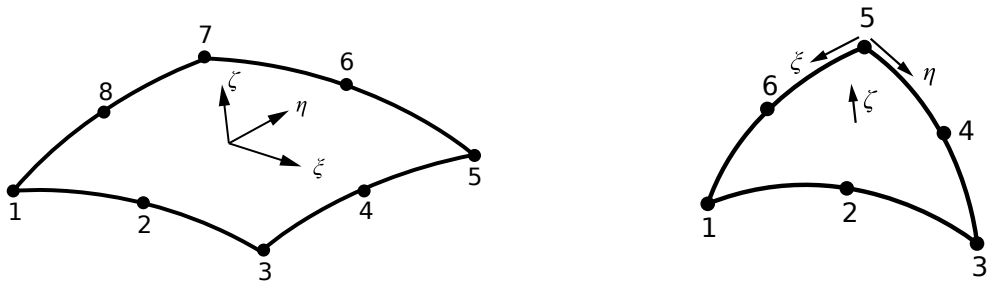

(a) CQ40S **(b)** CT30S

Figure 2.2: Regular curved quadratic quadrilateral and triangular shell elements

2.1.2. Solid elements

The nodes of a solid element have three variables/degrees of freedom: the translations u_x, u_y and u_z in the local xyz directions. See equation 2.2 and figure 2.3 [11]. No degree of freedom is available to describe a rotation so a single node of a solid cannot transfer curvature/moments. Moments are transferred to neighbouring solid elements through stresses and can be transferred to shells perpendicular to a solids face by tying the curvature of the face of the solid to row of nodes.

$$\mathbf{u}_e = \begin{pmatrix} u_x \\ u_y \\ u_z \end{pmatrix} \tag{2.2}$$

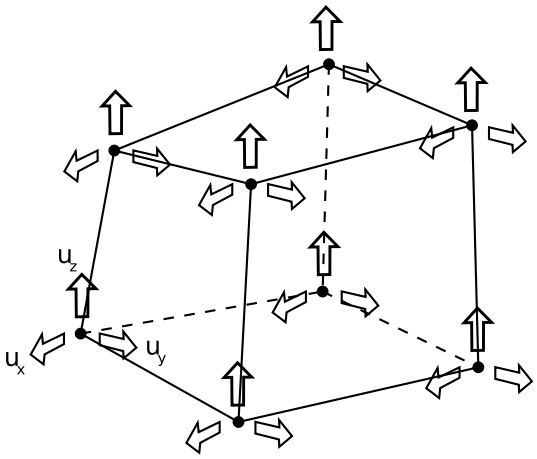

Figure 2.3: Degrees of freedom of a solid element

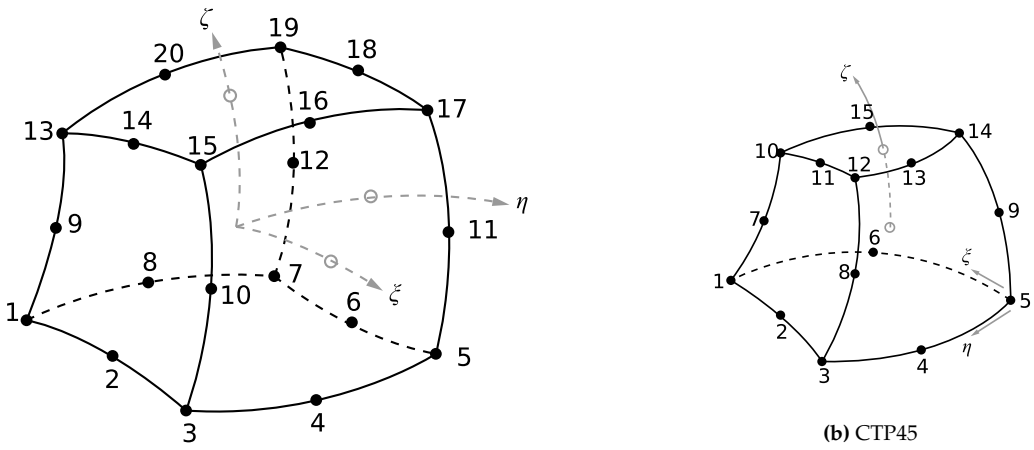

(a) CHX60

(b) CTP45

Figure 2.4: Hexagon and triangular prism shaped solid elements

2.2. Eurocode ULS assessment and NLFEA with GRF

In a regular ULS analysis, design values are used for material properties and the loads are increased by multiplying with the appropriate partial load factor. However, when using NLFEA the Eurocode (NEN-EN 1992-2+C1:2011 article 5.7) prescribes the application of the global resistance factor (GRF) to obtain the design resistance. The application of this safety format involves a modification of material properties as well as an increase of the applied loads. "On the application of the Global Resistance Factor (GRF) method" [1]" describes this procedure in determining the material safety factors and the partial load safety factor. The actual determination and application of the GRF is documented in Section 4.10.

2.3. Load-carrying mechanisms

The research goal of the field test [10] was to quantify additional load-carrying mechanisms currently not included in the assessment. Under load, these load-carrying mechanisms can be activated in a structure and more than one can be active simultaneously. These mechanisms occur on a local scale, e.g. in a single slab, beam or part of a beam but can occur at multiple locations at once. A properly configured numerical model should be able to include these load-carrying mechanisms and therefore approximate the results of the field tests much closer than the analytical assessment. Two kinds of restraining action can be distinguished: compressive membrane action (CMA) and fixed boundary action (FBA). Both are presented in Figure 2.5 [2]. Arch action is the CMA phenomenon occurring in a beam in the longitudinal direction.

2.3.1. Compressive Membrane Action

Loading the slab (see Figure 2.5a) causes cracking due to tensile failure of the concrete if the tensile strength is lower than the compressive strength of the slab. If lateral restraints are present at the supports the slab only displaces vertically and extension is prevented. This causes the neutral axis to shift towards the compressive zone and the formation of a compressive arch which causes an increase in the flexural and punching shear capacity. This phenomenon cannot occur in slabs with the same strength in tension and compression. With equal tensile and compressive strength, the slab would fail simultaneously in tension and compression at the onset of cracking. Also, the presence of reinforcement is not necessary. [2]. CMA can be activated in both directions if the lateral restraint is also present in both directions. In slabs the lateral restraint can also partly be created by shear stresses between the adjacent beams.

2.3.2. Fixed Boundary Action

Fixed boundary action is extremely similar to CMA. It can develop in both uncracked and cracked slabs and beams (provided that the tensile reinforcement is present at the boundaries) and is due to the

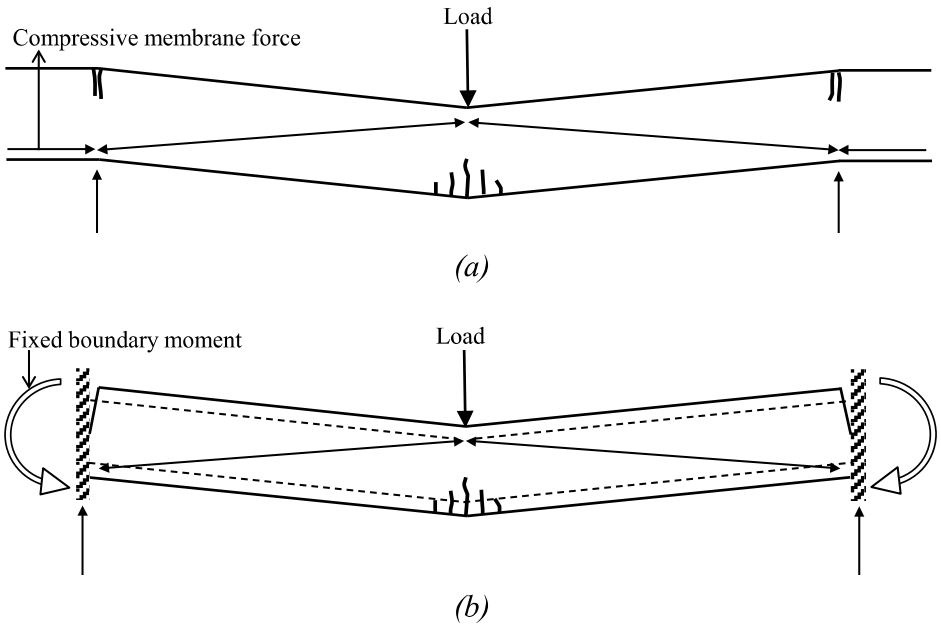

Figure 2.5: Idealized restrained slab a) Compressive membrane action; b) Fixed boundary action.

moment restraint only (see Figure 2.5b). Contrary to the CMA, this phenomenon can occur in slabs and beams with the same tensile and compressive strengths. [2]. Both CMA and FBA prevent rotation of the cross section at the support by preventing extension and exerting compressive stresses on the slab and also tensile stresses if reinforcement is present at the support causing an increase in normal force at the slab boundaries. This is an effect similar to an anchor of a prestressed tendon would have.

2.3.3. Analytical and Numerical Study of Arch Action in T-beam Bridges

The thesis of Shozab Mustafa [21] focuses on the development of arch-action in single T-beams acting as part of a bridge system. His work consists of two parts. In the first part analytical analysis is conducted with numerical verification. In the second part several type of numerical models of the field test experiments are created and validated using the tests results. His 2.5D shell model is the starting point of my work in DIANA. His thesis and his personal feedback helped me understand the concepts of CMA and arching action as well as some of the complex parts of setting up a correct, working numerical model.

2.3.4. Transverse (re)distribution

Transverse load distribution is a load-carrying mechanism in which a part of the load is distributed in the transverse direction to the adjacent bridge deck and T-beam. Redistribution can take place after cracking of the concrete.

2.4. Effect of lateral confinement

Concrete loaded uniaxially in compression will expand perpendicular to the direction of the applied load and generate tensile stresses and strains limiting the compressive load the concrete specimen can carry. The lateral expansion can be limited internally by increasing it's resistance to tensile stresses and strains or externally by applying a lateral compressive load to reduce the tensile stresses within the specimen. By increasing the resistance to lateral tensile stresses, a higher compressive strength can be achieved resulting in a greater load-carrying capacity.

2.4.1. Behaviour of concrete under biaxial stresses

This study [19] conducted by Kupfer et al. contains a literature review of previous experiments on biaxial stress states in concrete and describes and demonstrates the possible increase of the maximum principle stresses under biaxial loading. In Figure 2.6 the results of the experiments of three types of plain concrete are shown and fitted with the Drucker-Prager failure surface [11]. The results demonstrate that the maximum compressive principle stress exceeds the uniaxial compressive strength by about 25%.

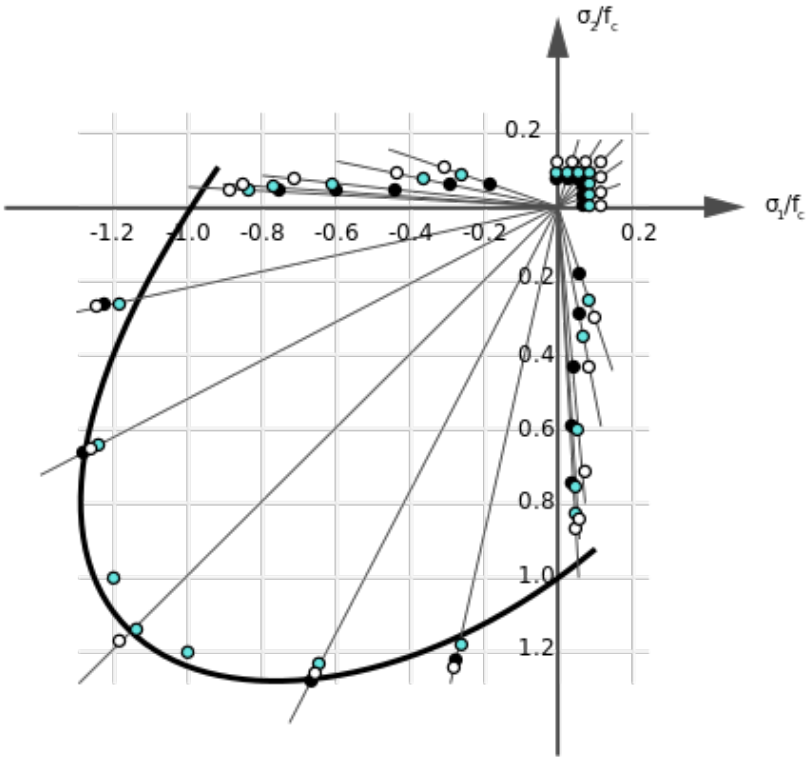

Figure 2.6: Results of experimental investigation with a biaxial fit of the Drucker-Prager failure surface

2.4.2. Selby and Vecchio stress confinement model

In the numerical model in DIANA the confinement effect of concrete is realized with the application of the Selby and Vecchio stress confinement model [27]. The stress tensor $\boldsymbol{\Sigma}$ can be represented in terms of the principal stress tensor in the 1-2-3 coordinate system:

$$\boldsymbol{\Sigma}_{123} = \begin{bmatrix} \sigma_1 & 0 & 0 \\ 0 & \sigma_2 & 0 \\ 0 & 0 & \sigma_3 \end{bmatrix} = \underbrace{\begin{bmatrix} p & 0 & 0 \\ 0 & p & 0 \\ 0 & 0 & p \end{bmatrix}}_{isotropic} + \underbrace{\begin{bmatrix} \sigma_1 - p & 0 & 0 \\ 0 & \sigma_2 - p & 0 \\ 0 & 0 & \sigma_3 - p \end{bmatrix}}_{deviatoric} \tag{2.3}$$

The isotropic stress causes a change in volume and the deviatoric stress a change in shape. With the isotropic or hydrostatic stress p defined as:

$$p = \frac{1}{3}(\sigma_1 + \sigma_2 + \sigma_3) \tag{2.4}$$

The DIANA documentation (47.5.6.6 Compressive Behavior with Lateral Confinement) [11] describes the application of the Selby and Vecchio stress confinement model [27]. The increase of the strength with increasing isotropic stress is modelled with the four-parameter Hsieh-Ting-Chen failure surface [16]:

$$f = 2.0108\frac{J_2}{f_{cc}^2} + 0.9174\frac{\sqrt{J_2}}{f_{cc}} + 91412\frac{f_{c1}}{f_{cc}} + 0.2312\frac{I_1}{f_{cc}} - 1 = 0 \tag{2.5}$$

with:

$J_2 = \frac{1}{6}\left((\sigma_{c1} - \sigma_{c1})^2 + (\sigma_{c2} - \sigma_{c3})^2 + (\sigma_{c3} - \sigma_{c1})^2\right)$	Second invariant of the deviatoric stress tensor
$f_{c1} = max(\sigma_{c1}, \sigma_{c2}, \sigma_{c3})$	Maximum concrete principle stress
f_{cc}	Concrete uniaxial compressive strength
$I_1 = f_{c1} + f_{c2} + f_{c3}$	First invariant of the stress tensor

The stress f_{c3} is assumed to result in failure and is determined by scaling the linear elastic stress vector $\sigma_c = sE\epsilon_{nst}$ such that equation 2.5 holds. The failure strength f_{cf} is given by:

$$f_{cf} = -f_{c3} = s \cdot min(\sigma_{c1}, \sigma_{c2}, \sigma_{c3}) \tag{2.6}$$

The peak stress factor K_σ:

$$K_\sigma = \frac{f_{cf}}{f_{cc}} \geq 1 \tag{2.7}$$

For confined concrete, the peak strain K_ϵ increases much more rapidly than the peak stress K_σ as confining pressure is increased [27]. To relate the peak stress factor and the strain at peak stress, a two-part expression is implemented, equations 2.8 and 2.9. For low peak stress ratios ($K_\sigma < 3$), a fit to the data of Kupfer et al. (1969) is used: The peak strain factor K_ϵ:

$$K_epsilon = 0.2036K_\sigma^{4\check{}}2.819K_\sigma^3 + 13.313K_\sigma^2 - 24.42K_\sigma^4 + 13.718\sqrt{K_\sigma} + 1 \tag{2.8}$$

$$K_\epsilon = 5K_\sigma\check{}4 \tag{2.9}$$

These relations are not mentioned in the DIANA manual [11] and instead the following peak stress - peak strain relation is given in equation 47.137:

$$K_\epsilon = K_\sigma \tag{2.10}$$

2.5. Failure modes

Structural failure of concrete beams can be classified into two types, flexural failure and shear failure. In Figure 2.7 the typical crack pattern for several failure modes is presented.

2.5.1. Flexural failure

Flexural failure occurs when the steel in the beam is yielding, followed by crushing of the concrete in the compressive zone occurs. The ductility of the reinforcement allows for a gradual failure. The crack pattern of this failure mode shows cracks extending into the compressive zone of the beam. Flexural compression is the opposite failure mode. The steel does not yield before crushing of the concrete, resulting in a sudden (no warning signs), brittle failure. The accompanying crack pattern mostly shows crushed concrete in the compressive zone.

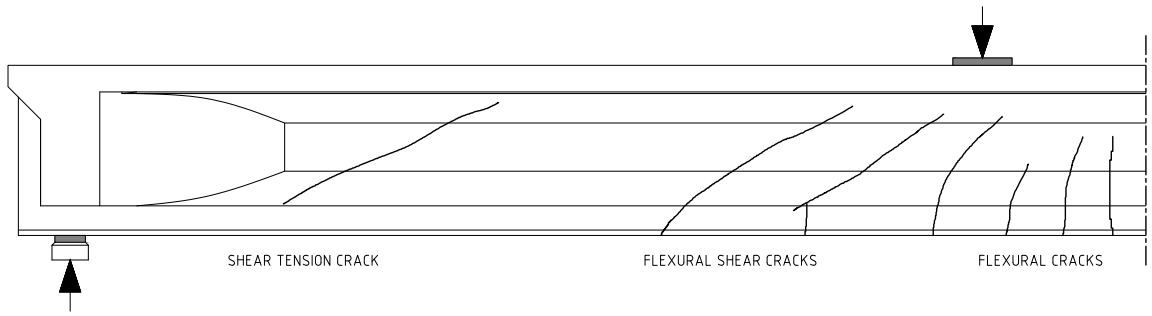

Figure 2.7: Typical crack pattern for shear tension, flexural shear and flexural failure modes

2.5.2. Shear failure

A common property of all shear failure modes is that they are brittle failures. Flexural shear failure occurs when a vertical flexural crack develops into a single, diagonal shear crack towards the point of application of the load. Shear tension failure is quite similar but the shear crack will develop without the initial bending crack. With shear compression failure crushing of the concrete of the compressive strut within the beam occurs.

Punching shear failure is a combined action of flexure and shear load resulting in combined flexural, radial and inclined shear cracking. The angle of inclination is dependant on the reinforcement ratio which influences the angle of the punching cone. The vertical flexural and inclined shear cracking is commonly grouped as tangential cracking [2]. The dissertation of dr. Amir gives the detailed description of the development of a punching shear failure:

1. Initially, at low load levels, flexural cracks develop at the bottom of the slab directly under the projection of the load, within and around the loading perimeter.
2. Next, radial cracks, caused by tangential moments, spread out from the perimeter of the load projection, dividing the slab into fan-like segments.
3. At further loading, inclined shear cracking, caused by the radial moments, forms from the tangential cracks, and starts building up a cone-like plug.
4. At higher loads, the inclined cracks extend towards the slab edges and appear around the loaded perimeter. For some time, the Crack width are found to increase with very few new cracks and then failure occurs suddenly and in a very brittle manner when the concrete plug is pushed out of the slab at the ultimate punching load.

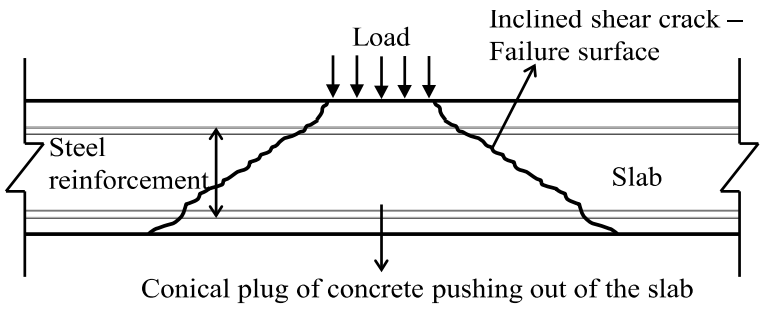

(a)

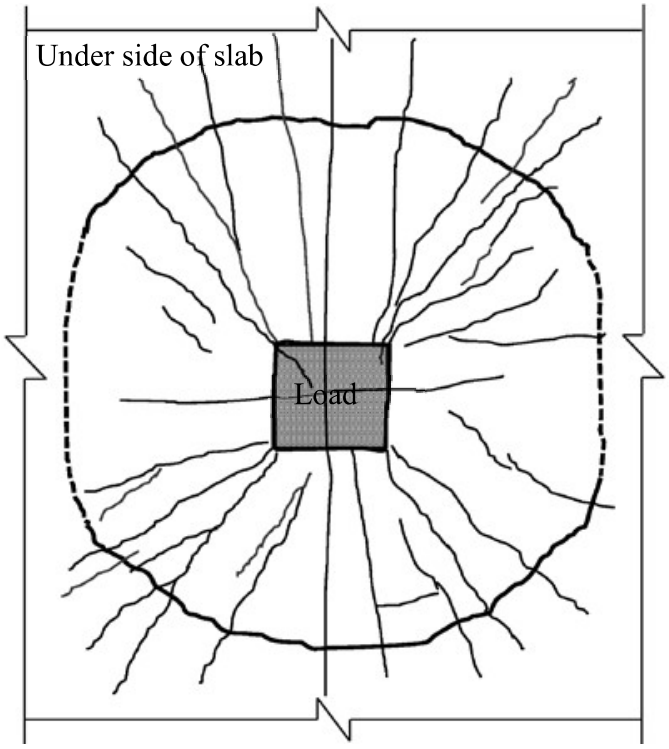

(b)

Figure 2.8: Typical punching shear cracking pattern: a) Punching shear cone in cross section; b) Crack pattern in plan. [2]

3

Vechtbrug

The Vechtbrug is the subject of the case study for the thesis research. In this chapter, the geometry of the bridge deck, the mentioned field tests and the derivation of the material properties will be discussed. Figure 3.1 [6] shows the bridge under construction displaying the separate T-beams on the spans where the slab concrete hasn't been poured yet. Figure 3.2 shows the bridge in use with the addition of the two lane expansion with alternating driving directions [15].

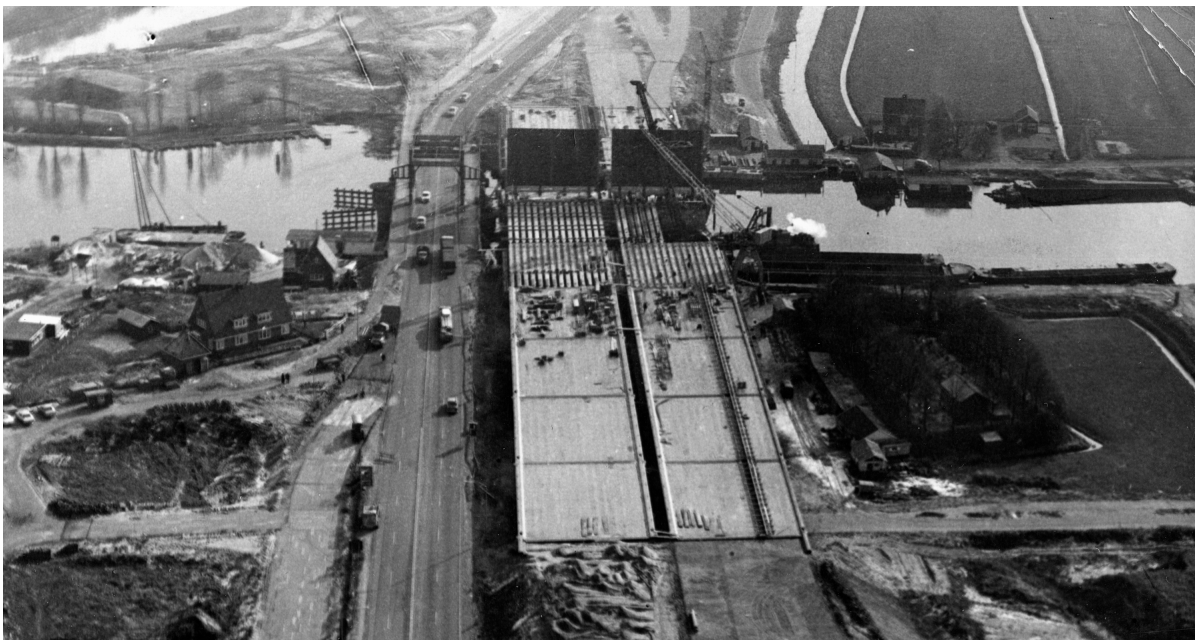

Figure 3.1: Vecht bridge under construction in 1965 [6]

Figure 3.2: Vechtbrug in use in 2011 [15]

3.1. Geometry

All the dimensions of the geometry were provided by the original design drawings (see Table 3.1) of the bridge deck for both the concrete, reinforcement, prestressing steel and the rubber/steel load bearing pads between the T-beam and the concrete support structure. The structure of a single span of the bridge deck consists of fifteen longitudinally prestressed T-beams with a length of 24,7 m interconnected every eight meters by a cross beam. The beam has a rectangular profile on each end which changes into the T-shape moving toward the centre. Each beam end is supported by a load bearing pad. Cast-in-situ concrete is cast between the beams forming a continuous deck. Both longitudinal and transverse prestressing is applied over the entire length of the span. Figure 3.3 shows a partial top view with the location of the loading plate of the field test experiment. Figure 3.4 shows cross section A-A′ in the longitudinal direction through the cast-in-situ deck with the side view of the T-beam with the location of the applied point load and the support. Figure 3.5 shows cross section B-B′ in the transverse direction with the location of the applied point load with the side view of the cross beam.

Table 3.1: Design drawings

Drawing number	Subject
C9728	Kabelverloop voorgespannen liggers
C9747	Zachtstaal wapening voorgespannen liggers
C10444	Maten brugdek
C10880	Zachtstaal wapening brugdek
C11238	Rubberoplegging

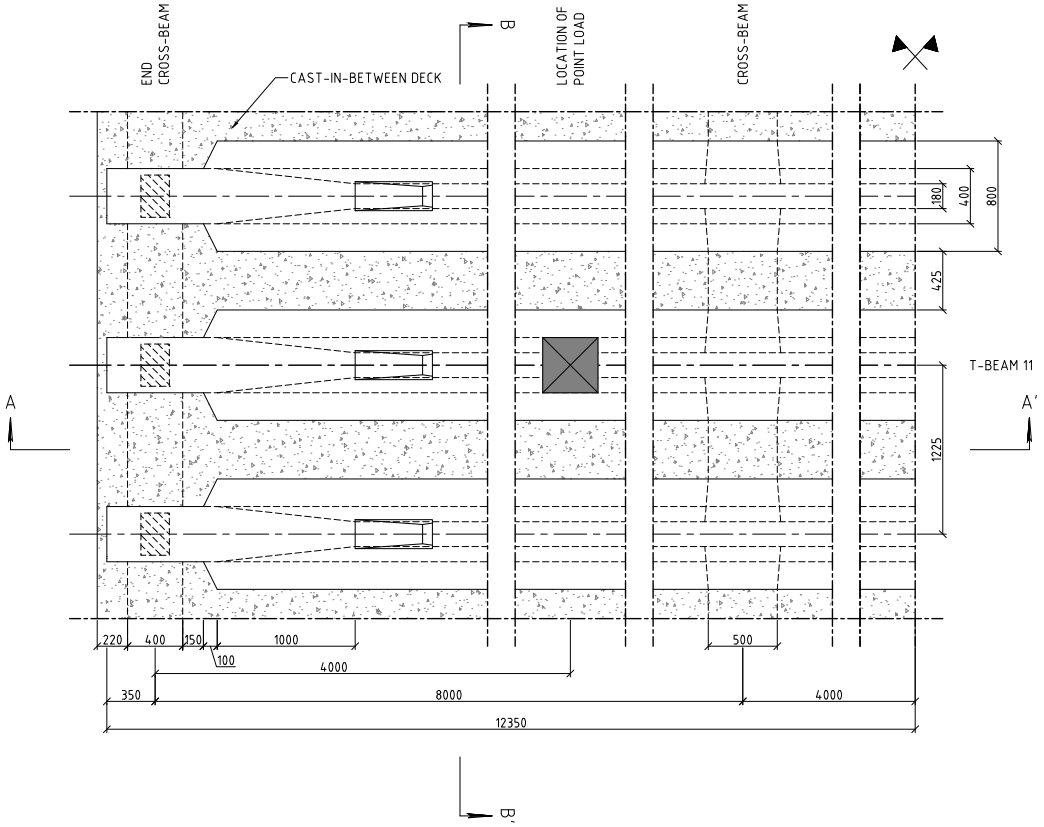

Figure 3.3: Partial top view of bridge deck span four

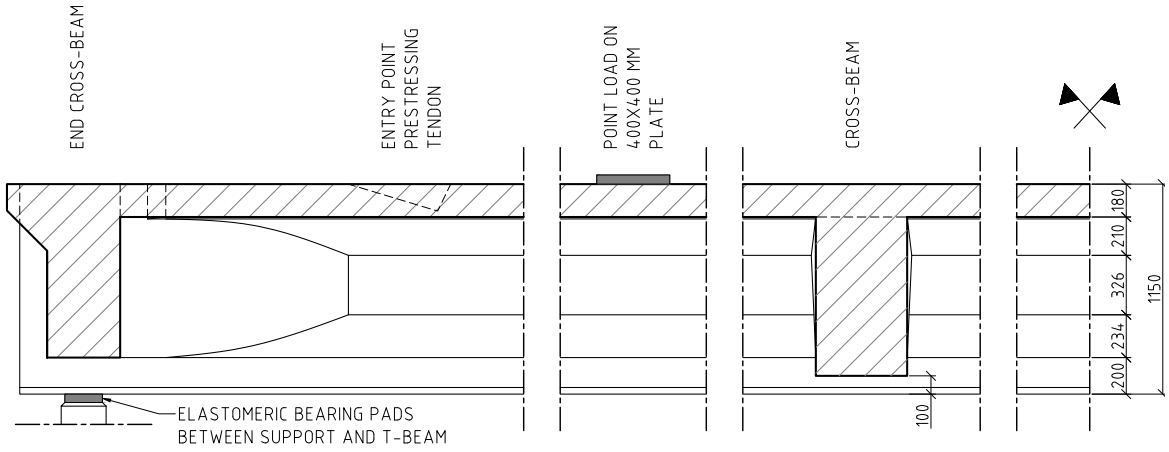

Figure 3.4: cross section A-A′ of bridge deck

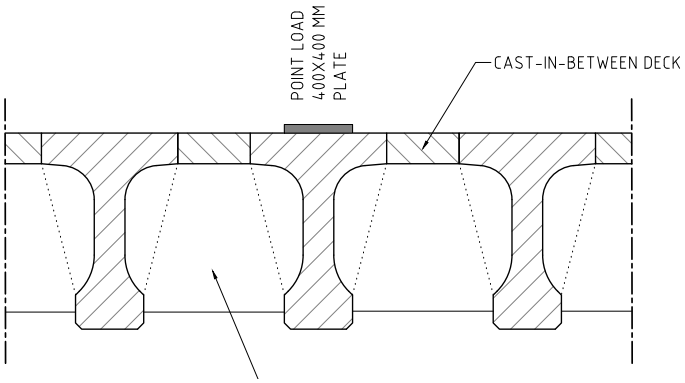

Figure 3.5: Partial cross section B-B′ of bridge deck

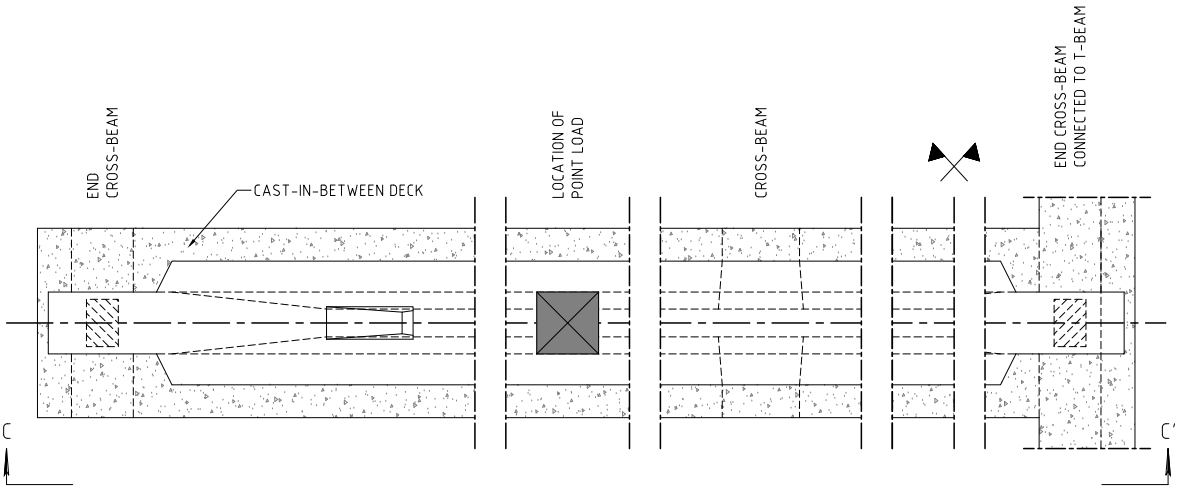

Figure 3.6: Top view of single beam connected to end-beam on right hand side

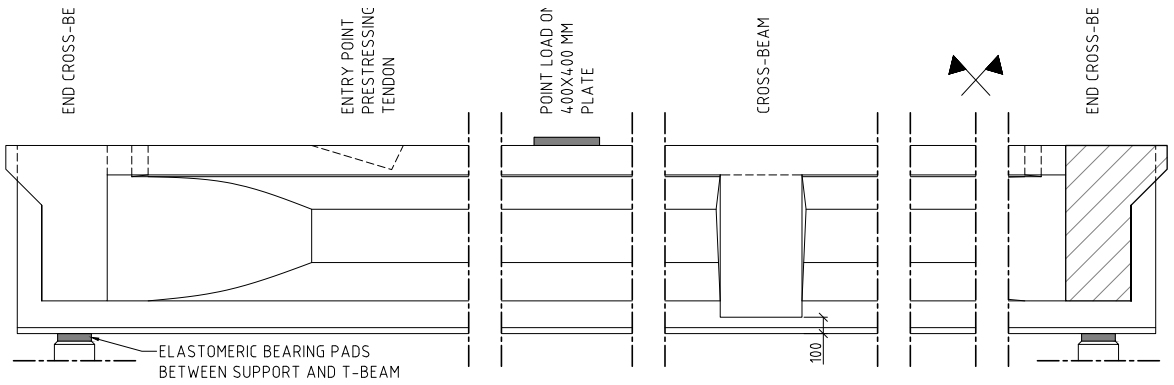

Figure 3.7: Side view C-C′ of single beam connected to end-beam on right hand side

3.2. Collapse load tests

"Measurement Report Loading of Vechtbrug (25H-100). Stevin Report 25.05-17-03" [18] documents in detail all the planned and performed failure tests. Table 3.2 lists all the performed collapse tests. Tests one to three were performed on a complete, unmodified concrete span (span four), see Figure 3.8.

Table 3.2: Overview of performed tests

Test numer	a [mm]	Type of test
1	4000	Cooperation tests on centre beam
2	2250	Cooperation tests on centre beam
3	2550	Cooperation tests on edge beam
4	2250	Individual test on centre beam
5	2250	Individual test on centre beam
6	2250	Individual test on centre beam
7	4000	Individual test on centre beam

Tests four to seven were performed on single, isolated beams (see Figures 3.6 and 3.7) apart from the remaining connection to the end cross beam in order to retain stability of the beam during testing (span two)(see Figure 3.9). The loading plate used in all experiments is a steel plate with dimensions of 400 x 400 x 100 mm and is placed on top of plywood on top of a layer of sand on the concrete girder to prevent localisation of stresses. The applied load was increased in 500 kN steps for the cooperative beams and 100 kN steps for the single, isolated beams till collapse of the structure. Two points of application of the load were selected:

1. 2.25 m centre-to-centre from the support. This location was selected because it is just beside the end of the hammer piece, and thus shear stresses are the highest [18].
2. 4.0 m centre-to-centre from the support. This location is in the middle of two cross beams allowing for maximal deflection so (in case of cooperative beams) cooperation between neighbouring girders can possibly develop [18].

3.2.1. Measurements

During all the tests, several quantities were continuously measured. Their respective locations and measurement tools are depicted in Figure 3.10. The vertical deflection at the support plates and below the loading plate are also measured at the two adjacent beams on both sides for collapse test 1. In addition, the vertical deflection was measured at the bottom of the cross beam.

3.2.2. Determination of material properties

Steel

Steel and concrete samples were collected from the span three to undergo laboratory testing to determine their mechanical properties. The results of the tensile tests for prestressing steel are presented in Figures 28 to 31 and for reinforcement figures 32 to 34 of the measurement report [18] and are summarized in Table 4.3. The ultimate strain values in the table are the conservative average of these test results and will be used as input in the numerical models.

Concrete

"Proof loading bridge "Vecht Bridge A1" - Material research concrete compressive strength" [7] presents the results of extensive concrete compressive testing of the extracted samples of the bridge deck and the calculation of the material properties of the two types of concrete used in the structure. Concrete samples were taken from the T-beam's top flange, web and bottom flange in addition to samples of the slab concrete. This resulted in a mean compressive concrete strength for the girder of $9{,}0 \cdot 10^9$ N/m^2 and $6{,}2 \cdot 10^9$ N/m^2 [21] and will be used as input for the numerical models.

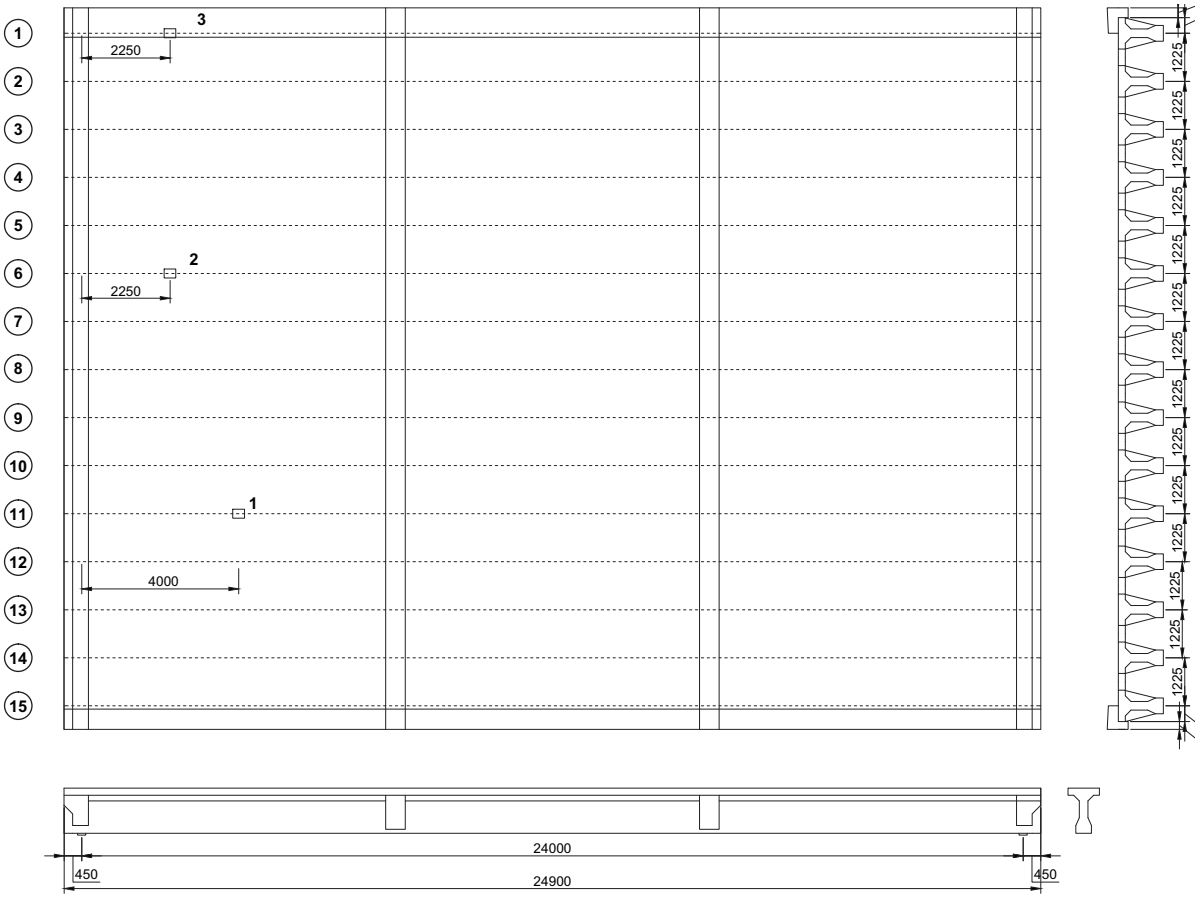

Figure 3.8: Top and side view of span 4, test locations for test 1, 2 and 3

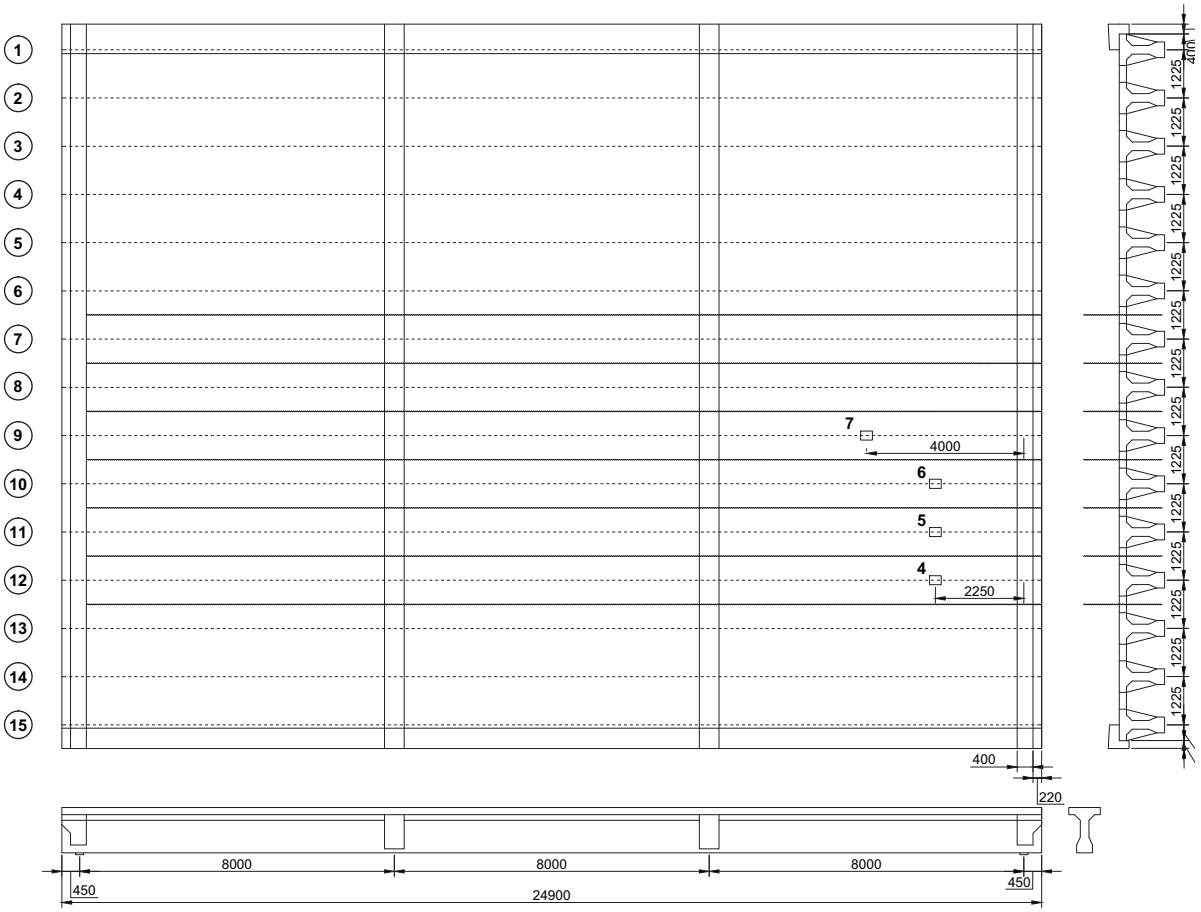

Figure 3.9: Top and side view of span 2, test locations for test 4, 5, 6 and 7 with cutting lines

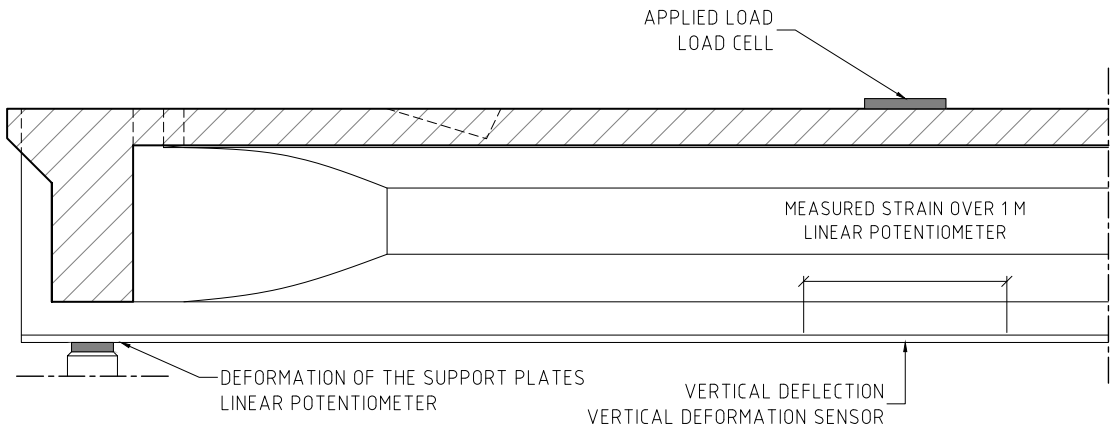

Figure 3.10: Type and location of the measurements performed as part of the field test

3.2.3. Failure modes

Punching shear was the primary failure mode in collapse test 1 (Cooperation tests on centre beam) of the Vechtbrug field test, immediately followed by a regular shear failure. Shear failure was the failure mode for collapse test 7 (Individual test on centre beam).

4

Non-linear finite element analysis

4.1. Guidelines for non-linear finite element analysis of concrete structures

The "Guidelines for non-linear finite element analysis of concrete structures" [13]. and "Validation of the guidelines for non-linear finite element analysis of concrete structures" [3] is developed *based on scientific research, general consensus among peers, and a long-term experience with nonlinear analysis of concrete structures by the contributors.*. Non-linear finite element analyses have intrinsic model and user factors that influence the results. The document provides guidelines to reduce these factors and to improve the robustness of non-linear finite element analyses [13]. It has been my primary scientific basis for decision making setting up my numerical models. In addition the structure of the guidelines is followed to document the configuration of the models and analyses.

4.2. Analyses

The numerical modelling of the case study consists of three analyses: the recreation of collapse tests 7 (see Figure 3.9) and 1 (see Figure 3.8) and an ultimate limit state analysis of the deck loaded by the traffic load gr1a. Each analysis have been given a short name in Table 4.1 for convenient referencing.

Table 4.1: Analyses name abbreviations

Model name	Collapse test	Geometry	Load	Safety factors
IBCL	Test 7	Isolated beam with clamped end	Single concentrated load	-
CDCL	Test 1	Complete deck	Single concentrated load	-
CDTL	N/A	Complete deck	ZOAB UDL, EC traffic load gr1a	ULS + GRF

4.2.1. IBCL

In the finite element model the isolated beam and slab are represented by of straight surfaces (see Figure 4.1). Rectangular volume elements are used for the connection to the end beam of the bridge deck at the right hand side of the model. Four meters centre to centre relative to the left hand side support is the location of the concentrated applied load. The applied load of the collapse test is represented as a quadrilateral load with an increased dimension to incorporate the downward dispersal of the load into the deck.

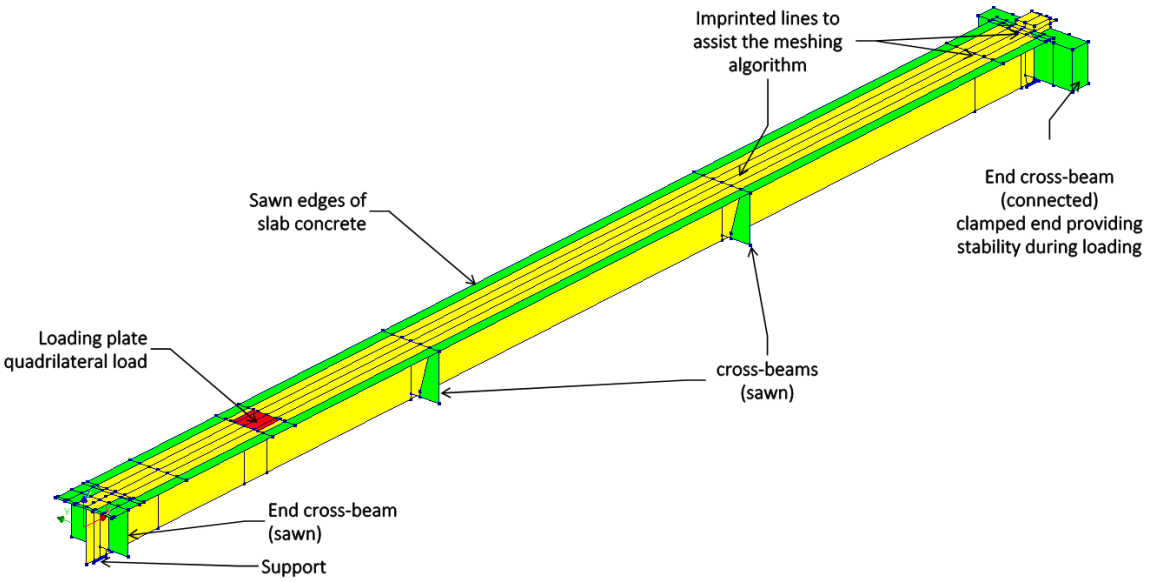

Figure 4.1: Isometric view of the isolated beam model with concentrated applied load

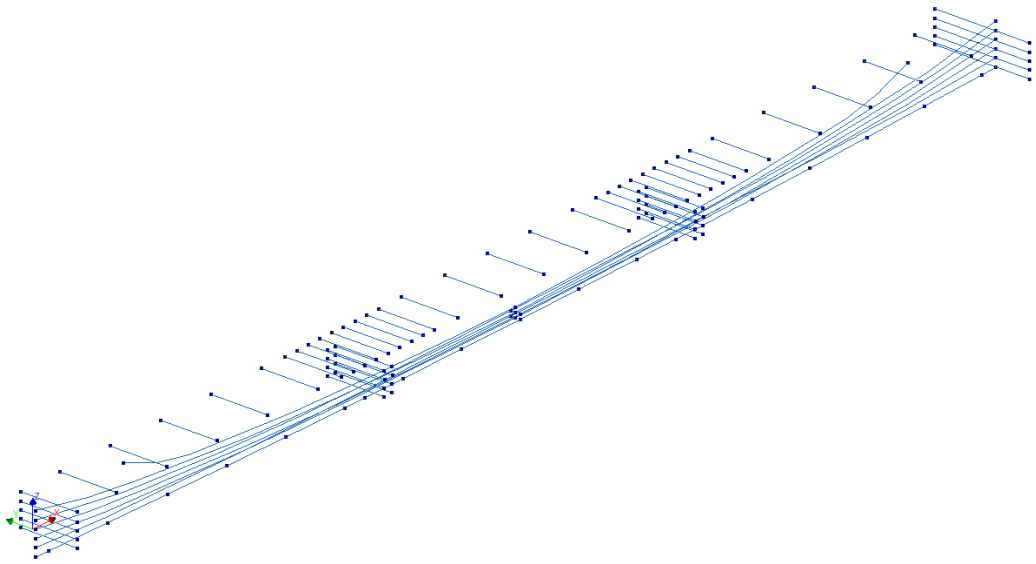

Figure 4.2: Isometric view of the prestressing tendons in both directions of the IBC model

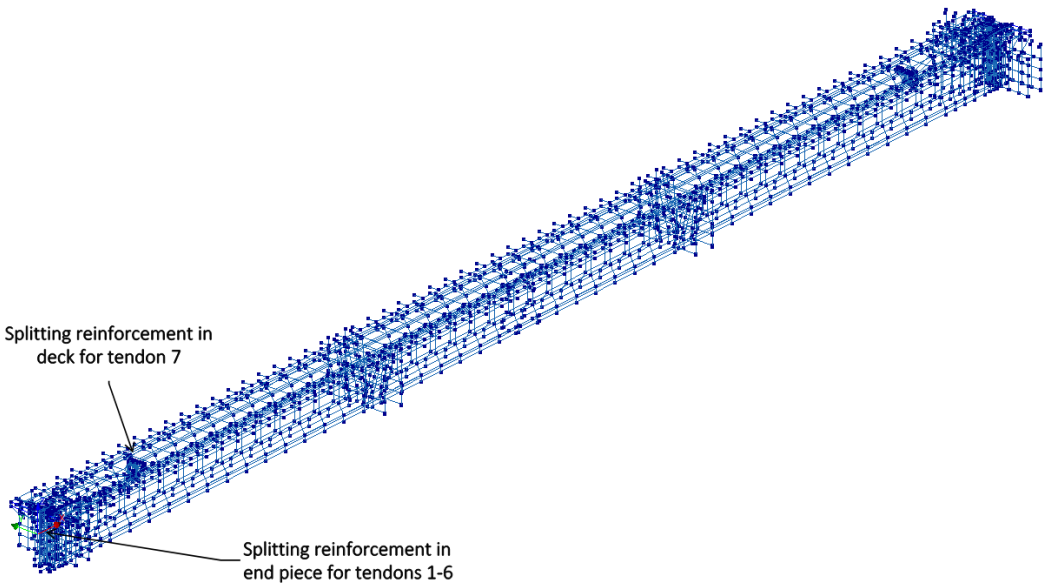

Figure 4.3: Isometric view of the reinforcement of the IBCL model

An interface between the T-beam and the support is configured to represent the elastic properties of the load bearing pads (see 4.11). Several straight lines were imprinted on the surfaces to assist the meshing algorithm creating the mesh. In Figure 4.2 the curved profile of the longitudinal tendons is presented as well as the transverse tendons. In Figure 4.3 the splitting reinforcement can be seen at the locations when the prestressing force is introduced into the concrete.The mesh (see 4.4) consists of over 6000 elements and can be considered almost completely structured with only 20 triangular elements. The depth of the surface elements is accomplished in the mesh by assigning functions defining the thickness depending on z or z and x. See Figure 4.5

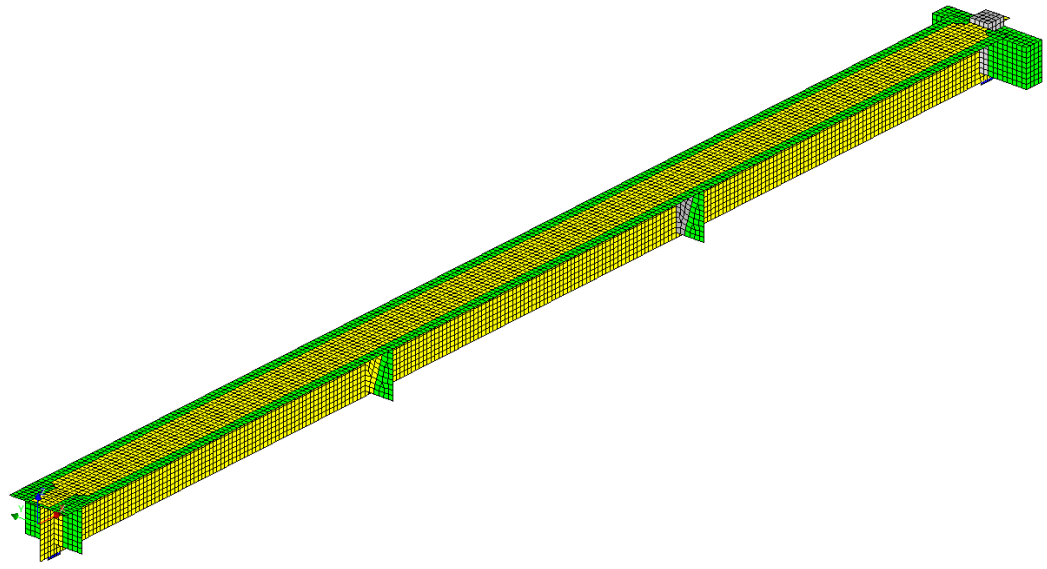

Figure 4.4: Isometric view of the mesh of the IBCL model

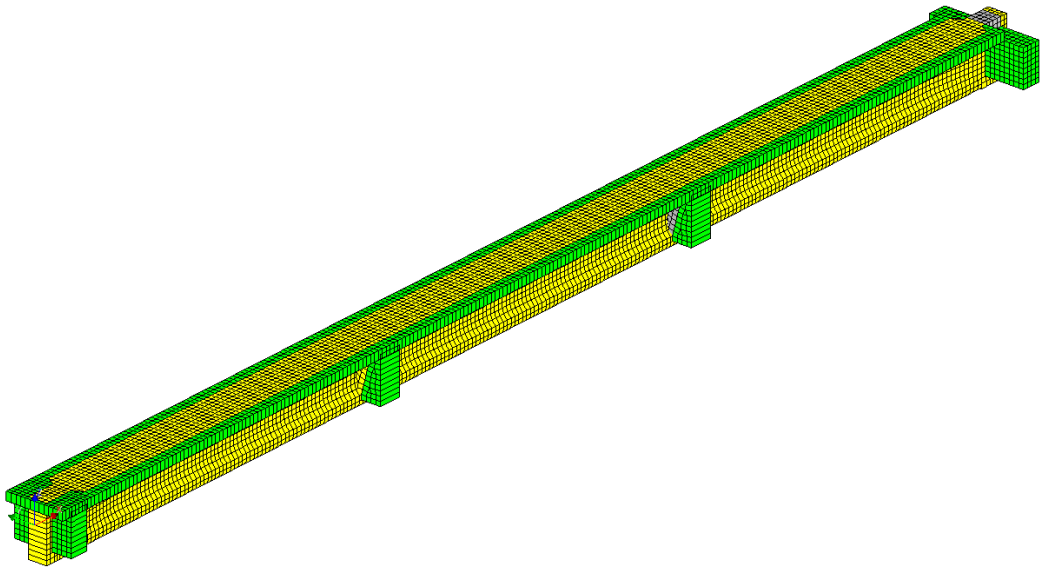

Figure 4.5: Isometric view of the mesh of the IBCL model with assigned thickness displayed

4.2.2. CDCL

The finite element model of the complete deck was created by creating fourteen additional copies of the isolated beam model without the end beam connection modelled in solids. See Figure 4.6. Small modifications were made to recreate the edge beams and several surfaces were combined into one which is shown in Figure 4.7. The mesh can again be considered almost completely structured.

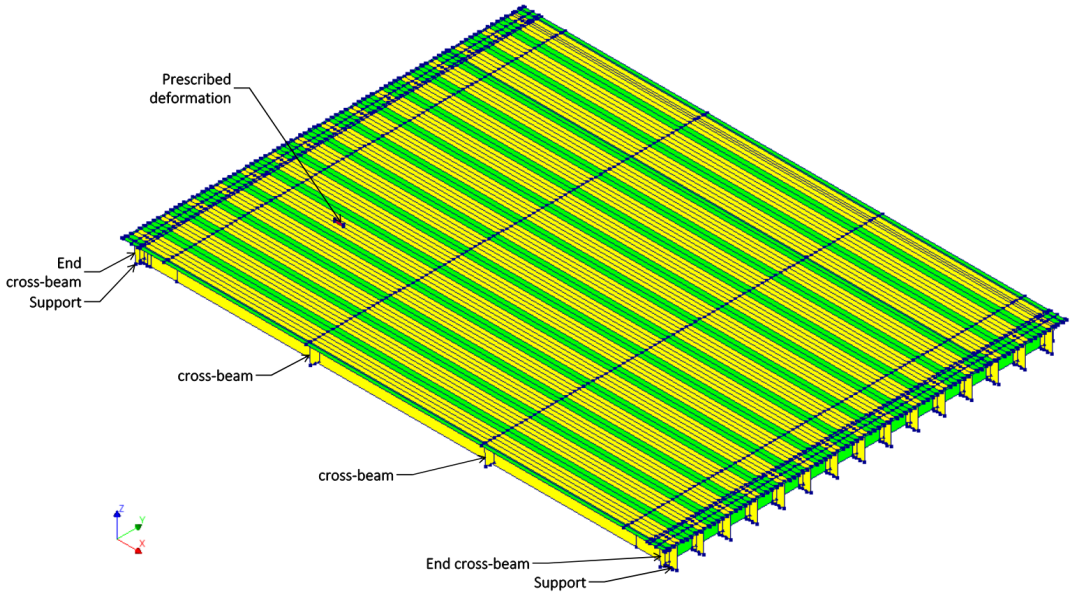

Figure 4.6: Isometric view of the complete deck model with concentrated applied load

4.2.3. CDTL

The complete deck traffic model has the same geometry as the CDCL model. It differs in load setup with the application of the traffic load defined in the Eurocode (see 4.7.3). The values in the load combination tables are adjusted to account for the Eurocode ULS safety factors and the global resistance factor (GRF). Application of the GRF also includes modification of material properties (see 2.2).

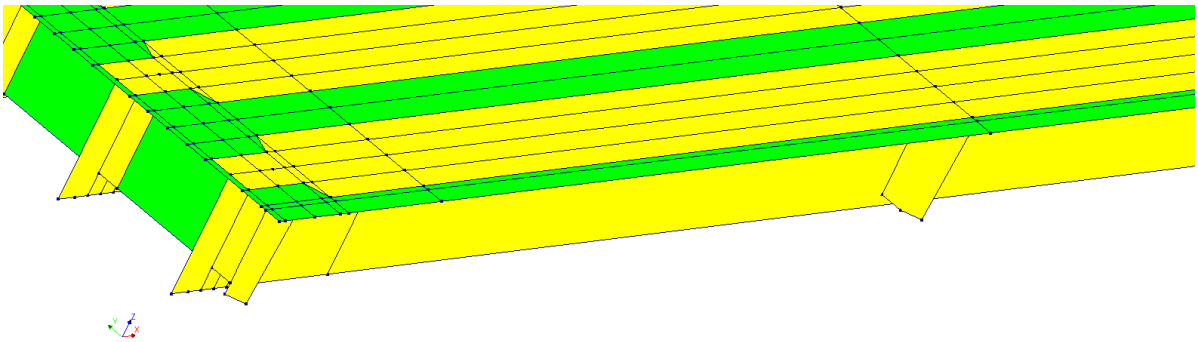

Figure 4.7: Partial isometric view of an edge beam

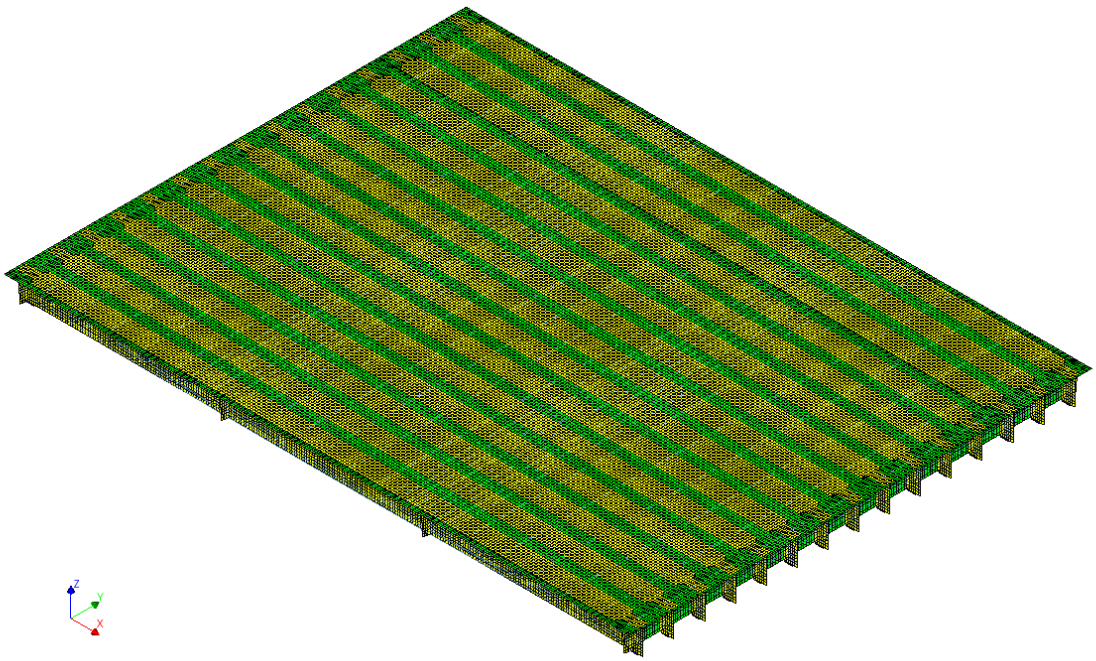

Figure 4.8: Isometric view of the mesh of the CDCL model

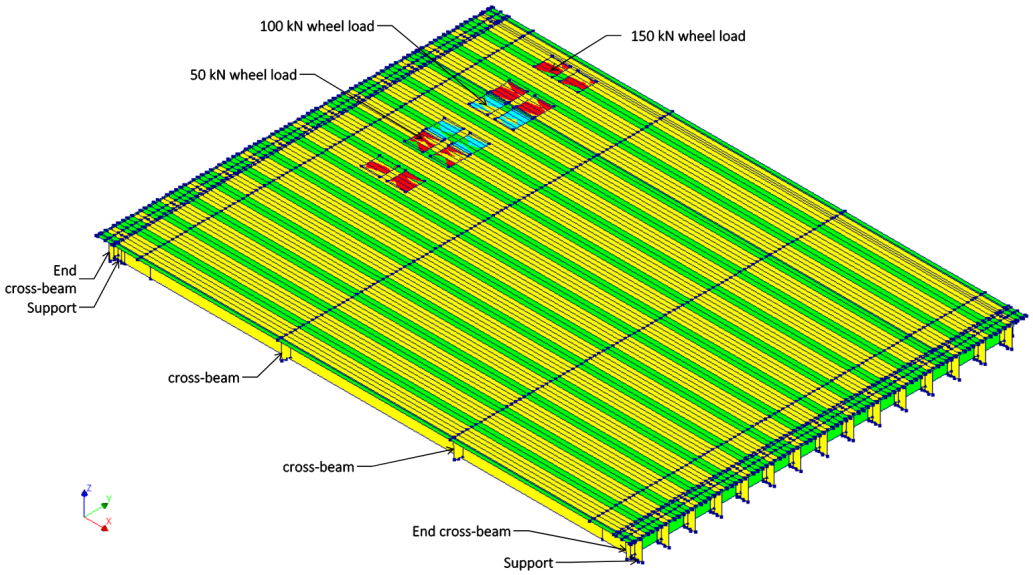

Figure 4.9: Isometric view of the complete deck model with the applied traffic load

4.3. Material properties

4.3.1. Concrete

Both the T-girder and the cast-in-situ deck have their own type of concrete with their properties displayed in Table 4.2.

Table 4.2: Concrete material properties

Property	Girder Concrete	Slab Concrete
Material class in DIANA	Concrete and Masonry	
Material model	Total strain based crack model	
Young's modulus, E	$4{,}4722 \cdot 10^{10}\,\mathrm{N/m^2}$	$3{,}9497 \cdot 10^{10}\,\mathrm{N/m^2}$
Poisson ratio, ν	0.2	
Mass density, ρ	$2500\,\mathrm{kg/m^3}$	
Crack orientation	Rotating	
Tensile curve	Hordijk	
Tensile strength, f_{tm}	$4{,}84 \cdot 10^{6}\,\mathrm{N/m^2}$	$4{,}19 \cdot 10^{6}\,\mathrm{N/m^2}$
Mode-I tensile fracture energy, G_f	$153\,\mathrm{N/m^1}$	$149\,\mathrm{N/m^1}$
Crack band-width	Govindjee	
Poisson's ratio reduction	Damage based	
Compressive curve	Parabolic	
Compressive strength, f_{cm}	$9{,}0 \cdot 10^{7}\,\mathrm{N/m^2}$	$6{,}2 \cdot 10^{7}\,\mathrm{N/m^2}$
Compressive fracture energy	$41\,\mathrm{N/m^1}$	$38\,\mathrm{N/m^1}$
Reduction model (lateral cracking)	Vecchio and Collins 1993	
Lower bound reduction curve	0.4	
Confinement model	Selby and Vecchio	

4.3.2. Reinforcement

Both reinforcement and prestressing steel were used in the Vechtbrug. The laboratory tests have provided the yield and ultimate stress, see section 3.2.2. Table 4.4 shows the remaining material properties to complete the material definition in DIANA.

Table 4.3: Steel tensile tests

test nr.	Yield stress f_y	Ultimate stress f_u	Ultimate strain ϵ_u
Prestressing steel	$1{,}505 \cdot 10^{9}\,\mathrm{N/m^2}$	$1{,}77 \cdot 10^{9}\,\mathrm{N/m^2}$	65 ‰
Reinforcement	$2{,}88 \cdot 10^{8}\,\mathrm{N/m^2}$	$3{,}52 \cdot 10^{8}\,\mathrm{N/m^2}$	60 ‰

Table 4.4: Reinforcement and prestressing steel material properties

Property	Reinforcement	Prestressing
Equivalent steel quality	QR24	QP170
Young's modulus, E	$1{,}95 \cdot 10^{11}\,\mathrm{N/m^2}$	$2{,}00 \cdot 10^{11}\,\mathrm{N/m^2}$
Hardening hypothesis	Strain hardening	
Hardening type	Isotropic hardening	
Initial bonding	Bonded	Unbonded
Density ρ	$7850\,\mathrm{kg/m^3}$	
Poission ratio ν	0.3	

4.4. Constitutive models

4.4.1. Model for concrete

The guidelines prescribe the total strain rotating crack model which is a smeared crack material model. This method does not require a change in topology of the mesh and does not restrict the crack propagation to the mesh lines but instead considers a whole element cracked.

Linear-elastic properties

The linear-elastic material properties are the Young's modulus and the Poisson ratio with a damage based Poisson's ratio reduction. In a fully damaged or in other words cracked state, the Poisson effect of a material is no longer present. Stretching of a cracked direction does no longer lead to contraction of the perpendicular directions [11]. See Table 4.2.

Tensile behaviour

Upon reaching the maximum uniaxial tensile stress, the concrete will start to crack and the maximum tensile stress will decrease with increasing strain. The exponential Hordijk diagram describes this reduction of the tensile stress. Application of an exponential-type softening diagram is preferred since it will result in more localized cracks and consequently will avoid large areas of diffuse cracking [13].

Compressive behaviour

The compressive behaviour should be modelled such that the maximum compressive stress is limited. The parabolic stress strain diagram with a softening branch is prescribed and applied [13].

Tension-compression interaction

A reduction of the compressive strength resulting from lateral cracking (Vecchio and Collings 1993) is enabled to account for tension-compression interaction.

Compression-compression interaction

The effect of confinement is realized by enabling the Selby and Vecchio stress confinement model (see section 2.4.2). It is selected to be enabled in my analysis since at least the prestressing of the concrete in two directions will result in biaxial compression.

Equivalent length

Application of the total strain crack model requires the determination of the crack band width (equivalent lenght, see section 4.5.4) and is performed with the Govindjee method in DIANA.

4.4.2. Model for reinforcement

An elasto-plastic material model with isotropic strain hardening is enabled for both the steel bars and prestressing tendons. See Tables 4.3 and 4.4. No steep softening branch were defined to model rupture. In the performed post analysis check, no bars and tendons have ruptured as the maximum stress remained below σ_u.

4.4.3. Model for concrete-reinforcement interaction

Tension stiffening

The Hordijk diagram is selected as the curve that describes the tensile behaviour. It does not include a tension stiffening effect but ignoring it is a conservative assumption.

Slip

The reinforcement and pre-stressing tendons are modelled as being embedded within the mother element and do not have degrees of freedom on their own. The strains in the steel are computed from the displacement field of the mother elements which implies perfect bond with the concrete. The bond between the concrete and the prestressing steel is only enabled after the prestressing force has been applied. Slip between steel and concrete can be modelled in DIANA. Both Mustafa and Ensink have not enabled bond-slip behaviour. Since I will compare my own numerical results with theirs I have chosen to not enable this feature so no additional differences between the models are introduced.

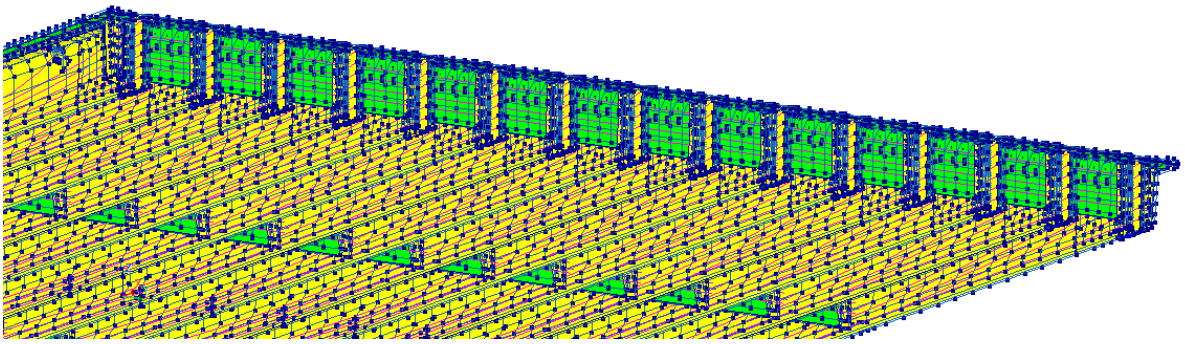

Figure 4.10: Partial view of the bridge geometry represented with sheet and line elements

Dowel action

No options concerning dowel action seem to be available in DIANA.

4.5. Finite element discretization

4.5.1. Finite elements for concrete

Shape and Interpolation

The discretization of the geometry of the Vechtbrug deck is carried out by placing surface elements at the centres of the slab and of each web of the beams (see Figure 4.12). The surface elements will be meshed with quadrilateral elements whenever possible. The use of quadrilateral elements (structured mesh) is preferred over triangular ones (unstructured) because they offer several advantages [26]:

- A structured mesh requires significantly less memory — say a factor of three less — than an unstructured mesh with the same number of elements, because array storage can define neighbour connectivity implicitly. A structured mesh consists of a set of coordinates and connectivities which naturally map into the elements of a matrix, implicitly defining the connectivity. In an unstructured mesh the connectivities and topologies must be explicitly defined in a connectivity matrix, increasing the required memory by a large amount.
- A structured mesh can also save time: to access neighbouring cells when computing a finite difference stencil, software simply increments or decrements array indices. Compilers produce quite efficient code for these operations; in particular, they can optimize the code for vector machines.

The amount of triangles in the mesh is 20 triangles out of 6618 elements per T-beam. The mesh will be constructed of regular curved shell elements. Quadratic elements will be used to prevent shear locking. The mesh will be constructed of CQ40S (curved quadrilateral 40 dof shell) and only when required of CT30S (curved triangular 30 dof shell) elements. Each element in the model is assigned an 'element geometry' which assigns various properties to the element including a thickness (see Table 4.5). The web was assigned a thickness function varying over the z-axis. The transition between the rectangular cross section and the regular profile with the curves had a thickness function varying over both the x and the z-axis. DIANA has an option to display the shells with the assigned thickness, which is shown in Figure 4.13.

Numerical Integration

The guidelines [13] prescribe the use of the following integration schemes in the Table 4.6. The triangular and predominantly quadrilateral shell elements, are numerically integrated in-plane and through the defined depth. The through-depth integration rule should be capable of capturing a gradual stiffness reduction due to cracking and crushing. In general, a 7-point Simpson rule is mostly sufficient but an 11-point Simpson rule is necessary in certain cases and recommended in case of doubt [13].

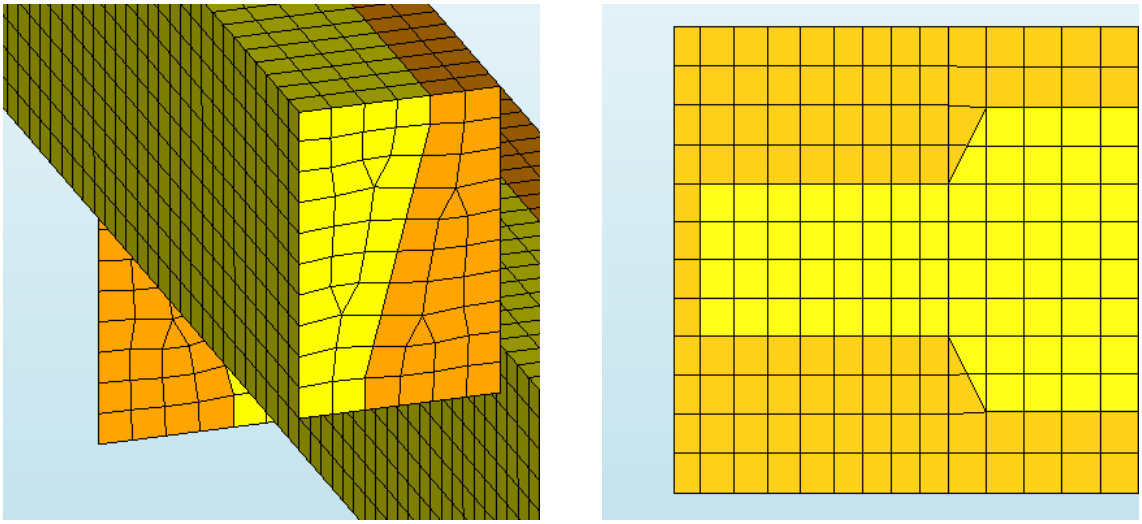

(a) Triangular shell elements in cross beam **(b)** Triangular shell elements in deck

Figure 4.11: Triangular shell elements in the mesh

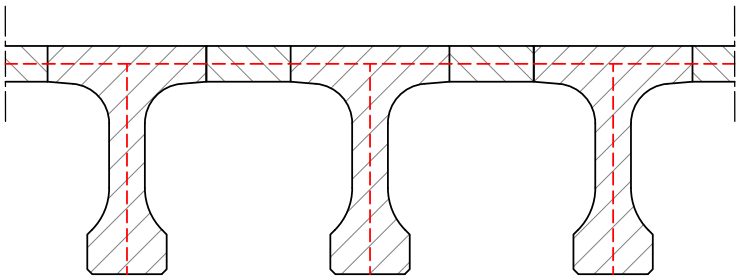

Figure 4.12: Discretization of the cross section

Reduced-order integration for quadratic elements can lead to spurious modes when the stiffness of the element becomes small due to extensive cracking (De Borst and Rots 1989) [13]. *The default integration point scheme for shell and beam elements may not be suitable for the non-linear analysis, since the stress distribution across the shell thickness or beam height cannot be described properly by the definition of three integration points across the thickness. In such cases the user may explicit use more integration points across the thickness of the shell or beam [25].* This is especially true for the bridge deck elements. Those are predominantly subjected to bending making the stress and strains vary a lot through the element depth. This is not the case for the web elements being mostly subjected by membrane forces and therefore having an almost constant stress and strain through the depth. Therefore the standard 3-point Simpson scheme is used for all web elements and is added to table 4.6.

Table 4.5: Element geometries in DIANA

Shell	Interface	Reinforcement
Thickness (function)	Thickness	
Local element axes (x)	Local element axes (y)	
Underlying geometry (flat)		
		Reinforcement type (embedded)
		Cross section input (diameter)

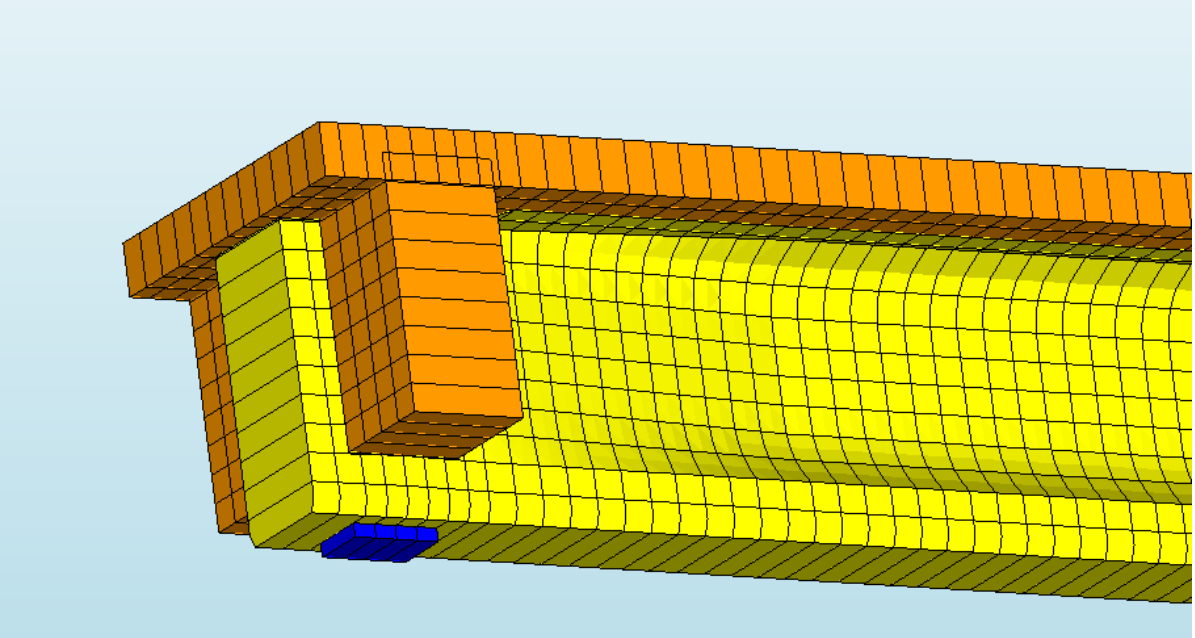

Figure 4.13: Mesh of shells displayed with thickness

Table 4.6: Numerical integration schemes

Orientation	Triangular element	Quadrilateral element	Reinforcement
In-plane	7-point Hammer (Full/high)	3x3-point Gauss (Full/high)	
Through-depth	3-point Simpson (web elements of adjacent beams) 7-point Simpson (standard) 11-point Simpson (when in doubt)		Reduced integration

4.5.2. Finite elements for reinforcement

The reinforcement and prestressing steel is represented by line elements (see Figure 4.10 for a partial view of the bridge geometry). The tendons and reinforcement are modelled as embedded bars and this choice is motivated in Section 4.4.3.

Shape and Interpolation

DIANA automatically selects the order of interpolation without input from the user.

Numerical Integration

The reinforcement can be integrated with a reduced integration scheme since the reinforcement will not exhibit spurious modes since these are inhibited by the embedding element. [13]. The technique of embedding allows the geometries of the reinforcement to be different from the geometries of the mesh. This permits the user to generate the finite element mesh without having to anticipate on the location of reinforcements.

4.5.3. Meshing algorithm

A lot of time and effort have been spend on making sure no distorted elements are present in the meshes of all analyses. The use of imprinting lines on surfaces was required to achieve this result.

4.5.4. Minimum and maximum element size

The largest elements in my model have an approximate size of 0.10 by 0.10 meters. There are no restrictions on the minimum element size other then time and computational limitations. There are however restrictions on maximum element size [13].

1. The first restriction is to ensure that the constitutive model does not exhibit a ”snap-back” in the stress-strain relationship. The maximum element edge length should be approximately half of the maximum equivalent length. The equivalent length is defined by the following equation:

$$h_{eq} < \frac{EG_f}{f_t^2} \tag{4.1}$$

   The quantities and computed values in the following table show that the restriction has been met. Increasing the fracture energy will also increase the equivalent length.

Table 4.7: ”Snap-back” in the stress-strain relationship limitation

Quantity	Symbol	Girder	Slab
Mode-I tensile fracture energy	G_f	$153\,\mathrm{N/m^1}$	$149\,\mathrm{N/m^1}$
Young’s modulus	E	$4{,}4722 \cdot 10^{10}\,\mathrm{N/m^2}$	$3{,}9497 \cdot 10^{10}\,\mathrm{N/m^2}$
Tensile strength	f_t	$4{,}84 \cdot 10^{6}\,\mathrm{N/m^2}$	$4{,}19 \cdot 10^{6}\,\mathrm{N/m^2}$
Maximum equivalent length	h_{eq}	0.292 m	0.334 m
Maximum equivalent length/2	h_{eq}	0.146 m	0.167 m

2. The second restriction is in order to obtain relatively smooth stress fields the chosen element size has to be sufficiently small. be and is given in the following table and shows again that the chosen element size of 0.100 m is sufficiently small.

Table 4.8: Relatively smooth stress field limitation

Object	Equations for maximum element size	Maximum element size value
Girder	$\min\left(\frac{l}{50}, \frac{h}{6}\right)$	0.182 m
Slab (deck)	$\min\left(\frac{l}{50}, \frac{b}{50}\right)$	0.368 m

Table 4.9: Post-tensioning properties

Property	Value	Unit
Friction coefficient (μ)	0.26	-
Wobble coefficient (ω)	0.01	m^{-1}
Wedge set	7	mm

4.6. Prestressing

The prestressing tendons in the longitudinal direction have a curved, asymmetric profile and the transverse tendons a symmetric, straight one. The type and properties of the system used in the Vechtbrug can be found in table "B4-1 Freyssinet en Dywidag" of "Richtlijnen Beoordeling Kunstwerken 1.1" [5] and are: Freyssinet, 12 strands of $\varnothing$7 mm and a steel quality of QP170. The prestressing force is applied in DIANA as a post tensioning load on both ends of the tendons. Through this, the Coulomb friction coefficient and the wobble factor can be taken into account for an more realistic stress distribution along the tendons [21]. These properties are presented in table 4.9. The table B4-1 also states that the maximum initial prestressing force of 500 kN is 65% of the maximum that the system is capable of and considering 20% prestress losses to include long term effects results in an effective prestressing force of 400 kN per tendon. The prestressing tendons are loaded from both ends.
For tests four to seven [18] T-beams were isolated by saw-cuts through both the concrete and the (transverse prestressing) reinforcement on both sides of the beam. The connection to the end-beam furthest away from the loading plate was left intact to secure stability of the beam during testing. Therefore the transverse prestressing is still active in that end-beam.

4.7. Loads

In the following section the different loads are discussed and numbered as load cases (LC).

4.7.1. Dead weight and prestressing

The dead weight (LC1) is applied as a global load by DIANA and the guidelines suggest a 2500 kg/m^3 value for reinforced concrete. The application and magnitude of the prestressing load (LC2) is discussed in section 4.6.

4.7.2. Permanent loads

The Vechtbrug deck was stripped of all asphalt [10] prior to performing the collapse tests. The load of the mandatory layer of asphalt (LC3) was applied for the third analysis with the traffic load (CDTL).

4.7.3. Traffic Loads

In the Netherlands, both the Eurocode 1991-2 and the Richtlijnen Beoordeling Kunstwerken define the traffic load on the bridge deck. The loading that should be applied depends on the use case ranging from disapproval to design. The way the traffic load is defined is almost identical, but it is applied with different safety factors. The EC 1991-2 prescribes Load Model 1 for global and local verifications (LC4).

Notional lanes

The first step to determine the traffic load is to choose a notional lanes configuration (see Figure 4.14) that represents the unfavourable scenario. Notional lane 1 is assumed to start 0.5 m away from the edge of the deck to allow for a guard rail minimizing transverse load distribution.

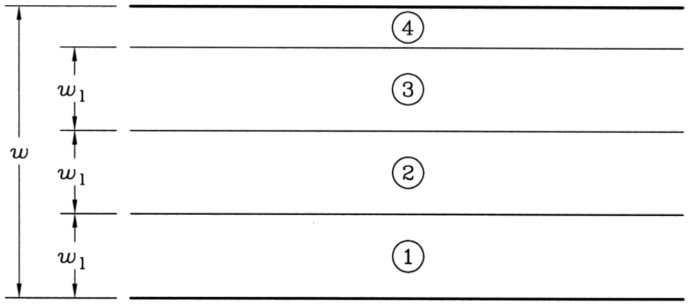

Figure 4.14: Notional lanes configuration, EN 1991-2 figure 4.1

w	=	Carriageway width
w_i	=	Notional lane i
4	=	remaining area

Load Model 1

Next is the application of the two elements of the traffic load Load Model 1 (see Table 4.10). The first element, the axle loads Q_{ik} in Table 4.10 are divided equally among the two loading plates with dimensions of 400x400 mm. The second part is the uniformly distributed load on the entire bridge deck with an increased value on notional lane 1. The reduction factors from table NB.1 of EN 1991-2+C1:2015/NB:2019 α_{Qi} and α_{qi} are set to a value of 1 since no reduction in traffic intensity is intended. The two loads of Load Model 1 are referred to as loading group gr1a in the code [8].

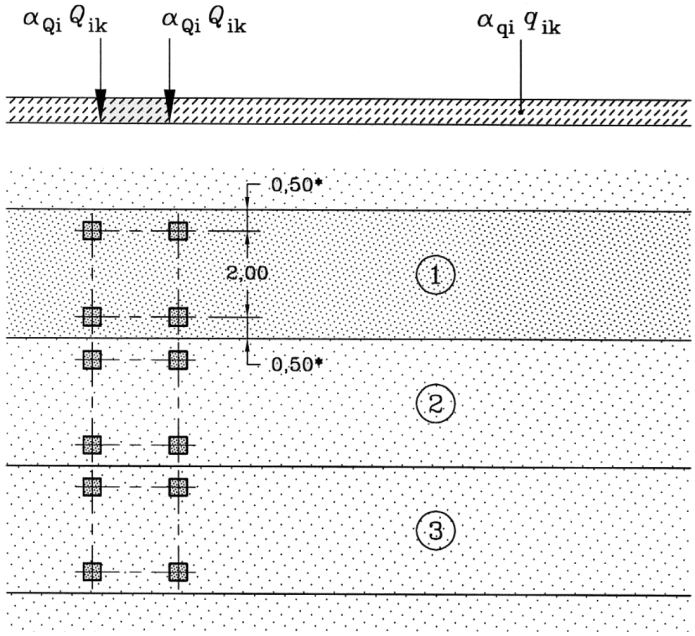

Figure 4.15: Application of Load Model 1 on notional lane configuration, EN 1991-2 figure 4.2a

Table 4.10: 1991-2 Table 6.2 — Load Model 1: Characteristic values

Location	Tandem system ***TS*** Axle loads $\boldsymbol{Q_{ik}}$ [kN]	***UDL*** system $\boldsymbol{q_{ik}}$ (or $\boldsymbol{q_{rk}}$) [kN/m^2]
Notional Lane 1	300	9
Notional Lane 2	200	
Notional Lane 3	100	2.5
Other Lanes	0	
Remaining area [q_{rk}]		

Downwards dispersal of concentrated loads
Article 6.3.6 of EN 1991-2 states that:

1. If the various concentrated loads associated with Load Models 1 and 2 are applied as patch loads, they should be taken as uniformly distributed on their whole contact area.
2. The dispersal through the pavement and concrete slabs may be taken at a spread-to-depth ratio of 1 horizontally to 1 vertically down to the level of the centroid of the concrete slab.

Figure 4.16 shows the resulting dimensions of the concentrated loads. Figure 4.15 shows the location of the applied loads Q_{1k} and Q_{2k} very close together resulting in a concentration of applied loading.

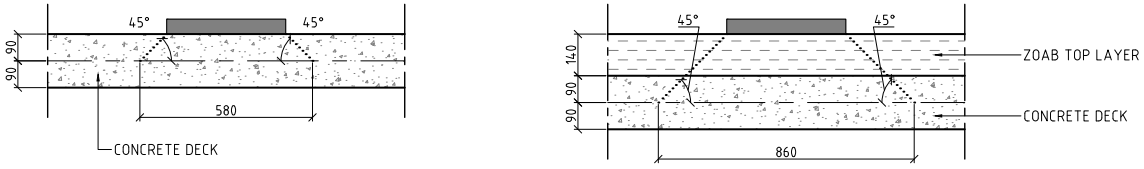

Figure 4.16: Dispersal of concentrated loads with load applied without and with ZOAB top layer.

Determination of the point of application of the traffic load
In section 4.7.3 the notional lanes configuration was chosen, with the heaviest loaded area at the side of the bridge deck to minimize transverse load distribution. The measurement report [18] shows that application of the point load 4 m away from the closest support gave the lowest collapse load. Therefore the location of application of the axel loads is chosen so that the resultant of these loads is at this location.

4.7.4. Applied load
The applied load (LC5) in the collapse test is applied over an area of a single wheel load of the previously discussed traffic load. It is applied to a steel loading plate placed on the centre of a T-beam 2250 mm or 4000 mm centre-to-centre away from the load bearing pads depending on the tests performed [18]. The dispersal of the concentrated load is assumed according to article 6.3.6 of EN 1991-2. See 4.16

4.7.5. Temperature loads
Since the analysis are a recreation of the collapse tests which were performed in unremarkable Dutch weather meaning mild temperatures combined with broken cloud cover. These conditions yield a minimal temperature gradient within the concrete resulting in the absence of temperature loads.

4.8. Boundary conditions
Support plates
The physical bridge deck is supported by elastomeric bearing pads at both ends of each T-beam. Drawing 'C11238 Rubberoplegging' shows the dimensions and materials of the pads. They consist of two 15.5 mm layers of natural rubber between sheets of steel. The entire 'sandwich' is enclosed in a 3 mm layer of natural rubber. An interface represents the complete deformation of the pads (see Table 4.11). A

linear elastic steel block acts as the support plate for the interface to connect to with it's translation is restrained in all directions. Noteworthy is that the y-direction of the interface material corresponds with the global z-axis of the model. The no-tension option is enabled for the support plate interface to improve the accuracy of the response.

Table 4.11: Interface material properties in DIANA

Property	Bearing pads interface	Load plate interface
Type	3D line interface (2 shear, 1 normal)	
Normal stiffness modulus y	$7{,}53 \cdot 10^9$ N/m^3	$4{,}4722 \cdot 10^{10}$ N/m^3
Normal stiffness modulus x Normal stiffness modulus z	$2{,}9 \cdot 10^7$ N/m^3	$4{,}4722 \cdot 10^{10}$ N/m^3
Non-linear elasticity	No-tension option enabled	-

Load plates
The load plate and axel loads are modelled in the analyses IBCL and CDTL as quadrilateral loads. These loads are internally converted to element surface and or element point loads. The sum of forces and moments will be exactly matching the defined force value and position of the quadrilateral force load [11]. Since the load is divided equally across elements during the entire analysis, no stress concentration can occur and application of the interface is not required.
The load plate in the CDCL analysis is modelled as a vertical shell and is loaded by a prescribed deformation. The properties of load interface from the thesis of Mustafa [21] are derived from the properties of girder concrete as suggested in RTD 1016-3B [14]. The normal stiffness of the interface is equal to the Young's modulus of girder concrete and the shear stiffness a factor of 1000 lower (see Table 4.11). This prevents localization of stresses at the point of application of the load. The vertical load plate is restrained in the y-direction.

Phase 1 isolated beam model
In a phased analysis items can be turned on or of for each defined phase which in this case study means boundary conditions. The sides of the cross end beams are considered to be a clamped connection to the world. However, in the first phase, the cross end beams undergo a small translation in x- and z-direction and rotation around the y-axis due to the application of the dead weight and prestressing force. That is why no restraints can be active on the sides of the cross end beam in this phase.

Phase 2 isolated beam model
In this phase the sides of the cross end beam are restrained in all directions.

Phase 2 Prescribed deformation
A support with restraint in the z-direction is activated at the top centre of the loading plate sheet in phase two. The prescribed deformation is assigned to that support.

4.9. Analysis configuration

All performed analyses were geometrically and physically non-linear. All loads are placed in the DIANA model in full, meaning that the complete load is applied upon reaching a load factor of 1. Safety factors are applied on these load factors which are combined in a load combination.

4.9.1. Loading sequences

All analysis start with the application of self-weight and prestressing the tendons in full. During this loading activity bond between prestressing steel and concrete is turned off. Turning it on requires a separate loading activity (position two in the load sequences) and adding the item 'Physic non-linear options' with the bonding option enabled. All following items on the loading sequence require that item to be present and enabled in order to keep bonding enabled for that loading activity. For the CDTL

model the ZOAB layer permanent load is applied in full next. Lastly, the (traffic) load is applied to the structure. The load factors for the ULS simulation are determined in Section 4.10.2 and 4.10.2.

Table 4.12: Loading sequence model IBCL mean values load controlled analysis with arc length control

				LC1	LC2	LC5
Sequence Position	Load Step Size	Load Factor	Load Combination	Self-weight	Pre-stressing	Applied Load
1	0.2	1	Load Combination 1	1	1	
2	0	1	Bonding activation			
3	0.05	Till failure	Load Combination 2			1

Table 4.13: Loading sequence model CDCL mean values displacement controlled analysis

					LC1	LC2	LC5
Sequence Position	Load Step Size	Load Factor	Phase	Load Combination	Self-weight	Pre-stressing	Prescribed Deformation
1	0.2	1	Phase 1	Load Combination 1	1	1	
2	1	1	Phase 2	Start steps + Bonding activation			
3	0.2 mm	Till failure		Load Combination 2			1

Table 4.14: Loading sequence model CDTL ULS simulation with 6.10b factored loads with GRF applied, traffic load group gr1a applied with arc length control

				LC1	LC2	LC3	LC4
Sequence Position	Load Step Size	Load Factor	Load Combination	Self-weight	Pre-stressing	ZOAB Top Layer	TF load gr1a
1	0.2	1	Load Combination 1	1.438	1		
2	0	1	Bonding activation				
3	0.2	1	Load Combination 2			1.787	
4	0.05	Till failure	Load Combination 3				2.145

4.9.2. Load incrementation

The load incrementation is controlled and limited by the application of arc length control for analyses IBCL and CDTL. The step size for the prescribed deformation was 0.2 mm. This value is a good balance between the number of non-converged solutions and the already long analysis time of approximately fourteen days.

4.9.3. Equilibrium iteration

For analyses IBCL and CDTL the Regular Newton Raphson procedure (rN-R) has been selected for equilibrium iteration in combination with the application of arc length control. For the analysis CDCL using the prescribed deformation, the article "Non-linear analysis of prestressed concrete T-beams" [12] suggests the use of the Quasi-Newton BFGS method for that type of analysis.

4.9.4. Convergence criteria

A solution is considered converged when the change in the norm of the last iteration is smaller than the prescribed convergence tolerance ε times the value of the norm in the first iteration of that loading step.

Table 4.15: Suggested convergence criteria in the guidelines

Basis of convergence criterion	Tolerance
Force norm	0.01
Energy norm	0.001

Three different norms are defined in DIANA: The force norm (4.2) which is considered to be the most demanding criterion. Second, we have the energy norm (4.3). The last norm (4.4) is the displacement norm and is considered the easiest to comply with'[4].

$$\|\mathbf{f}_{\text{ext}} - \mathbf{f}_{\text{int},j}\|_2 \leq \varepsilon \times \|\mathbf{f}_{\text{ext}} - \mathbf{f}_{\text{int},1}\|_2 \tag{4.2}$$

$$\|\mathbf{f}^{\text{T}}_{\text{int},j} - \mathrm{d}\mathbf{a}_j\|_2 \leq \varepsilon \times \|\mathbf{f}^{\text{T}}_{\text{int},j} - \Delta\mathbf{a}_1\|_2 \tag{4.3}$$

$$\|\mathrm{d}\mathbf{a}_j\|_2 \leq \varepsilon \times \|\Delta\mathbf{a}_1\|_2 \tag{4.4}$$

The guidelines suggest the convergence criteria in Table 4.15 and considers a solution converged if one of the criteria is met. Load increments in which at least one of the two norms is satisfied can be considered as converged, according to the guidelines. Load increments which do not fully comply the convergence criteria might be still admissible, provided that they are followed by converged load increments and a plausible explanation for the temporarily non-convergence is presented [13]. For analysis CDCL an energy norm tolerance with the recommened value of 10^{-3} was selected. For the other two analyses IBCL and CDTL a stricter convergence criterion with an energy norm tolerance of 10^{-4} was used. The displacement controlled analysis had too much difficulty achieving the stricter convergence resulting in too many non-converged solutions increasing the computation time of the analysis without increasing it's accuracy.

4.10. Ultimate limit state verification

For an ultimate limit state analysis, the load is increased by multiplication with the partial safety factors. The global resistance factor (GRF) is applied on the load as well as the material properties.

4.10.1. Partial safety factors acting on the material properties

The concrete material properties used in the ULS analysis have to be modified by applying the determined global resistance factor of 0.6577 (derived in Section 2.2) on the concrete mean strength, resulting in the modified concrete compressive strengths in Table 4.16.

Table 4.16: Reduced concrete mean strength

Concrete type	Concrete mean compressive strength f_{cm}	Reduced concrete compressive strength $f_{cm,GRF}$
T-Beam	$9{,}0 \cdot 10^7\ \text{N/m}^2$	$5{,}9193 \cdot 10^7\ \text{N/m}^2$
Cast-in-situ	$6{,}2 \cdot 10^7\ \text{N/m}^2$	$4{,}0777 \cdot 10^7\ \text{N/m}^2$

4.10.2. Partial safety factors acting on the load

Ultimate limit state load combinations

The Eurocode 1990-1-1 [23] equations 6.10a and 6.10b define the load combinations with partial safety factors and the most unfavourable combination of the prescribed loads must be used. Because the traffic load is the only variable load, equation 6.10b should be selected to avoid a reduction in loading because of the multiplication of $\psi_{0,1}$.

$$\sum_{j\geq 1} \geq \gamma_{G,j} G_{K,j}'' + ''\gamma_P P'' + ''\gamma_{Q,1}\psi_{0,1} Q_{k,1}'' + '' \sum_{i>1} \gamma_{Q,i}\psi_{0,i} Q_{k,i} \tag{6.10a}$$

$$\sum_{j\geq 1} \geq \xi_j \gamma_{G,j} G_{K,j}'' + ''\gamma_P P'' + ''\gamma_{Q,1} Q_{k,1}'' + '' \sum_{i>1} \gamma_{Q,i}\psi_{0,1} Q_{k,i} \tag{6.10b}$$

Ultimate limit state partial safety factors

The determination of the safety factors starts with the selection of the consequence class with the use of table NB.11 – 2.1 of 1990 NB [24] which yields consequence class 3. This brings us to table NB.16 – A2.4(B) 1990 NB [24] 'Load factors for road bridges' which shows us that the partial factor for the self-weight and permanent load $\xi\gamma_{G,j,\text{sup}}$ is 1.25 and the partial factor for the traffic load is 1.5. The factors for the serviceability limit state are both 1.0. Table 2.2 of the RBK [17] presents the different partial load factors for the different use cases. Tables NB.16 – A2.4(B) and 2.2 combined gives us the following load factors from Table 4.17 for each use case. Article 2.4.2.2 of NEN-EN 1992-1-1 states that if application of the prestressing force is favourable which it is in this case, γ_P should be equal to 1.0.

Table 4.17: Eurocode and RBK partial load factors

Reliability level	β (cc3)	Reference period (years)	Permanent 6.10b $\xi\gamma_{G,j,\text{sup}}$	Traffic gra1 $\gamma_{Q,1}$
Eurocode ULS	4.3	100	1.25	1.5
RBK Design	4.3	100	1.25	1.5
RBK Renovation	3.6	30	1.15	1.3
RBK Usage	3.3	30	1.15	1.25
RBK Disapproval	3.1	15	1.1	1.25
Eurocode SLS	1.5	50	1.0	1.0

GRF partial safety factors

Section 4.17 has shown that the self weight (LC1) only has to be multiplied with the model uncertainty factor $\gamma_{Rd,NLFEM}$ = 1.15. The global resistance factor is called γ_{GL} in source [1] and $\gamma_{0'}$ in the guidelines [13]. The value is 1.43 and has to be applied on the permanent load (LC3) and the traffic load (LC4). All this combined yields the following load factors in DIANA in Table 4.18.

Table 4.18: Determination of DIANA load factors

Load cases	$\gamma_{Rd,NLFEM}$	γ_{GL}	EC ULS safety factor	Diana load factor
LC1 Self weight	1.15		1.25	1.438
LC2 Prestressing			1	1
LC3 permanent load ZOAB		1.43	1.25	1.787
LC4 Traffic load LM1		1.43	1.50	2.145

5 Results

5.1. Model IBCL

5.1.1. Results of the analysis using the non-planar shell mesh

Reviewing the results of the numerical analysis of collapse test 7, the occurrence of several events can be distinguished which are presented in Table 5.1 and are annotated on the load-displacement curve in Figure 5.1. The deformation of the beam is shown in Figure 5.3. Figure 5.3a shows the upward curvature of the beam due to the tendons forcing the concrete upwards. Figure 5.3b shows the vertical deformation at maximum load and Figure 5.3c shows the kink in the top flange after collapse. The numerical failure is due to crushing of the concrete in the top flange (see Figures 5.4a and 5.4b). The crushing of the concrete reduces the compressive stress in the loading step after the maximum load has been reached. The yielding of the longitudinal reinforcement occurs right after the formation of flexural cracks (Figure 5.5). The yielding of the stirrups occurs but not straight away after the formation of a shear crack. The tendons are yielding at the location of the applied load (Figure 5.6b) but have not reached the ultimate stress of $1{,}77 \cdot 10^9\,\mathrm{N/m^2}$ (Figure 5.6d.) The development of the crack pattern is presented in Figure 5.7. Finally, Figure 5.8 shows us that compressive strut has formed but it's load is small due to the lack of lateral restraint. Several load step show snap-through behaviour in the load-displacement curve (Figure 5.1) and those load steps show a reduction in plasticity and an increase in crack formation (See Figure 5.2).

Table 5.1: Events of the IBCL analysis

Load step	Figure nr.	Event
13	5.5a	Yielding of longitudinal rebars in the bottom flange
14	5.7a	Development of flexural cracks
23	5.7b	Development of shear cracks
36	5.5b	Yielding of stirrups
46		snap-through behaviour
57		snap-through behaviour
66	5.6b	Yielding of longitudinal tendons
71		snap-through behaviour
116		snap-through behaviour
131	5.4a	Maximum load
132	5.4b	Post collapse, concrete has crushed, non converged solution

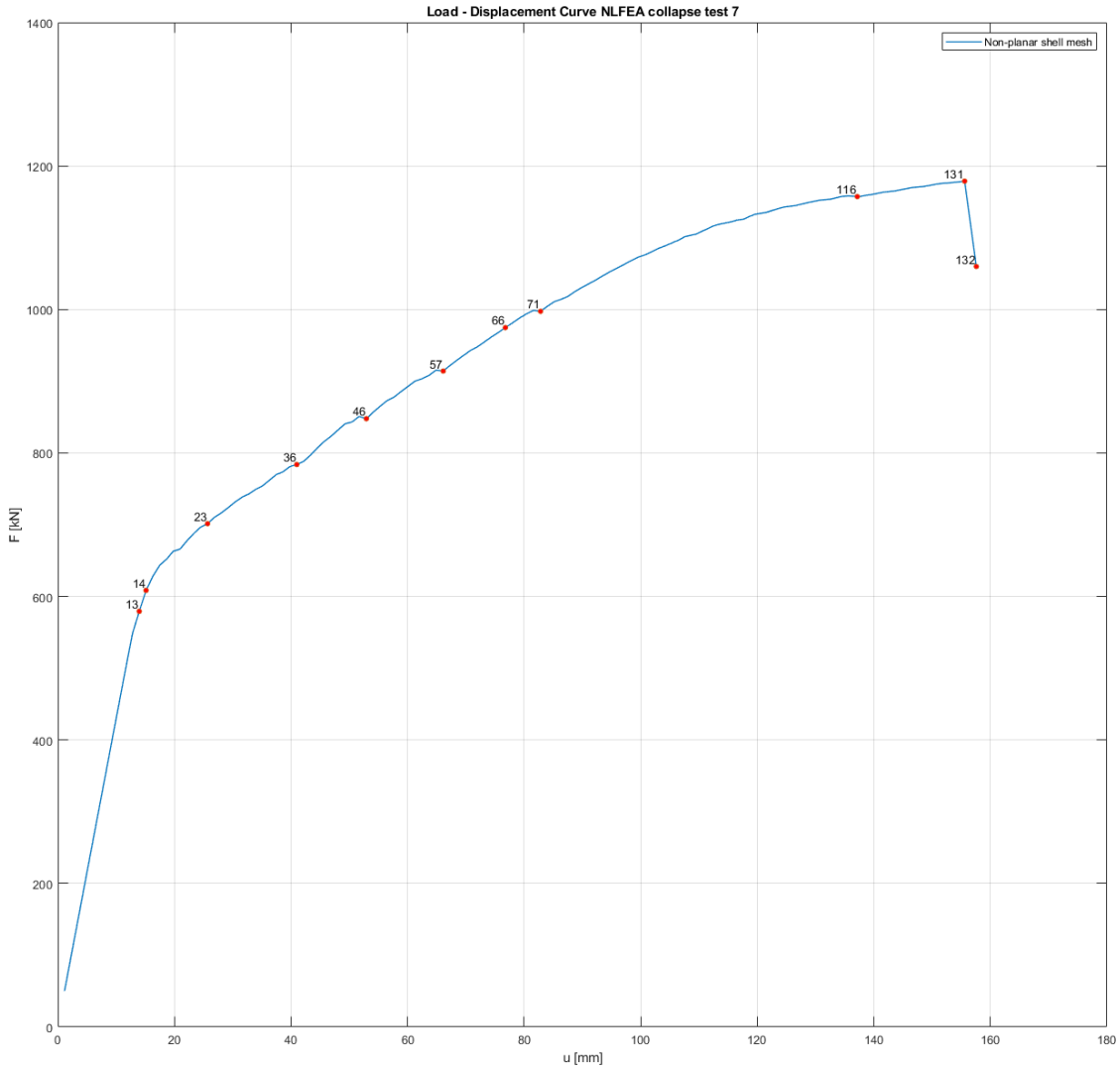

Figure 5.1: Load-displacement curve of the IBCL analysis

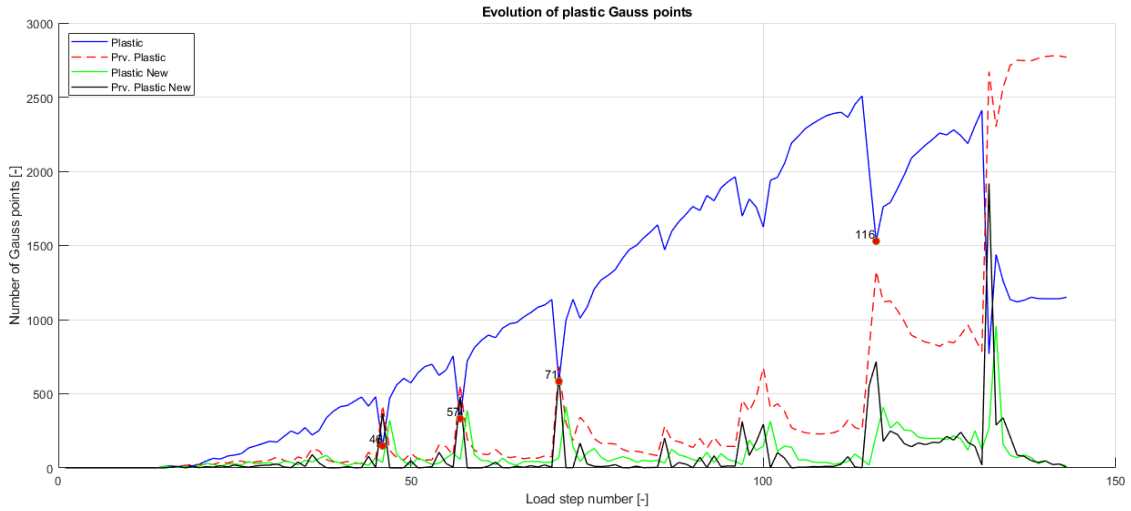

(a) Evolution of the number of Gauss points with (former) plastic behaviour (crushing or yielding)

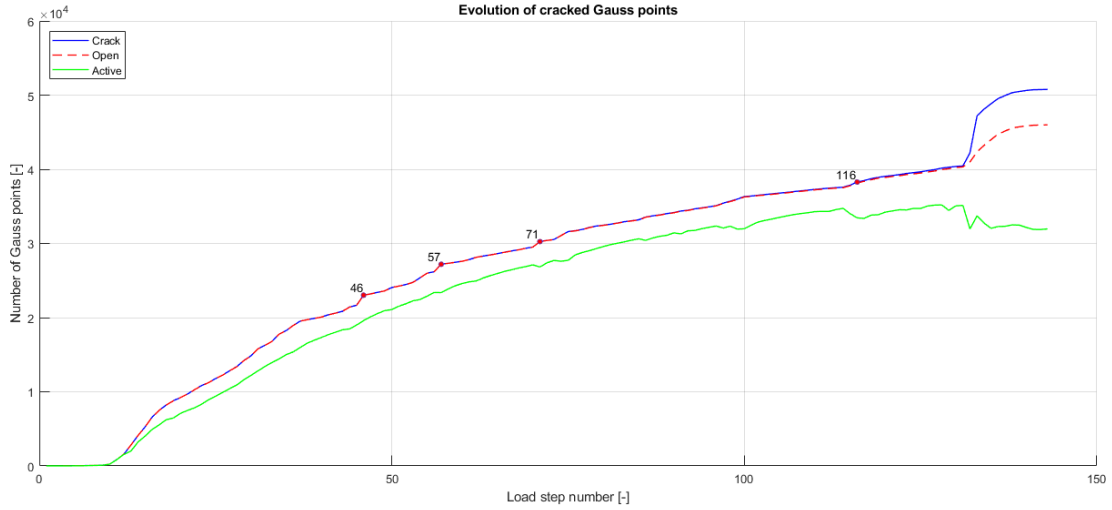

(b) Evolution of the number of cracked Gauss points

Figure 5.2: Gauss point statistics (IBCL)

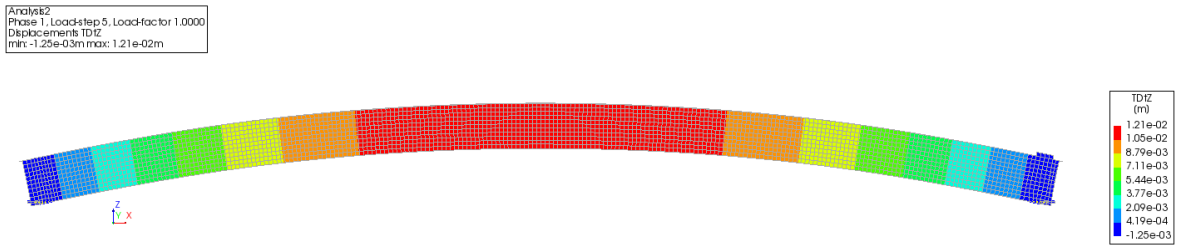

(a) Vertical deformation after prestressing

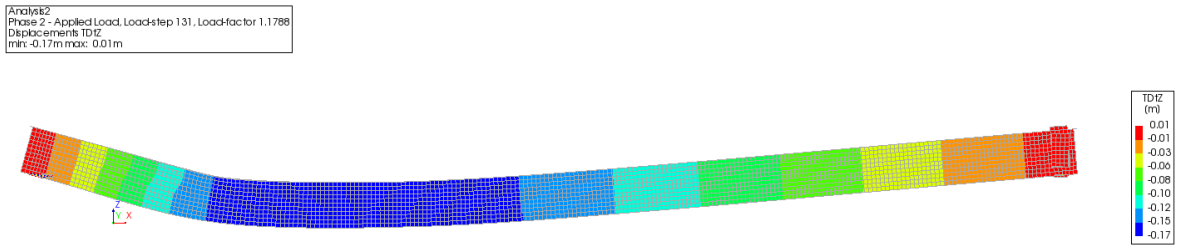

(b) Vertical deformation at maximum load

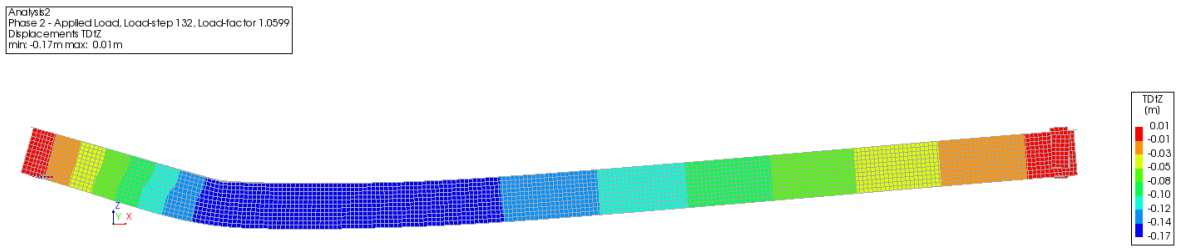

(c) Vertical deformation after collapse

Figure 5.3: Vertical deformation (IBCL)

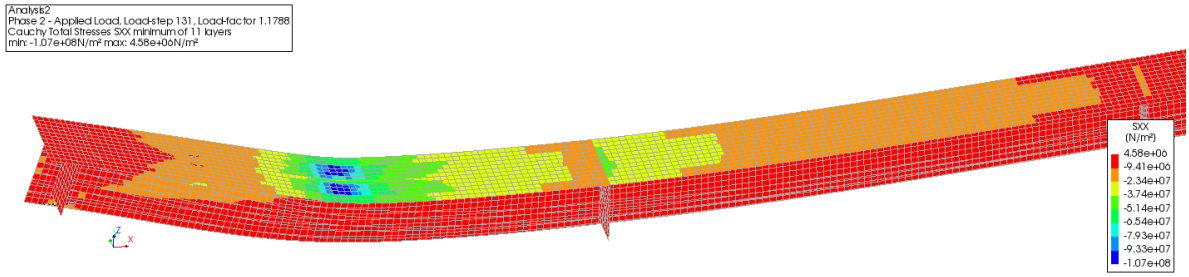

(a) Concrete stress SXX at maximum load

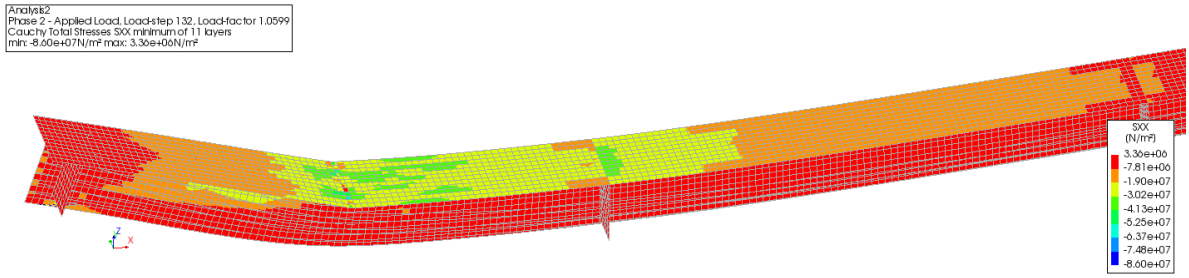

(b) Concrete stress SXX after collapse

Figure 5.4: Concrete stress SXX (IBCL)

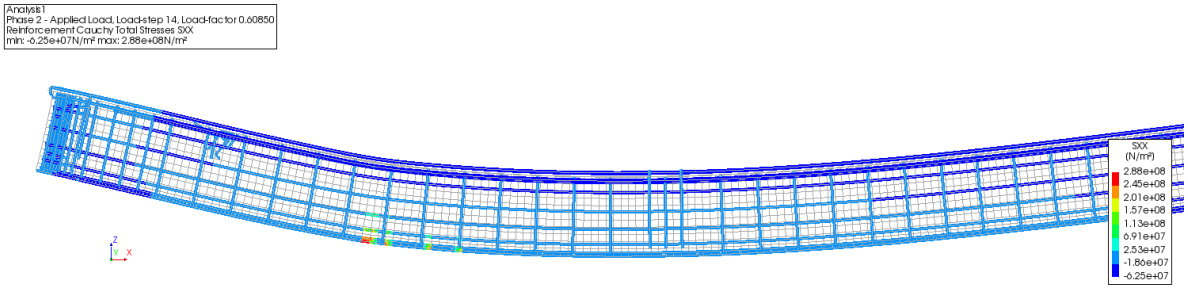

(a) Yielding of longitudinal rebars

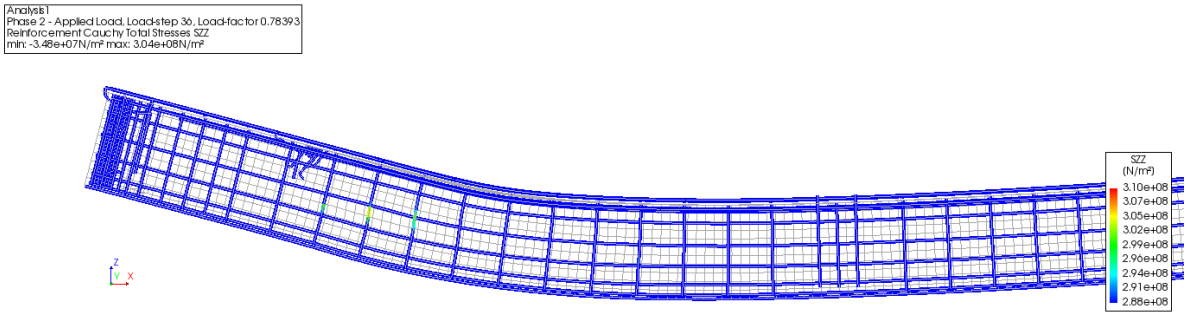

(b) Yielding of stirrups

Figure 5.5: Yielding of rebars (IBCL)

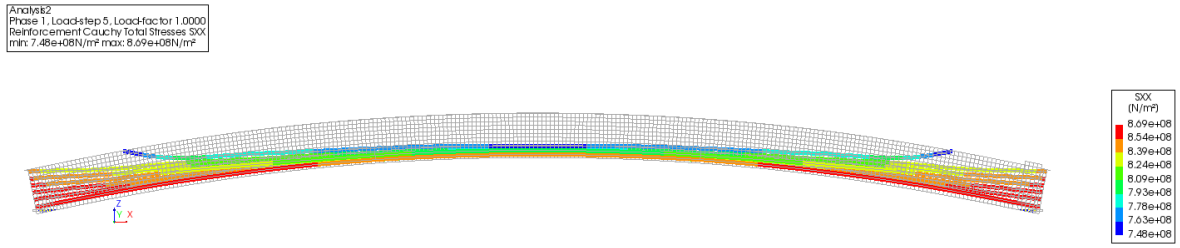

(a) Tensile stresses in tendons after prestressing

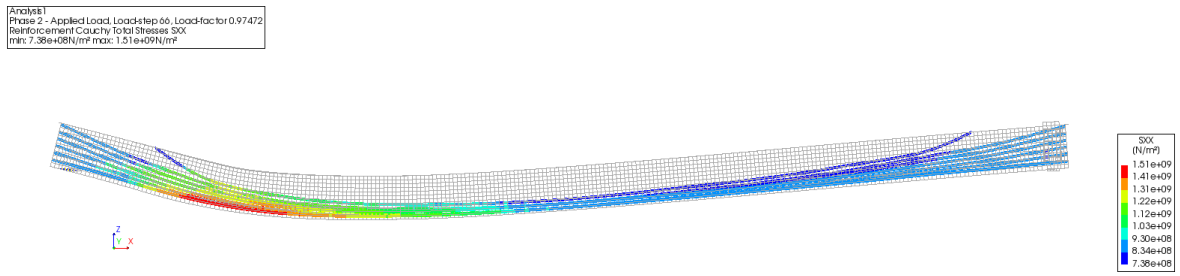

(b) Yielding of the longitudinal tendons

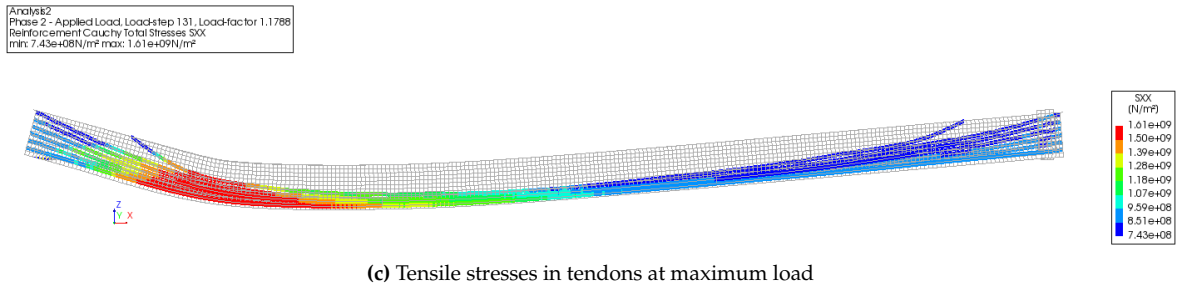

(c) Tensile stresses in tendons at maximum load

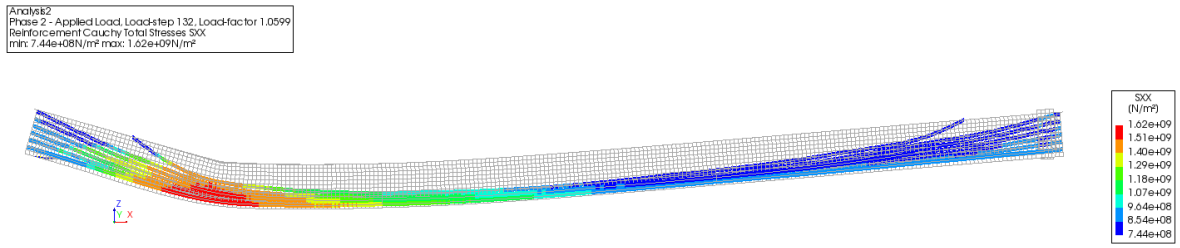

(d) Tensile stresses in tendons after collapse

Figure 5.6: Tensile stresses in longitudinal tendons (IBCL)

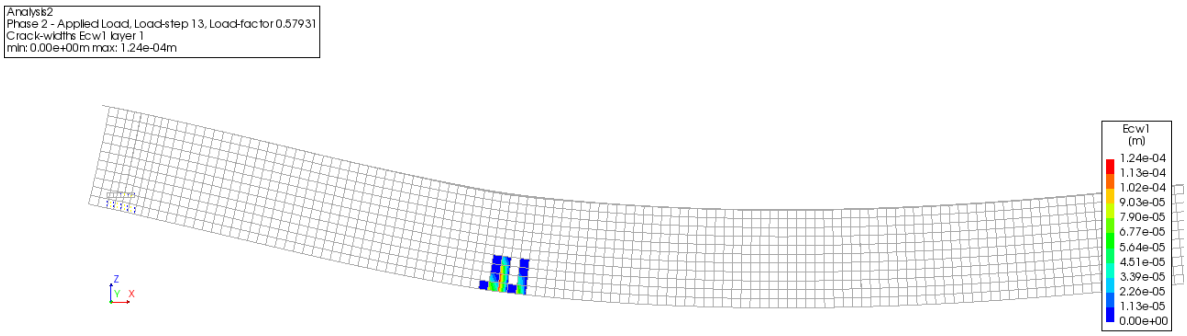

(a) Development of bending cracks

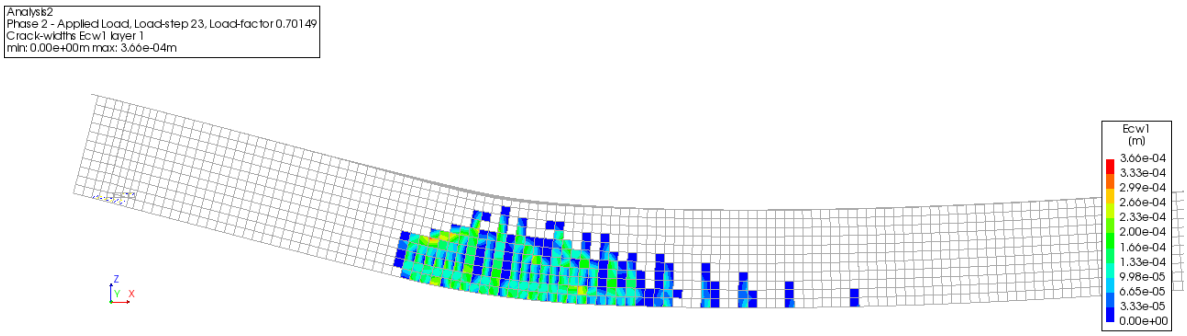

(b) Development of shear cracks

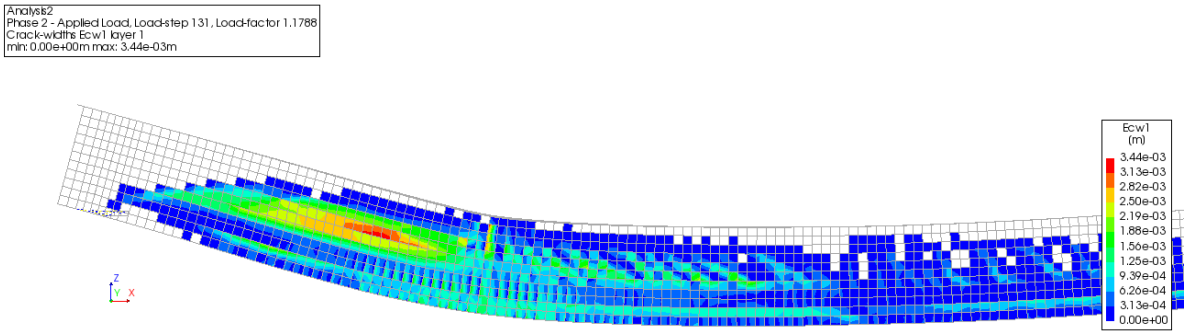

(c) Crack width at maximum load

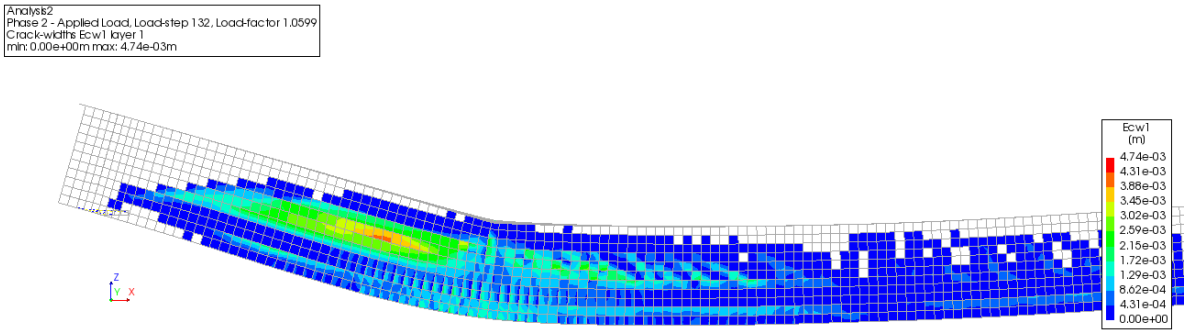

(d) Crack width after collapse

Figure 5.7: Crack width (IBCL)

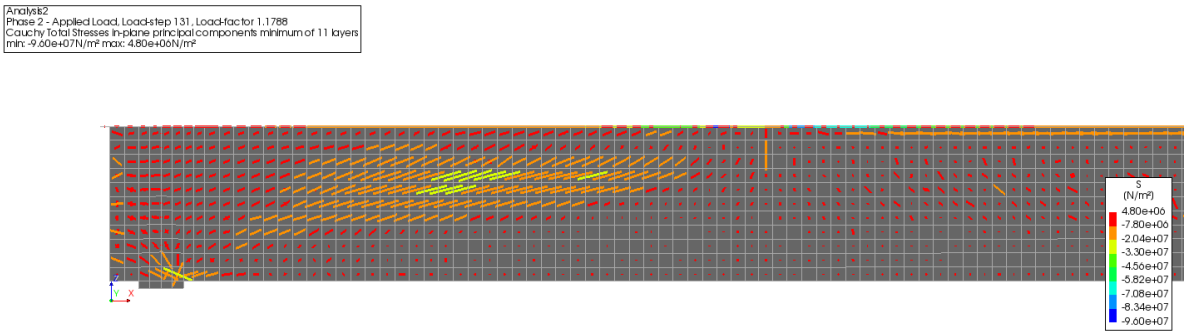

Figure 5.8: Cauchy total stresses in-plane principal components (IBCL)

5.1.2. Verification with collapse test data

The results of the numerical analysis are verified by comparing them with the performed measurements (see Figure 3.10) of the field test in Table 5.2. The data shows that the numerical model has an overly stiff and especially ductile response. Noteworthy is that the deviation of the load-displacement curve starts at approximately at load step 50 with a load factor of 0.88. The development of the shear cracks has been active since load step 23 (see 5.7b). If we look at Figure 5.9 we can see that the two load-displacement curves are in complete agreement until load step 50 with load factor 0.88 is reached. There is an overestimation of the stiffness at the maximum load which might have been one or two % lower if the beam didn't require unloading during the collapse test.

Table 5.2: Verification of IBCL results with collapse test 7 data

Measurement	Collapse test 7	IBCL	Difference
Collapse load	$1{,}022 \cdot 10^{6}$ N	$1{,}179 \cdot 10^{6}$ N	15 %
Deflection under load	$1{,}320 \cdot 10^{-1}$ m	$1{,}558 \cdot 10^{-1}$ m	18 %
Deflection at cross beam	$1{,}389 \cdot 10^{-1}$ m	$1{,}686 \cdot 10^{-1}$ m	21 %
Strain over 1 m at failure	$8{,}800 \cdot 10^{-3}$ –	$1{,}187 \cdot 10^{-3}$ –	35 %
Deflection at support at failure	$9{,}400 \cdot 10^{-3}$ m	$9{,}189 \cdot 10^{-3}$ m	−2,25 %

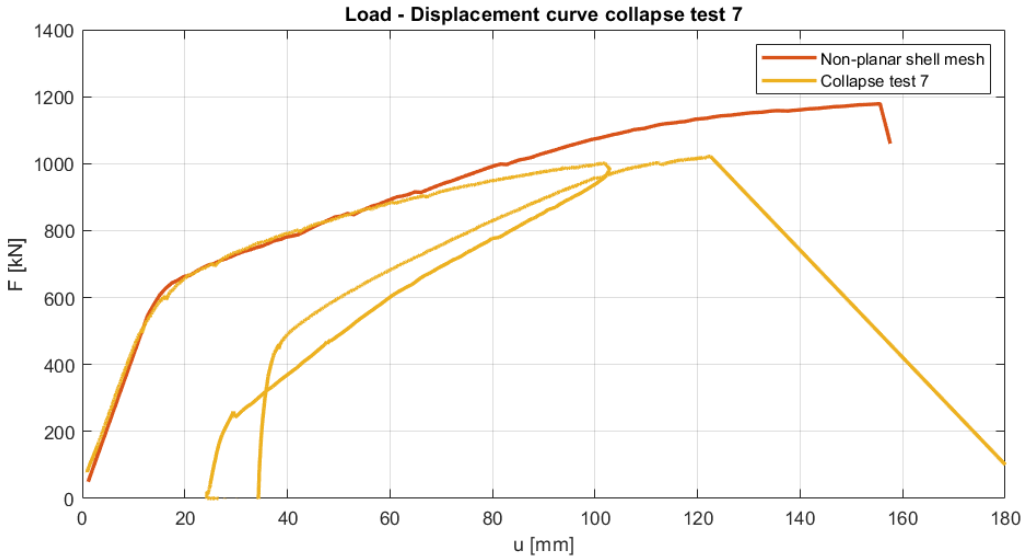

Figure 5.9: Comparison of the load-displacement curve of the field test 7 and non-linear finite element analysis

5.1.3. Comparison of results of NLFEA with different meshes

In Figure 5.10 the load-displacement curves of the numerical models of Mustafa, my own model and the test results are plotted. It shows that the results of the numerical analyses are in agreement and all show the same overly stiff and ductile response. The deflection during the collapse test 7 was greater than anticipated which required unloading and adjustment of the safety chains. In Table 5.3 the failure loads and deflections are presented. Unfortunately, modelling the complete bridge deck with 3d solid elements was not within the available computational capabilities for this thesis.

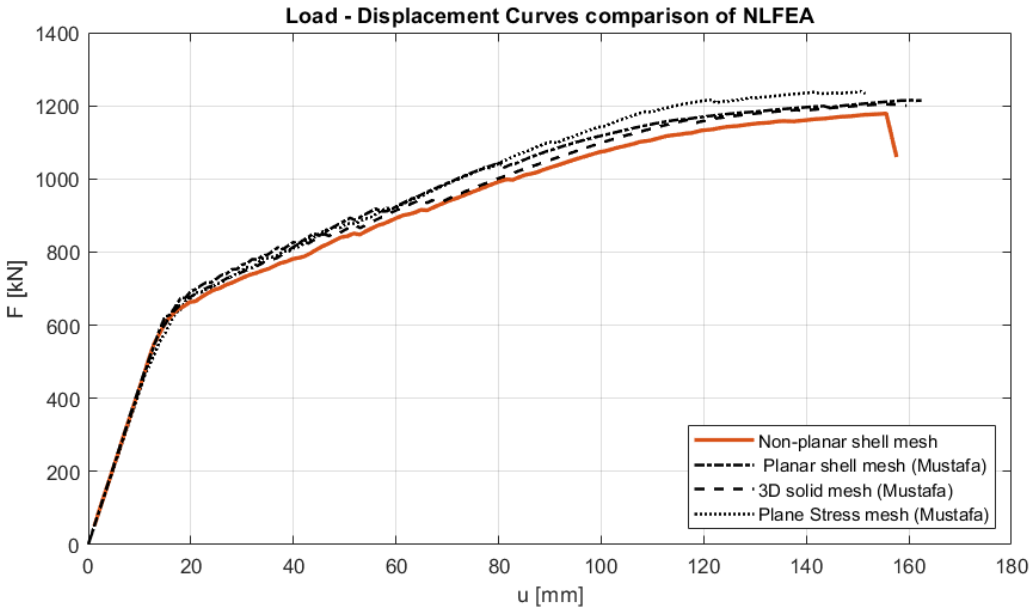

Figure 5.10: Comparison of the load-displacement curves of the numerical analyses of collapse test 7 with different meshes.

Table 5.3: Comparison of the collapse load and deflection to the field test and non-linear finite analyses

	F_u [kN]		δ_u [mm]	
Test 7	1022		132	
Shell non-planar mesh	1179	15%	156	18%
Plane stress mesh (Mustafa)	1239	21%	151	14%
Planar shell mesh (Mustafa)	1215	19%	162	23%
Solid 3D (Mustafa)	1205	18%	156	18%
Solid 3D (Ensink)	1178	15%	165	25%

5.1.4. Increase in normal force

To detect the presence of arch action manifesting in the beam, it is required to determine the increase in normal force which should be generated by a lateral restraint. The only lateral restraint available is the load bearing pad resisting shear deformation. The increase in horizontal reaction force caused by the applied load is $1.64e + 6$N.

5.2. Model CDCL

5.2.1. Results of the analysis using the non-planar shell mesh

The events that have occurred during the numerical analysis of collapse test 1 are presented in Table 5.4 and are annotated on the load-displacement curve in Figure 5.11. The deformation of the deck is shown in Figure 5.13. Figure 5.13a shows the upward curvature in both x and y-direction of the deck due to the tendons forcing the concrete upwards. Figure 5.13b shows the vertical deformation at maximum load. The numerical failure is due to crushing of the concrete in the top flange of the girder. The Figure 5.14 shows the crushing of the concrete in x-direction at failure and a reduced stress thereafter. The Figure 5.15 shows that the crushed concrete cannot withstand the stresses in the y-direction any more and the load is transferred to the concrete around the loading plate resulting in a small increase of stress. The longitudinal rebars start to yield after formation of flexural cracks and the yielding of the stirrups occurs a few load steps after development of the first shear crack (see Figure 5.16). The longitudinal tendons are not yielding at all during the complete analysis. The transverse tendons do yield but do not reach the ultimate stress (See figures 5.17a and 5.17c). The development of the crack pattern is presented in

Table 5.4: Events of the CDCL analysis

Load step	Figure nr.	Event
11	5.18a	Development of flexural cracks
13	5.16a	Yielding of longitudinal rebars in the bottom flange
28	5.18b	Development of shear cracks
35	5.16b	Yielding of stirrups
36		snap-through behaviour, no convergence
96		snap-through behaviour, no convergence
158	5.17b	Yielding of transverse tendons
265	5.14a	Maximum load
266	5.14b	Post collapse, concrete has crushed, non converged solution

Figure 5.18. Finally, Figure 5.19a shows us that compressive struts has formed in the loaded girder but again it's load is small relative to the compressive strength of the girder concrete so the contribution to the load-carrying capacity is minimal. Figure 5.19 shows no signs of the presence of a compressive arch/strut. Load steps 36 and 96 did not converge with an relative energy variation of $8{,}909 \cdot 10^{-3}$ and $5{,}542 \cdot 10^{-3} 5.542e-03$. The steps also showed some snap-through behaviour (Figure 5.11) but this was not accompanied with any noteworthy event in the evolution of plastic or cracked Gauss points (see Figure 5.12a). However, the last part of the graph depicting the evolution of the plastic Gauss points (Figure 5.12a) show a line with amplitudes spiking matching the non-smooth line of the last part of the load-displacement curve.

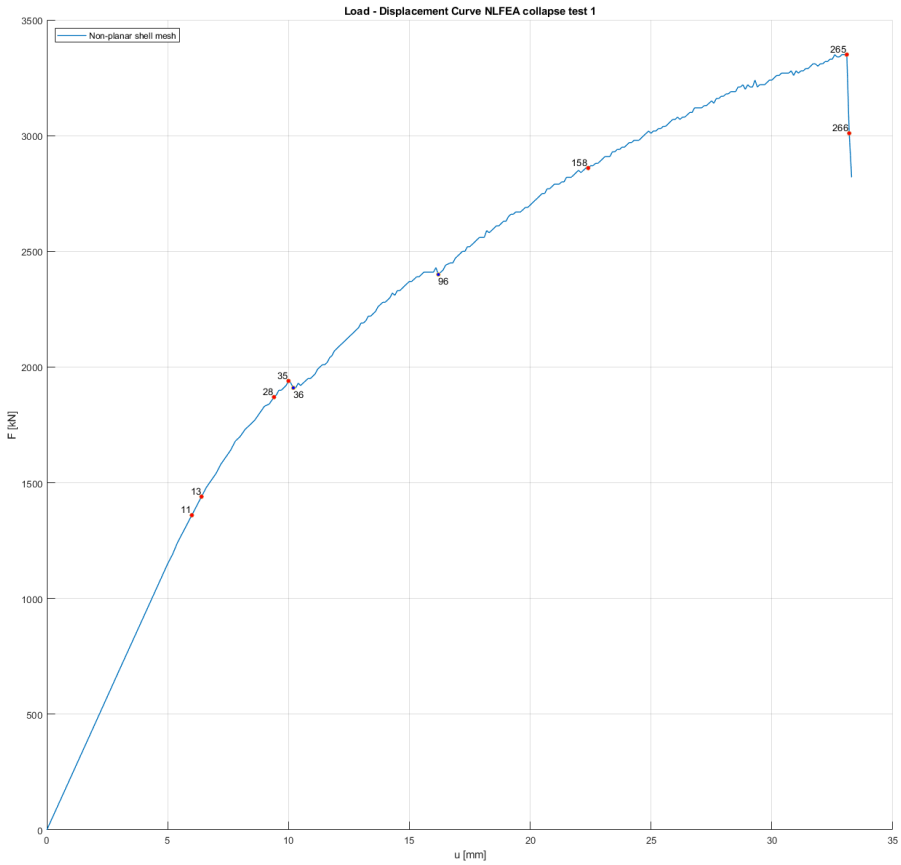

Figure 5.11: Load-displacement curve of the CDCL analysis

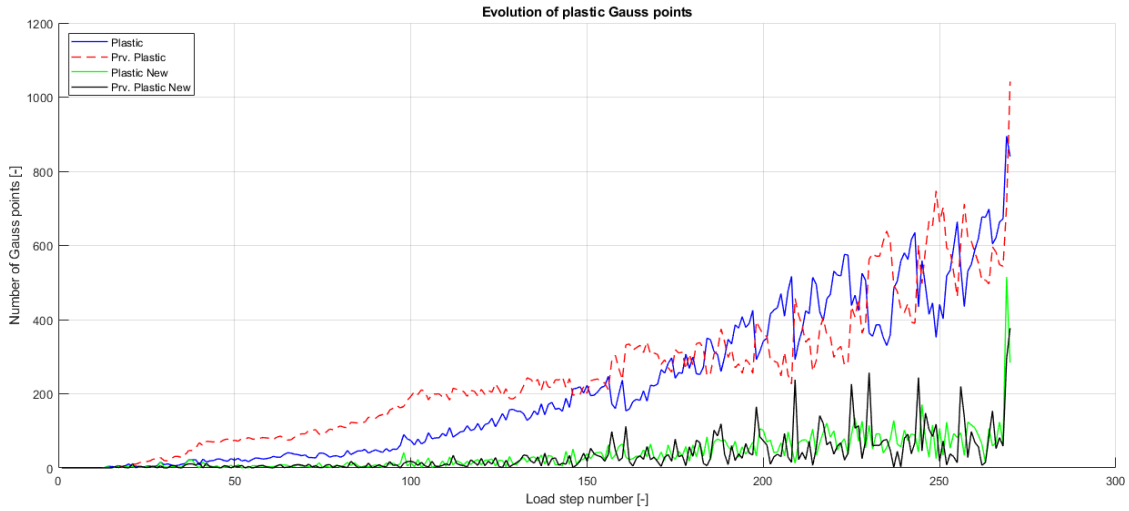

(a) Evolution of the number of Gauss points with (former) plastic behaviour (crushing or yielding)

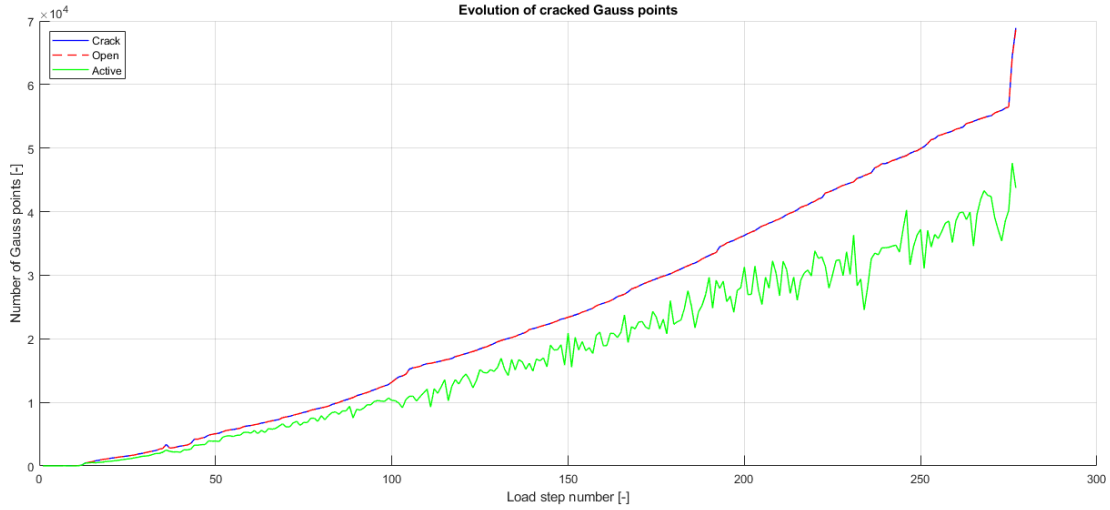

(b) Evolution of the number of cracked Gauss points

Figure 5.12: Gauss point statistics (CDCL)

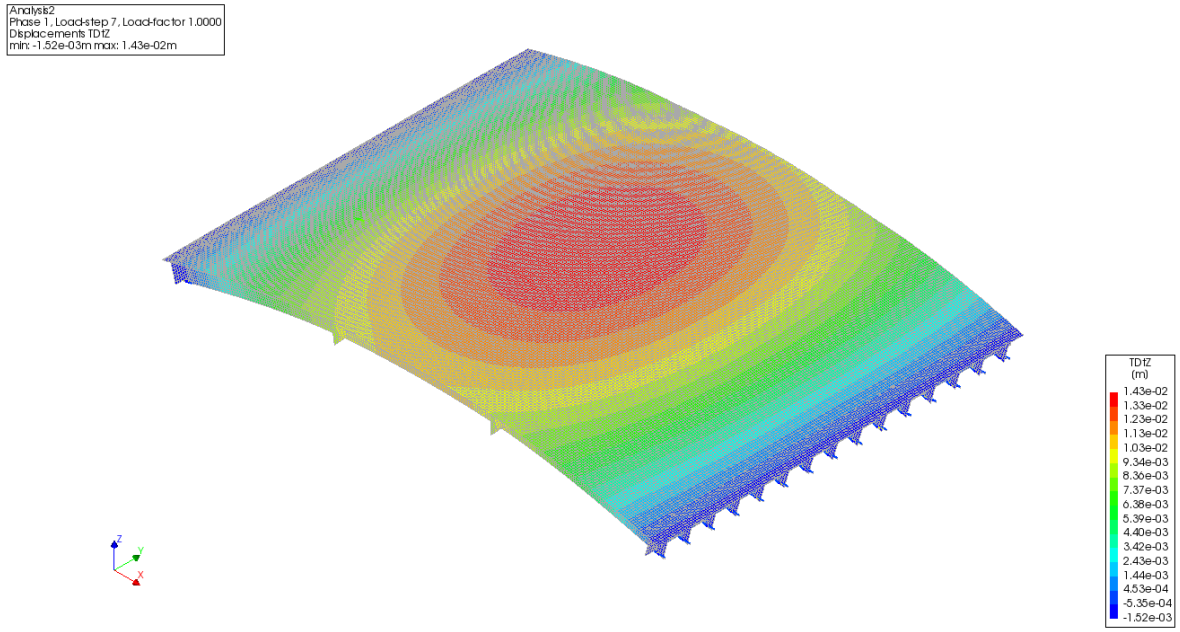

(a) Vertical deformation after prestressing

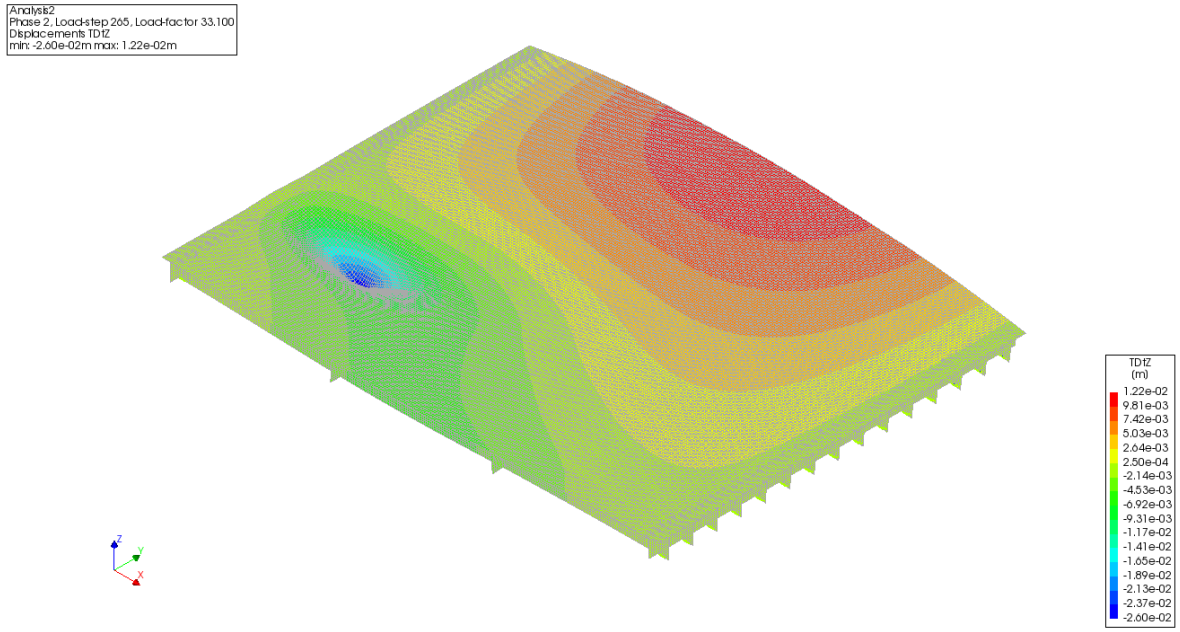

(b) Vertical deformation at maximum load

Figure 5.13: Vertical deformation (CDTL)

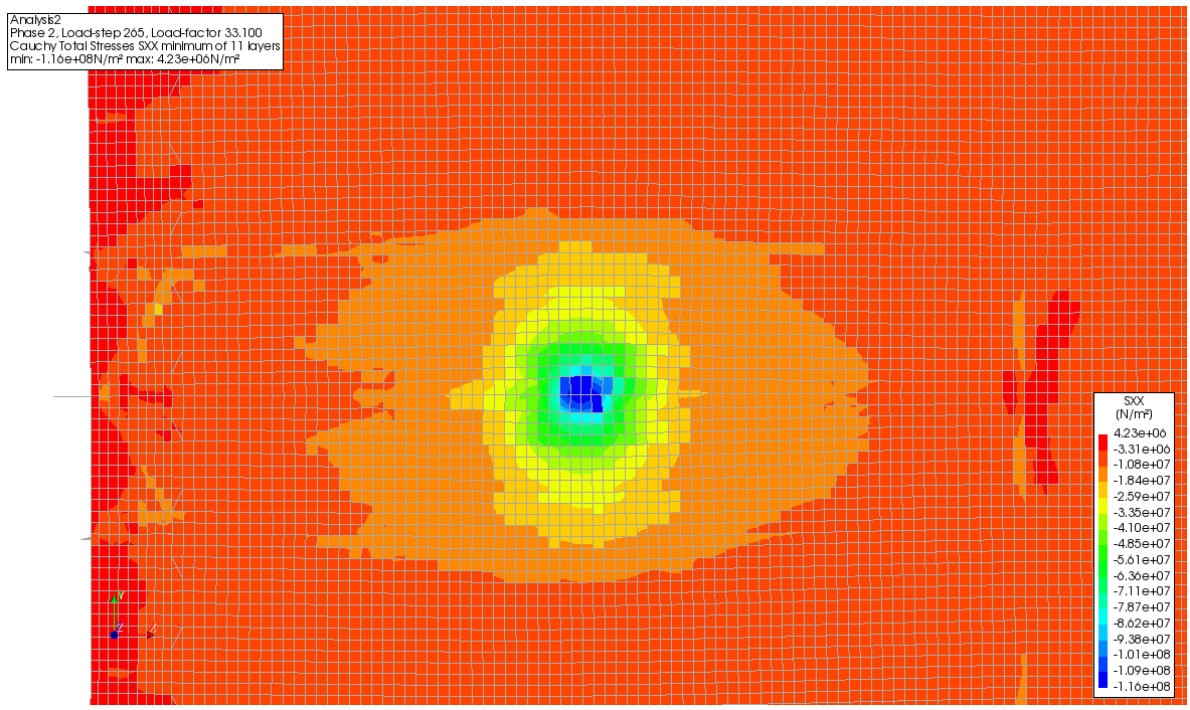

(a) Concrete stress SXX at maximum load

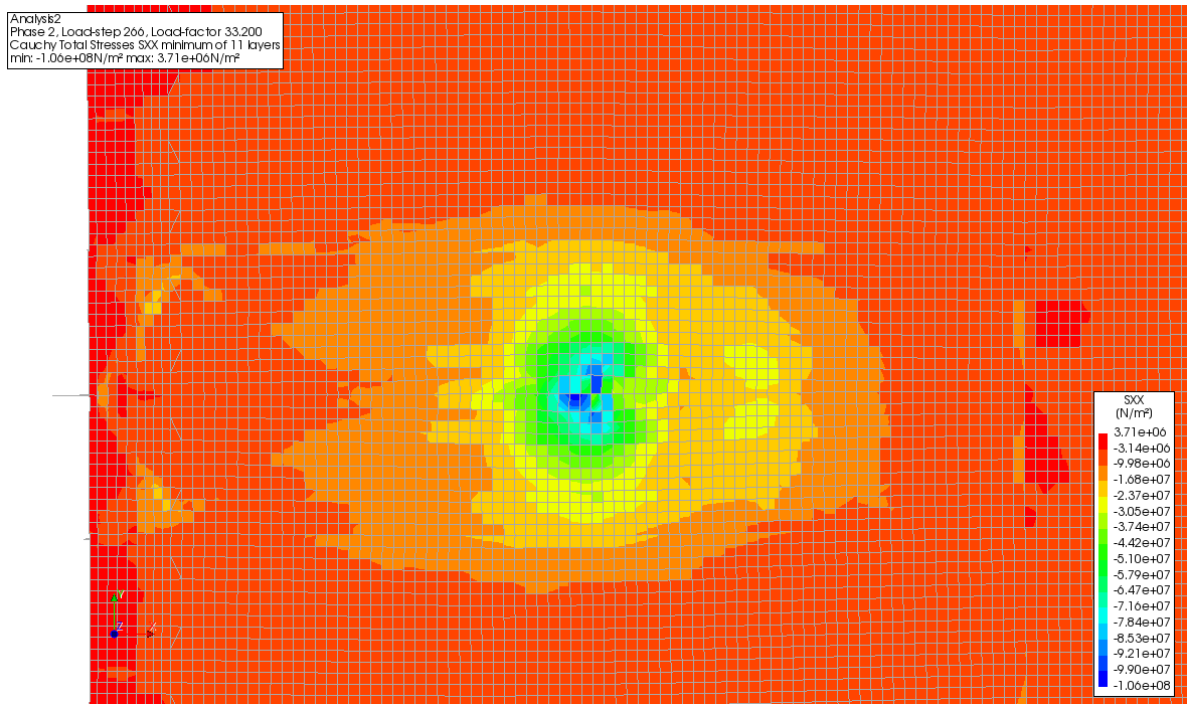

(b) Concrete stress SXX after collapse

Figure 5.14: Concrete stress SXX (CDCL)

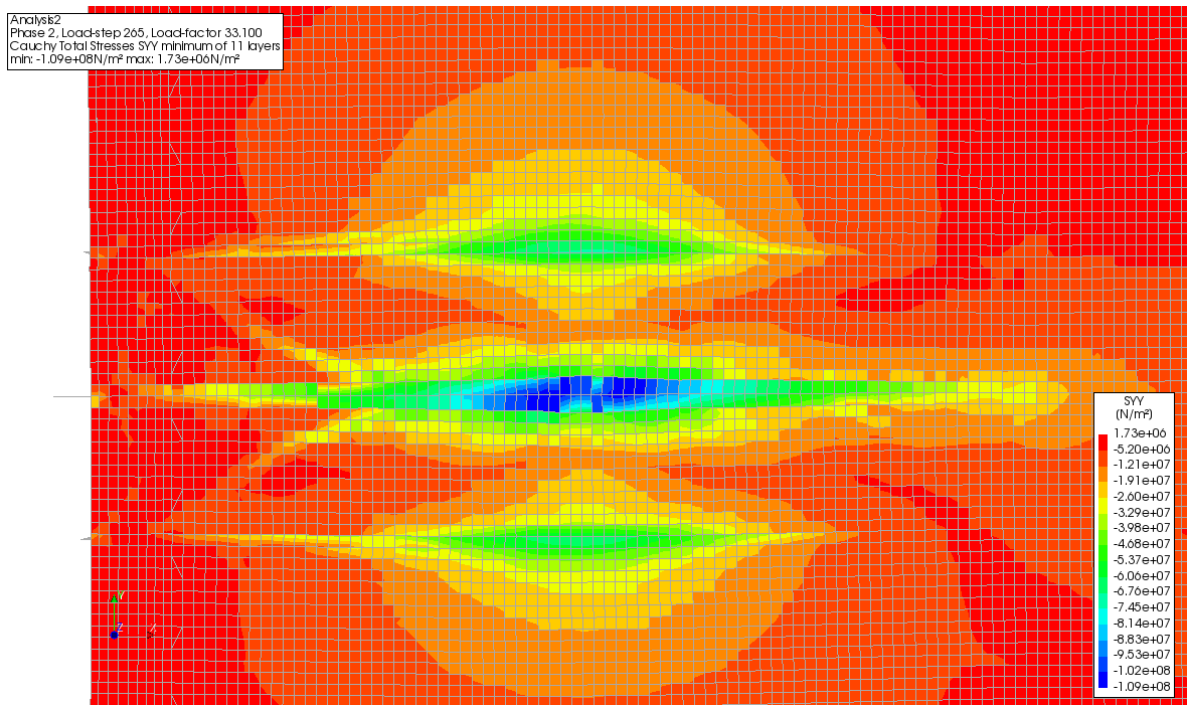

(a) Concrete stress SYY at maximum load

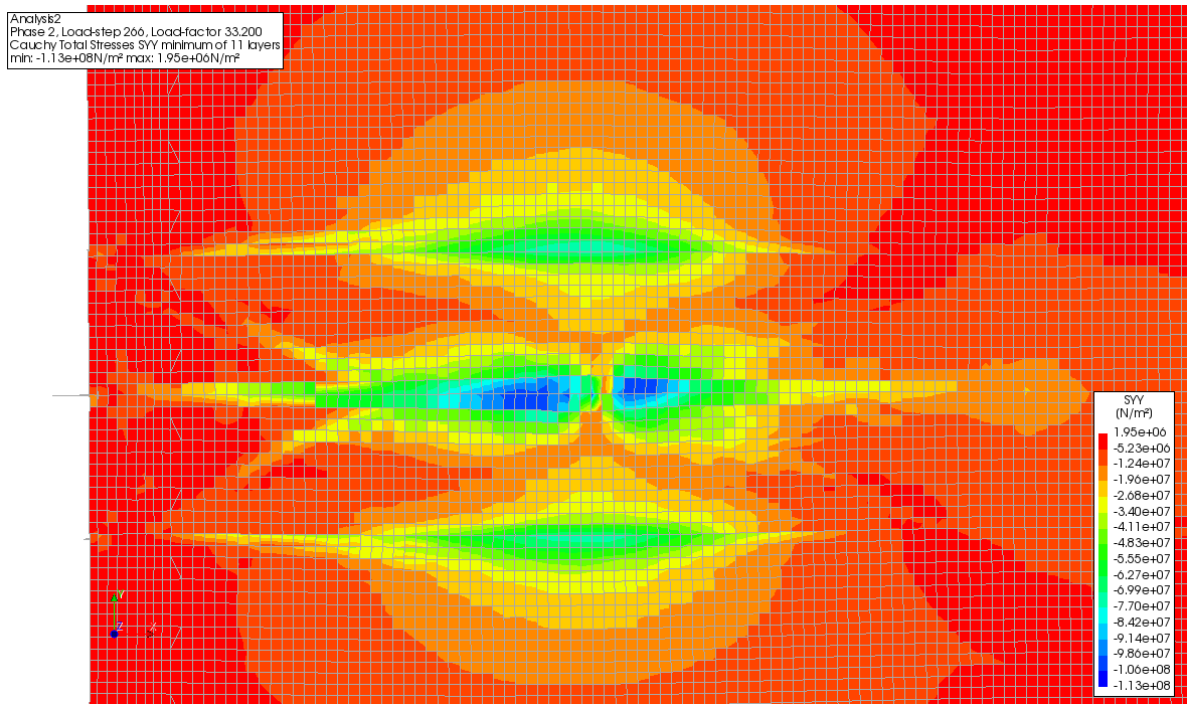

(b) Concrete stress SYY after collapse

Figure 5.15: Concrete stress SYY (CDCL)

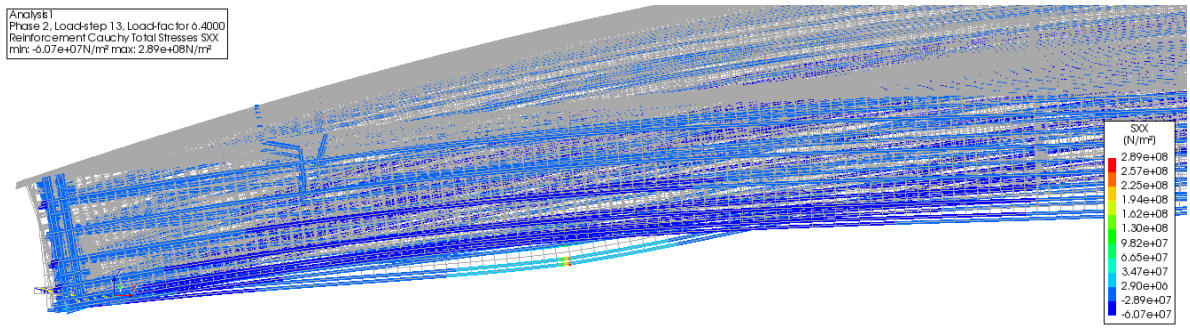

(a) Yielding of longitudinal rebars

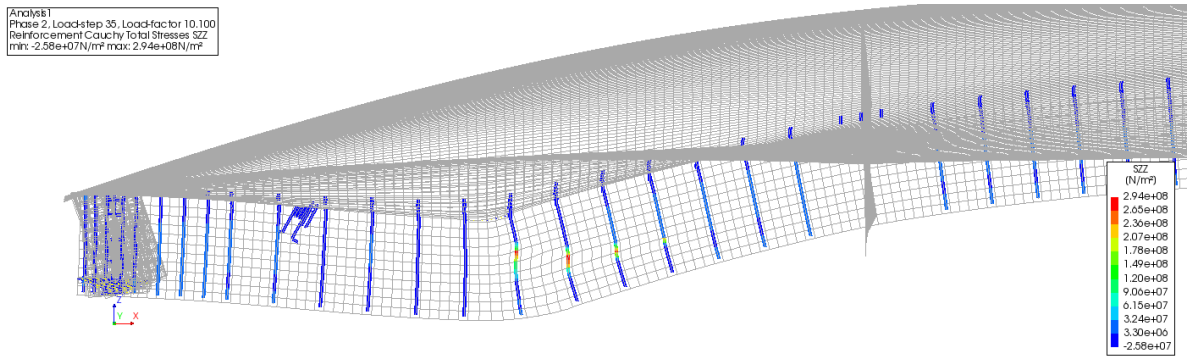

(b) Yielding of stirrups

Figure 5.16: Yielding of rebars (CDCL)

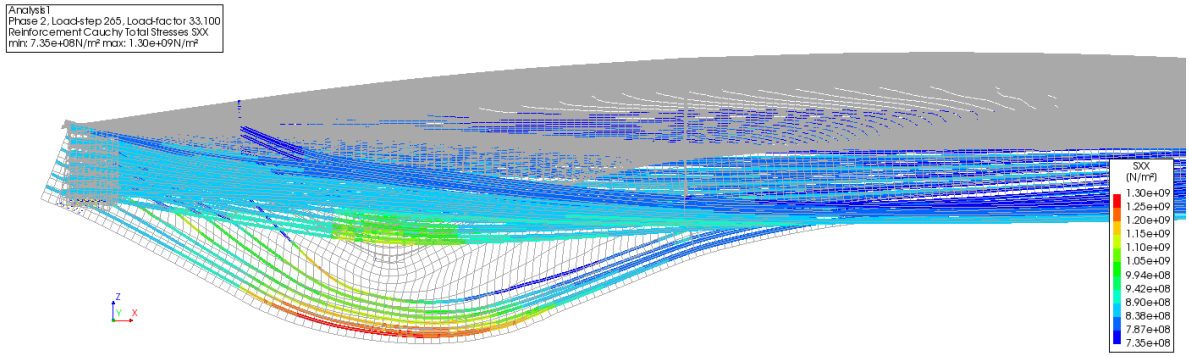

(a) Tensile stresses in longitudinal tendons at maximum load

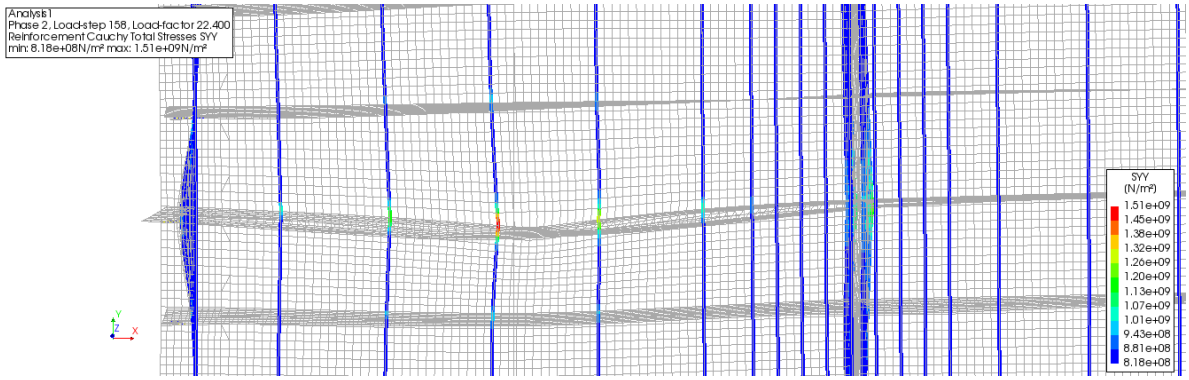

(b) Yielding in transverse tendons (only under the loading plate)

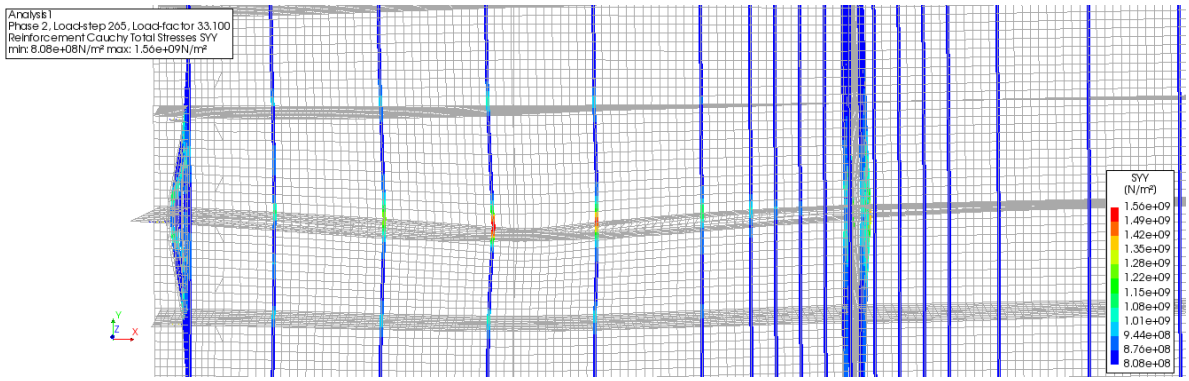

(c) Tensile stresses in transverse tendons at maximum load

Figure 5.17: Tensile stresses in longitudinal and transverse tendons (CDCL)

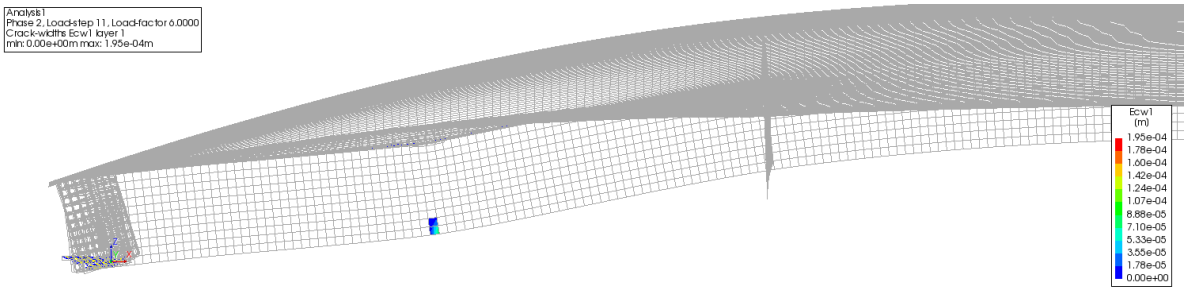

(a) Development of flexural crack

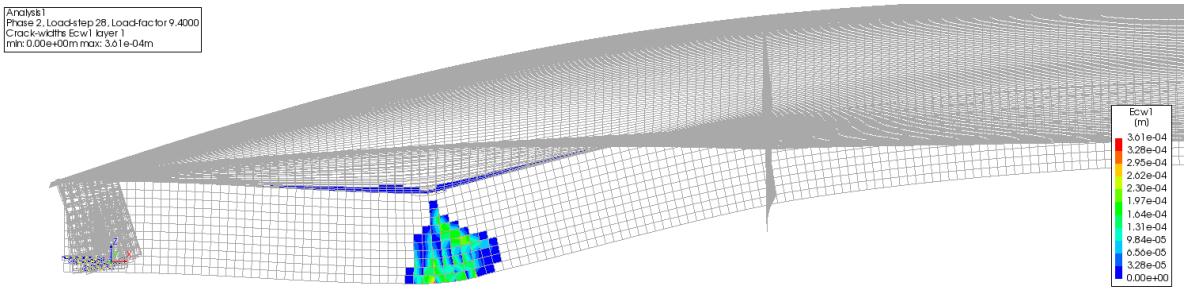

(b) Development of shear crack

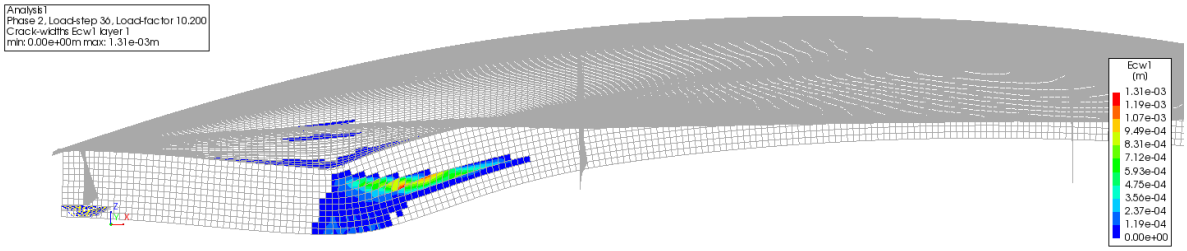

(c) Strain localization of shear crack

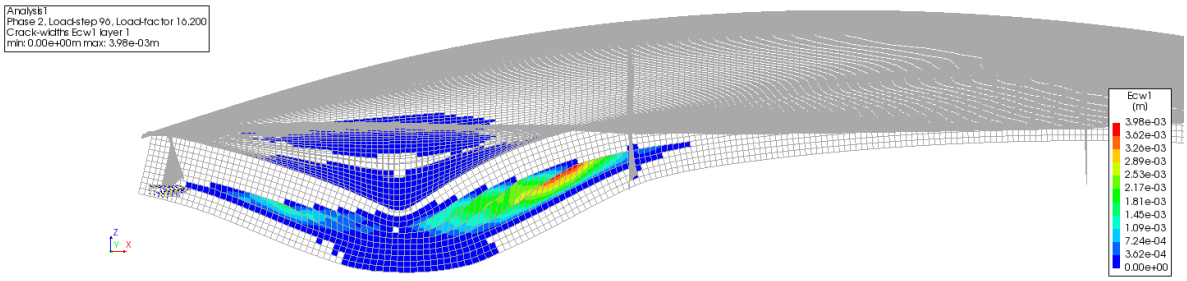

(d) Strain localization of shear crack developing towards support

Figure 5.18: Crack width (CDCL)

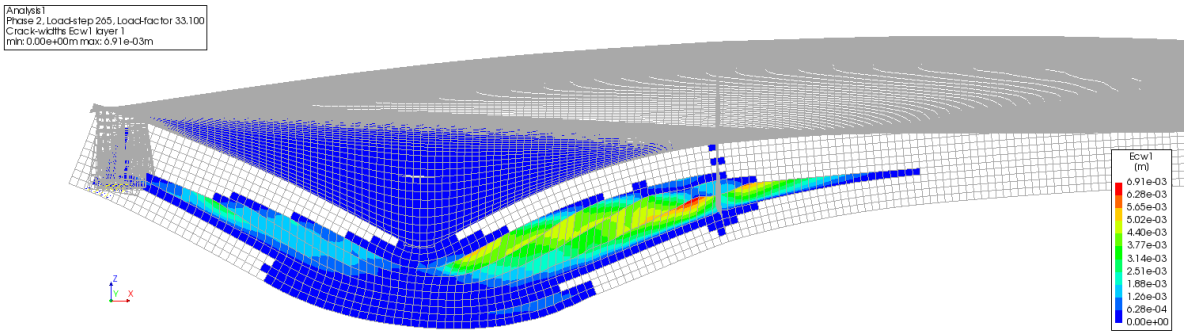

(e) Crack width at maximum load

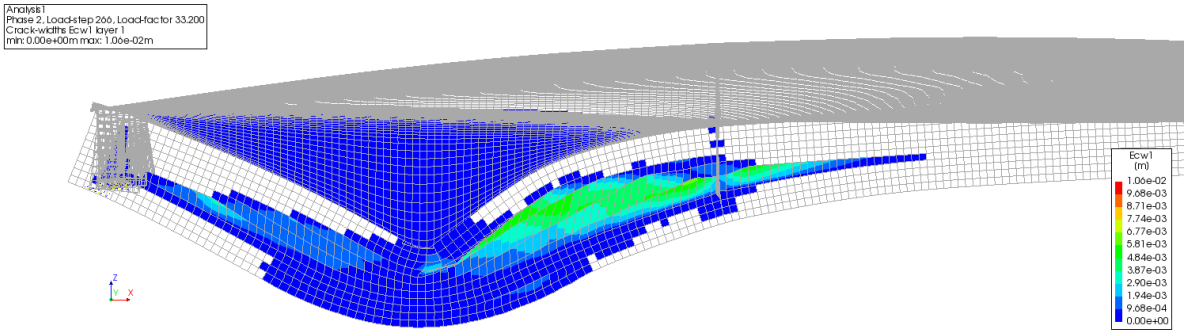

(f) Crack width post collapse

Figure 5.18: Crack width (CDCL)

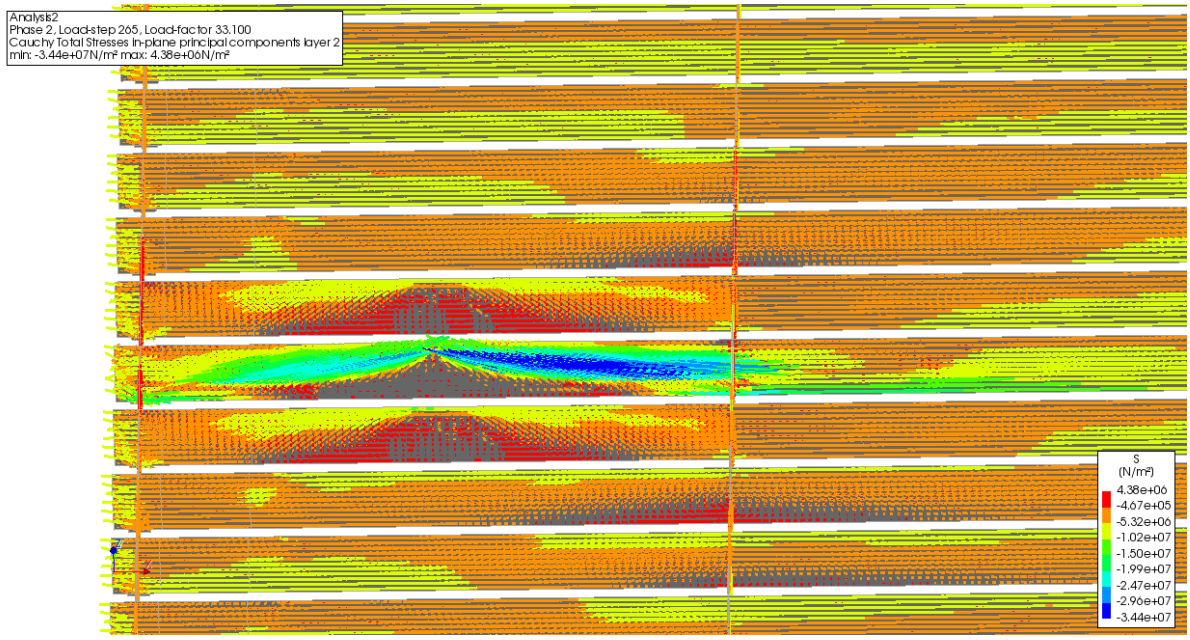

(a) In-plane principal stress components in the girders at maximum load

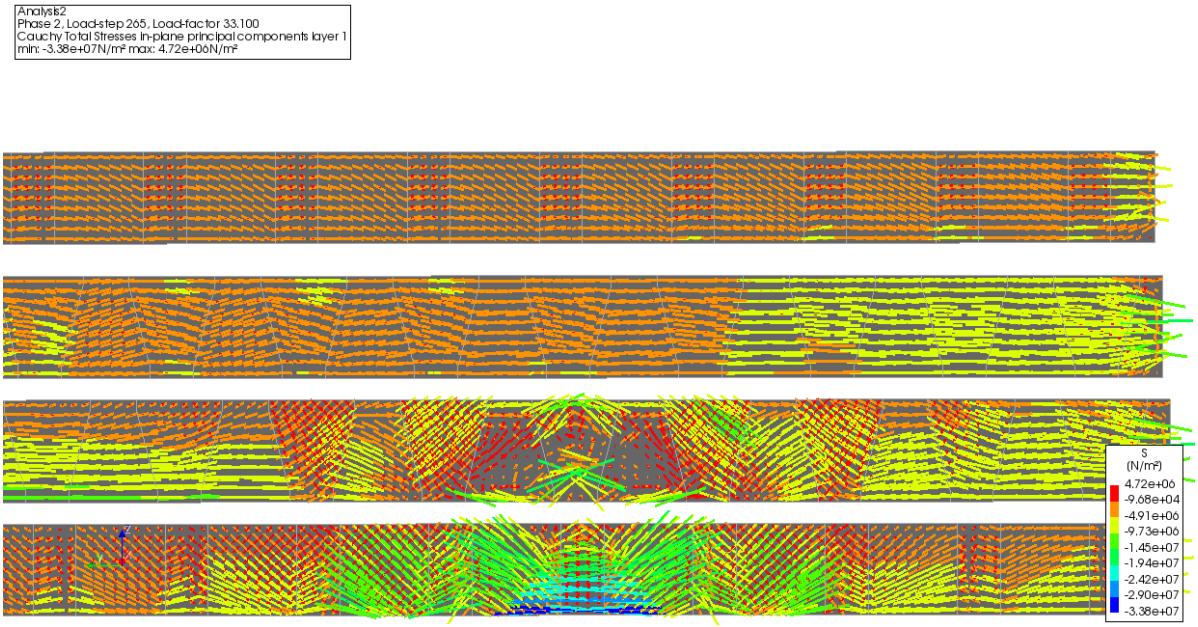

(b) In-plane principal stress components in the cross beams at maximum load

Figure 5.19: In-plane principal stress components in the girders and cross beams (CDCL)

5.2.2. Verification with collapse test data

The results of the numerical analysis are verified by comparing them with the performed measurements (see Figure 3.10) of the field test in Table 5.5. For test 1, the deflection under the load was not only measured at the bottom of the loaded beam (number 11), but also at the bottom of the two adjacent beams on either side (beams 9, 10, 12 and 13) and also the cross beam. The data shows again that the numerical model has an overly stiff and especially ductile response. However, the relative overestimation of the deformation is greater than the IBCL model. The overestimation of the deformation decreases moving away from the point of load application. The strain especially is much greater than the measured value. Reviewing the comparison of the load-displacement curves (Figure 5.20) show two curves that are not in agreement except for the collapse load, which has the same overestimation as the IBCL model. The most obvious difference is in the stiffness during the linear elastic phase. The NLFEA stiffness is too low but a clear linear elastic path can be seen in the first part of the graph. The curve of test 1 is steeper but it's angle is decreasing thus non-linear from the start. In addition, the decrease in stiffness of the NLFEA curve keeps exceeding the collapse test curve. Finally, the response of the NLFEA is too ductile resulting in a great overestimation of the deflection.

Table 5.5: Verification of CDCL results with collapse test 1 data

Measurement	Collapse test 1	CDCL	Difference
Collapse load [N]	$3{,}00 \cdot 10^{6}$ N	$3{,}35 \cdot 10^{-3}$ N	12%
Deflection under beam 9 [m]	$8{,}10 \cdot 10^{-3}$ m	$9{,}06 \cdot 10^{-3}$ m	12%
Deflection under beam 10 [m]	$1{,}20 \cdot 10^{-2}$ m	$1{,}52 \cdot 10^{-2}$ m	26%
Deflection under load beam 11[m]	$2{,}12 \cdot 10^{-2}$ m	$3{,}31 \cdot 10^{-2}$ m	56%
Deflection under beam 12 [m]	$1{,}27 \cdot 10^{-2}$ m	$1{,}63 \cdot 10^{-2}$ m	28%
Deflection under beam 13 [m]	$9{,}00 \cdot 10^{-3}$ m	$1{,}08 \cdot 10^{-2}$ m	19%
Deflection at cross beam [m]	$1{,}50 \cdot 10^{-2}$ m	$2{,}24 \cdot 10^{-2}$ m	50%
Strain over 1 m at failure [-]	$1{,}20 \cdot 10^{-3}$ –	$2{,}45 \cdot 10^{-3}$ –	104%
Deflection at support at failure [m]	$9{,}400 \cdot 10^{-3}$ m	$9{,}19 \cdot 10^{-3}$ m	−2.25%

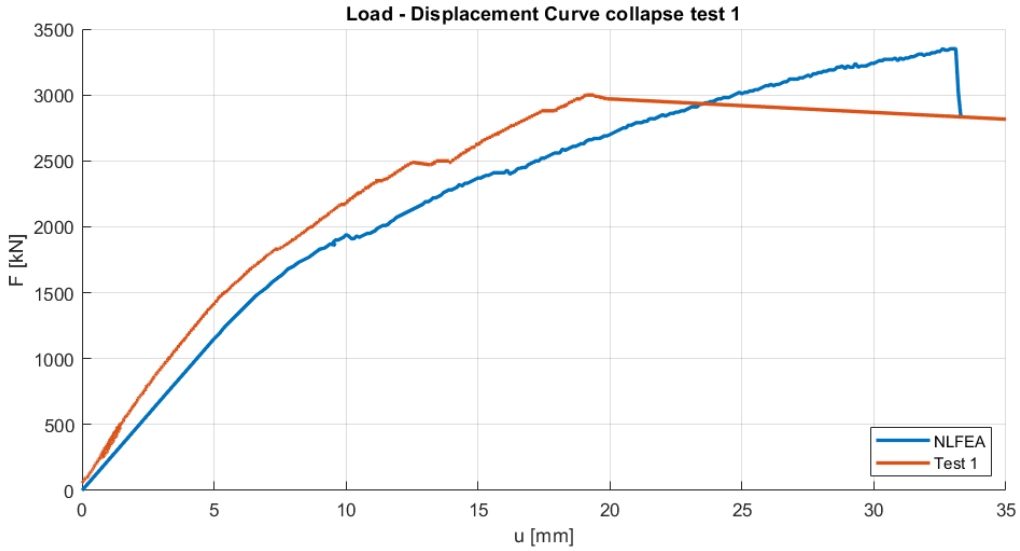

Figure 5.20: Comparison of the load-displacement curve of the field test 1 and non-linear finite element analysis

5.2.3. Transverse load distribution

In collapse test 1, the deflection of the two adjacent beams on each side is measured. The locations are shown in Figure 5.21. To demonstrate the effect of transverse load distribution, the load-deflection curves of the adjacent beams are investigated. Figure 5.23 shows that the load spreading reduces with

increasing load. This effect starts after approximately at 50% of the collapse load has been applied. Also the change in support reactions due to the application of the concentrated load has been determined for the support on the side closest to the applied load. The results show how the applied load is divided across the adjacent beams and are considered relative to the support reaction of the loaded beam. Figure 5.23 shows that up to 10 mm displacement, the lateral load spreading is constant. However, beyond the 10 mm displacement with increasing load the lateral spreading reduces. This reduction is just a few percent for the adjacent beams 10 and 12, but moving away from the applied load it is much more pronounced. When we consider the deflection of the adjacent beams in table 5.6, we can also see that the lateral load spreading in the CDCL analysis is much lower compared to the collapse test number 1.

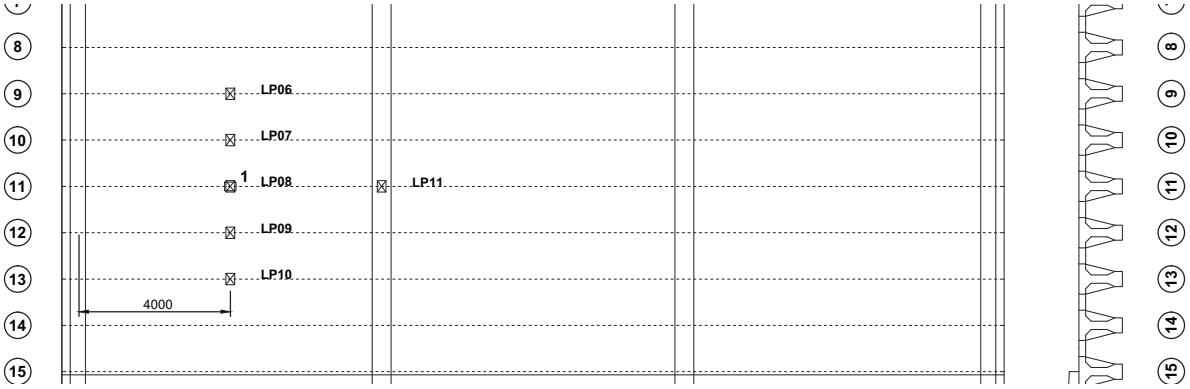

Figure 5.21: Top and side view of span 4, test 1, location of vertical deflection sensors for test 1

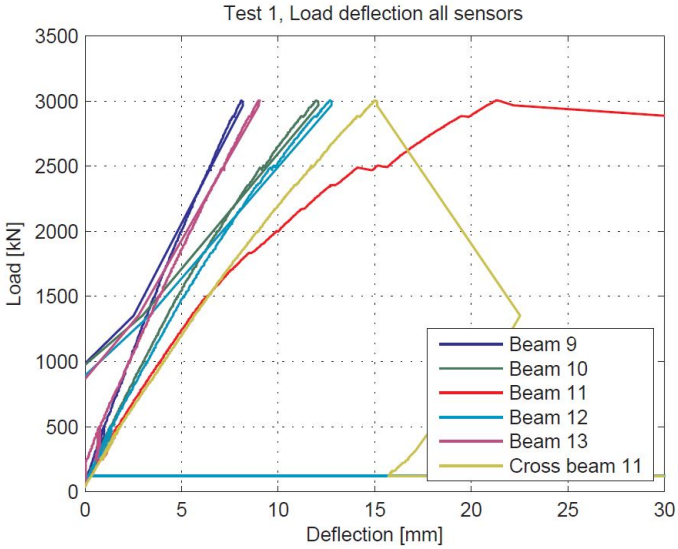

Figure 5.22: Load Deflection all sensors adjacent to loading plate test 1[18]

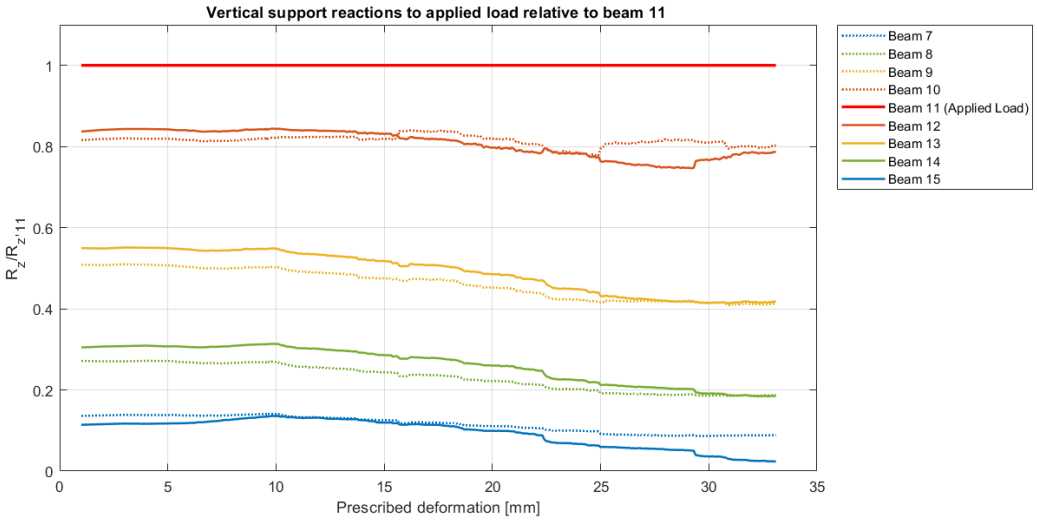

Figure 5.23: The changes in the vertical support reactions of adjacent beams to the load application relative to beam 11

Table 5.6: Comparison of transverse load distribution of collapse test 1 and NLFEA

Measurement	Collapse test 1	Relative to beam 11	NLFEA CDCL	Relative to beam 11	Difference
Deflection under beam 9	$8{,}10 \cdot 10^{-3}$ m	38%	$9{,}06 \cdot 10^{-3}$ m	27%	−33%
Deflection under beam 10	$1{,}20 \cdot 10^{-2}$ m	57%	$1{,}52 \cdot 10^{-2}$ m	46%	−25%
Deflection under load beam 11	$2{,}12 \cdot 10^{-2}$ m	100%	$3{,}31 \cdot 10^{-2}$ m	100%	–
Deflection under beam 12	$1{,}27 \cdot 10^{-2}$ m	60%	$1{,}63 \cdot 10^{-2}$ m	49%	−22%
Deflection under beam 13	$9{,}00 \cdot 10^{-3}$ m	42%	$1{,}08 \cdot 10^{-2}$ m	33%	−34%

Guyon Massonnet

The transverse load distribution in the numerical analysis is too low (see Table 5.6). Guyon Massonnet is a method which application yields an influence line which describes the transverse distribution of an applied load in a linear elastic response of the structure. The deflection in longitudinal and transverse directions are decoupled in this method. The response to the applied load in the field test and the numerical analysis was evidently non-linear which limits the accuracy of this method. However, the results show that the non-linearity in the transverse direction is very limited. No cracking occurs, only yielding (in the NLFEA) of the transverse tendons after 80% of the load has been applied and it is limited to under the loading plate. The method defines the length as 2a and width as 2b. See Figure 5.24. The load is applied on beam eleven. Nine stations are divided along the width of the deck which will generate points of the influence line. The input for the Guyon Massonnet method is presented in Table 5.7.

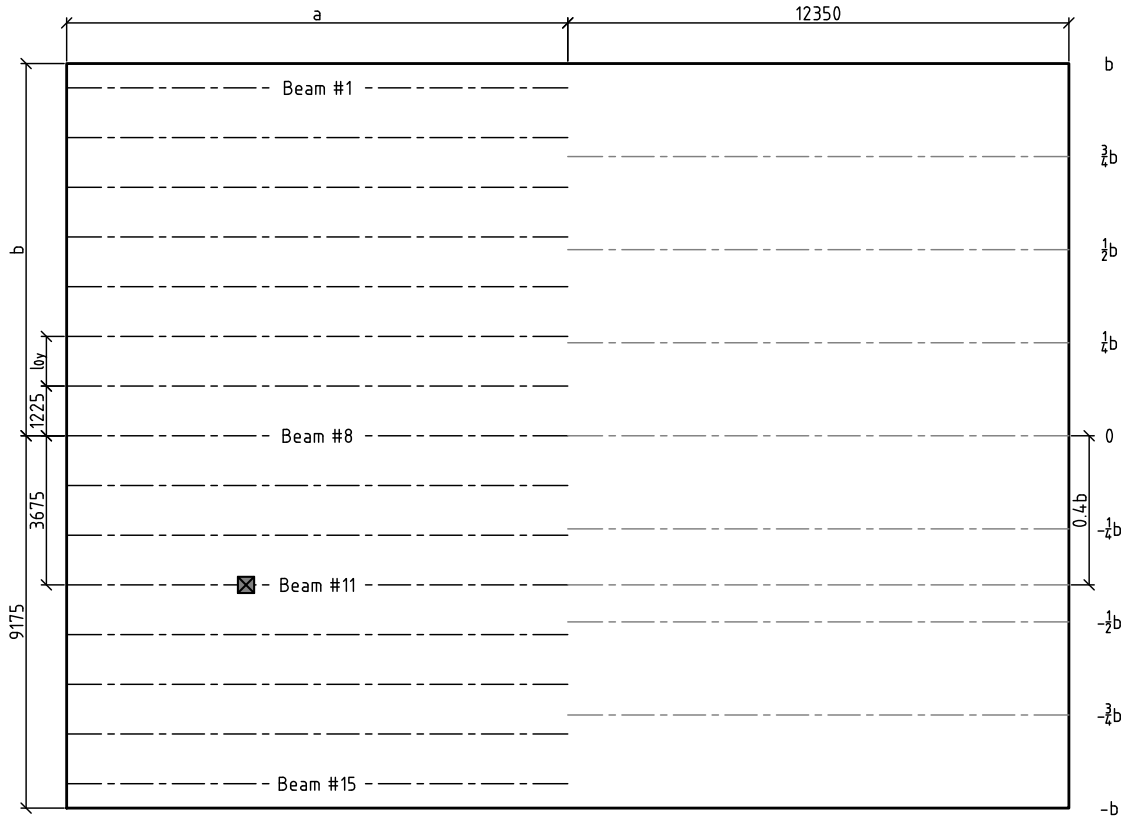

Figure 5.24: Guyon Massonnet deck dimensions and stations positions

Table 5.7: Determination of the input for Guyon Massonet

	Input
width deck (2b)	18.4 m
length deck (2a)	24.7 m
Position beam 11 = $\frac{3675}{9175}$b	0.4b [-]
E_{girder}	$4{,}4722 \cdot 10^{10}$ N/m^2
E_{slab}	$3{,}9497 \cdot 10^{10}$ N/m^2
$I_{xx,girder+slab}$	$7{,}06 \cdot 10^{-2}$ m^4
$I_{xx,girder}$	$6{,}02 \cdot 10^{-2}$ m^4
$I_{xx,slab}$	$1{,}04 \cdot 10^{-2}$ m^4
$I_{yy,slab}$	$1{,}62 \cdot 10^{-1}$ m^4 (Per cross beam section)
$width_{x,girder}$	24,7 m
$width_{y,girder}$	0,80 m
$width_{y,slab}$	0,425 m
$width_{l_{0y}}$	1,225 m
$\Sigma EI_{xx}/m = \rho_x$	$2.53e + 8$ kNm
$\Sigma EI_{yy}/m = \rho_x$	$7.99e + 8$ kNm
$\theta = \frac{b}{2a}\sqrt[4]{\frac{\rho_x}{\rho_y}}$	0.497 [-]

Equation 5.1 gives the relation between the deflection at location y relative to the average deflection.

$$K(\alpha)_v = \frac{w(x,y)}{w_0(x)} = \frac{W(y)}{W_0} \tag{5.1}$$

The FEA results show no cracks in the cross beams or slabs. The partial differential equation has been solved by others for every value of θ and $\alpha = 0$ for the load at every station. Because of the symmetry of the stations this results in five solutions with θ-K-curves for each station. The load at 0.4b can be determined through linear interpolating between the values of $\frac{1}{4}$b and $\frac{1}{2}$b for the right part of the curve and -$\frac{1}{4}$b and -$\frac{1}{2}$b for the left part of the curve.

Table 5.8: K-values for $\theta = 0.497$ and $\alpha = 0$

Location of the applied load	-b	-$\frac{3}{4}$b	-$\frac{1}{2}$b	-$\frac{1}{4}$b	0b	$\frac{1}{4}$b	$\frac{1}{2}$b	$\frac{3}{4}$b	b
$\frac{1}{4}$b	0	0.30	0.63	0.96	1.22	1.38	1.40	1.40	1.40
$\frac{1}{2}$b	-0.54	-0.17	0.22	0.63	1	1.44	1.81	2.07	2.31

which gives the following K-line:

Table 5.9: K-line for $\theta = 0.418$ and $\alpha = 0$ with the load at 0.4b

	-b	-$\frac{3}{4}$bb	-$\frac{1}{2}$b	-$\frac{1}{4}$b	0b	$\frac{1}{4}$b	$\frac{1}{2}$b	$\frac{3}{4}$b	b
0.4b	-0.324	0.018	0.384	0.762	1.11	1.404	1.564	1.668	1.764

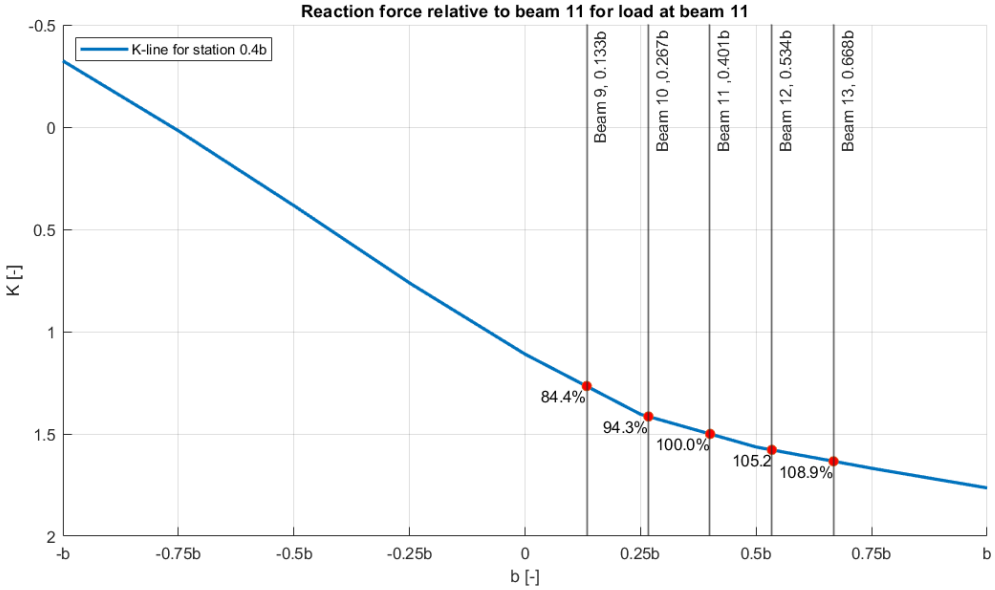

Figure 5.25: Reaction force relative to beam 11 for load at beam 11

Figure 5.25 shows the reaction force of the adjacent beams relative to the reaction force of beam eleven when beam eleven is loaded with the point load. Since the method assumes a linear elastic response, the displacement will be proportional to the applied load c.q. the reaction force on the beam and predict the transverse spreading of the applied load. The comparison shows an overestimation of about 70% in the transverse load distribution for the adjacent beams and 140% for the beams adjacent to those. This is without the inclusion of α (factor to include the torsional stiffness of the deck) which

Table 5.10: Comparison of transverse load distribution of collapse test 1 and Guyon Massonnet

Response	Collapse test 1 Relative to beam 11	Guyon Massonet Relative to beam 11	Difference
Beam 9	38%	84%	121%
Beam 10	57%	94%	65%
Beam 11	100%	100%	–
Beam 12	60%	105%	75%
Beam 13	42%	109%	159%

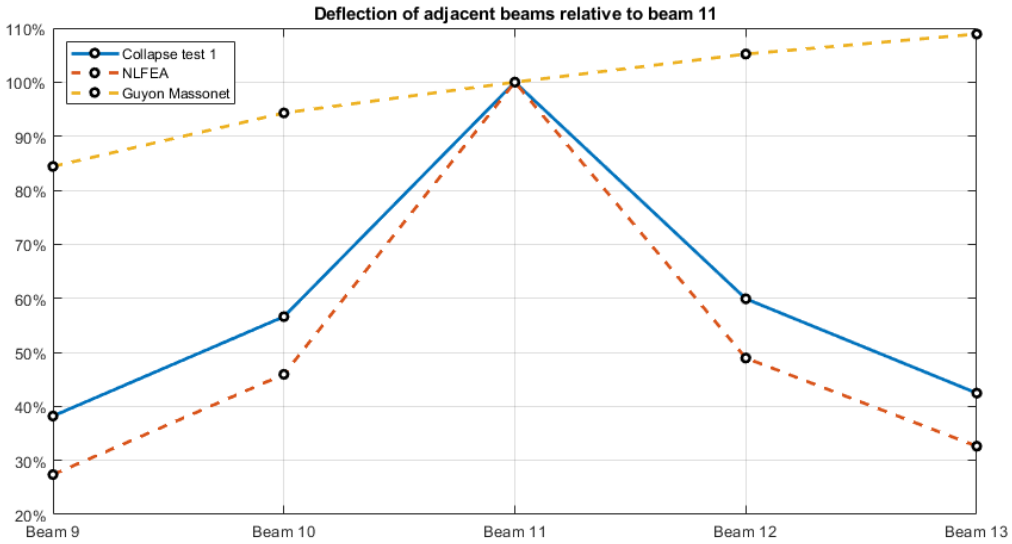

Figure 5.26: Comparison of the transverse load distributions

would made the reaction even less realistic. In Figure 5.26 the deflection of the adjacent beams relative to the loaded beam (beam 11) is presented for the collapse test 1, the NLFEA of test 1 and the Guyon Massonnet method results.

5.2.4. Increase in normal force

The increase in normal force is an indicator of activation of arch action and compressive membrane action[2]. The normal force will be determined for both the longitudinal and transverse directions. DIANA offers the option to add a composite line element to your model with an assigned area. It then calculates the normal force from the stress of each node within the assigned area on the composite line element but unfortunately it does so incorrectly. A pragmatic approach is used to see whether the normal force is increased over the cross section between load steps 7 and 265. After load step 7 the application of the self-weight and the prestressing force is complete. At load step 265 is the maximum load has been achieved. Two cross sections have been evaluated, at 1m left of the loading plate and 1m right of the loading plate and the difference between the load steps is the generated normal force in the cross section. The normal force has two components: the concrete stresses and the stresses in the reinforcement and the tendons.

Transverse direction

The normal force is evaluated in the transverse direction outwards from the loading plate at the centre of the slabs between beams 9 and 13 in the transverse direction with a strip width of 400 mm matching the loading plate.

Table 5.11: Increase of normal forces in the cross sections slab (CDCL)

Slab between beams	Concrete part	Tendons	Reinforcement	Total
9 & 10	$-5{,}90 \cdot 10^6$ kN	$-1{,}95 \cdot 10^7$ kN	$2{,}55 \cdot 10^7$ kN	$1{,}00 \cdot 10^5$ kN
10 & 11	$-1{,}05 \cdot 10^7$ kN	$-2{,}34 \cdot 10^7$ kN	$-2{,}04 \cdot 10^7$ kN	$-5{,}43 \cdot 10^7$ kN
11 & 12	$-1{,}05 \cdot 10^7$ kN	$-2{,}30 \cdot 10^7$ kN	$-2{,}12 \cdot 10^7$ kN	$-5{,}47 \cdot 10^7$ kN
12 & 13	$-5{,}58 \cdot 10^6$ kN	$-1{,}32 \cdot 10^7$ kN	$2{,}68 \cdot 10^7$ kN	$8{,}02 \cdot 10^6$ kN

Table 5.12: Increase of normal forces in the cross sections girder (CDCL)

Location	Concrete part	Tendons	Reinforcement	Total
1 m left of loading plate ($x = 3.45m$)	$-1{,}61 \cdot 10^6$ kN	$9{,}79 \cdot 10^5$ kN	$1{,}31 \cdot 10^5$ kN	$-5{,}00 \cdot 10^5$ kN
1 m right of loading plate ($x = 5.45m$)	$-1{,}19 \cdot 10^6$ kN	$9{,}37 \cdot 10^5$ kN	$1{,}44 \cdot 10^5$ kN	$-1{,}19 \cdot 10^5$ kN

Longitudinal direction

The normal force is evaluated in the longitudinal direction 1 meter before and after the loading plate. These locations are depicted in Figure 5.12.

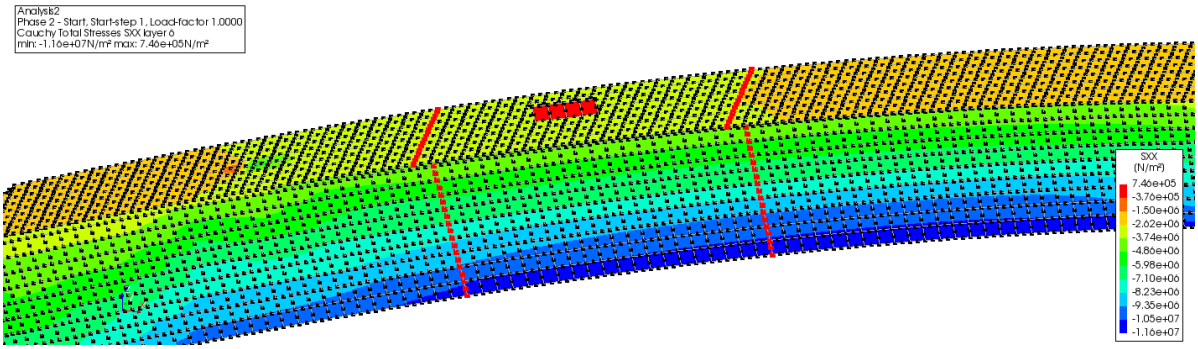

(a) Normal stress SXX after prestressing

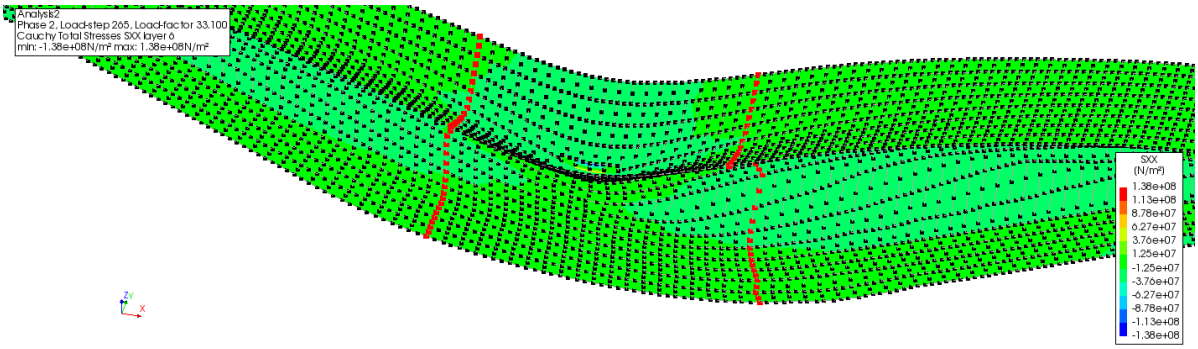

(b) Normal stress SXX after prestressing at maximum load

Figure 5.27: Normal stress SXX (CDCL)

5.3. Model CDTL

5.3.1. Results of the analysis using the non-planar shell mesh

The deformation of the deck is shown in Figure 5.30. The numerical failure is due to crushing of the concrete in the top flange of the girder. The Figure 5.31 shows the crushing of the concrete in x-direction at failure and a reduced stress thereafter. Some elements lost the quadrilateral shape indicating a loss of

stiffness. The Figure 5.32 shows a general reduction in stress and also show a loss of stiffness around the disformed quadrilaterals. The longitudinal rebars start to yield four load steps after the formation of flexural cracks. The yielding of the stirrups occurs fifteen load steps after development of the first shear crack (see Figure 5.33). The start of the yielding of the longitudinal tendons is depicted in Figure 5.34. The transverse tendons do not reaching yielding stress through the simulation. The development of the crack pattern is presented in Figure 5.35. Figure 5.36a shows the localization of strain ocuring in load step 80. The snap-through of load step 80 is matched with a reduction in plasticity and a minor increase in cracking (see Figure 5.29b). The downward deflection combined with the prestressing of the concrete in two directionsl yields a lateral confinement of the concrete, allowing for principal stresses to exceed the uniaxial compressive strength. In Figure 5.37 the nodal values of the principal stresses σ_3 and σ_2 for nodes in which the defined uniaxial compressive strength is exceeded. This procedure was performed for both the girder and the slab concrete.

Table 5.13: Events of the CDTL analysis

Load step	Figure nr.	Event
18	5.35a	Development of flexural cracks
22	5.33a	Yielding of longitudinal rebars in the bottom flange
50	5.35b	Development of shear cracks
65	5.33b	Yielding of stirrups
75	5.34	Yielding of longitudinal tendons
80	5.35c	Strain localization of shear cracks, snap-through behaviour
127	5.31a	Maximum load
128	5.31b	Post collapse, concrete has crushed, non converged solution

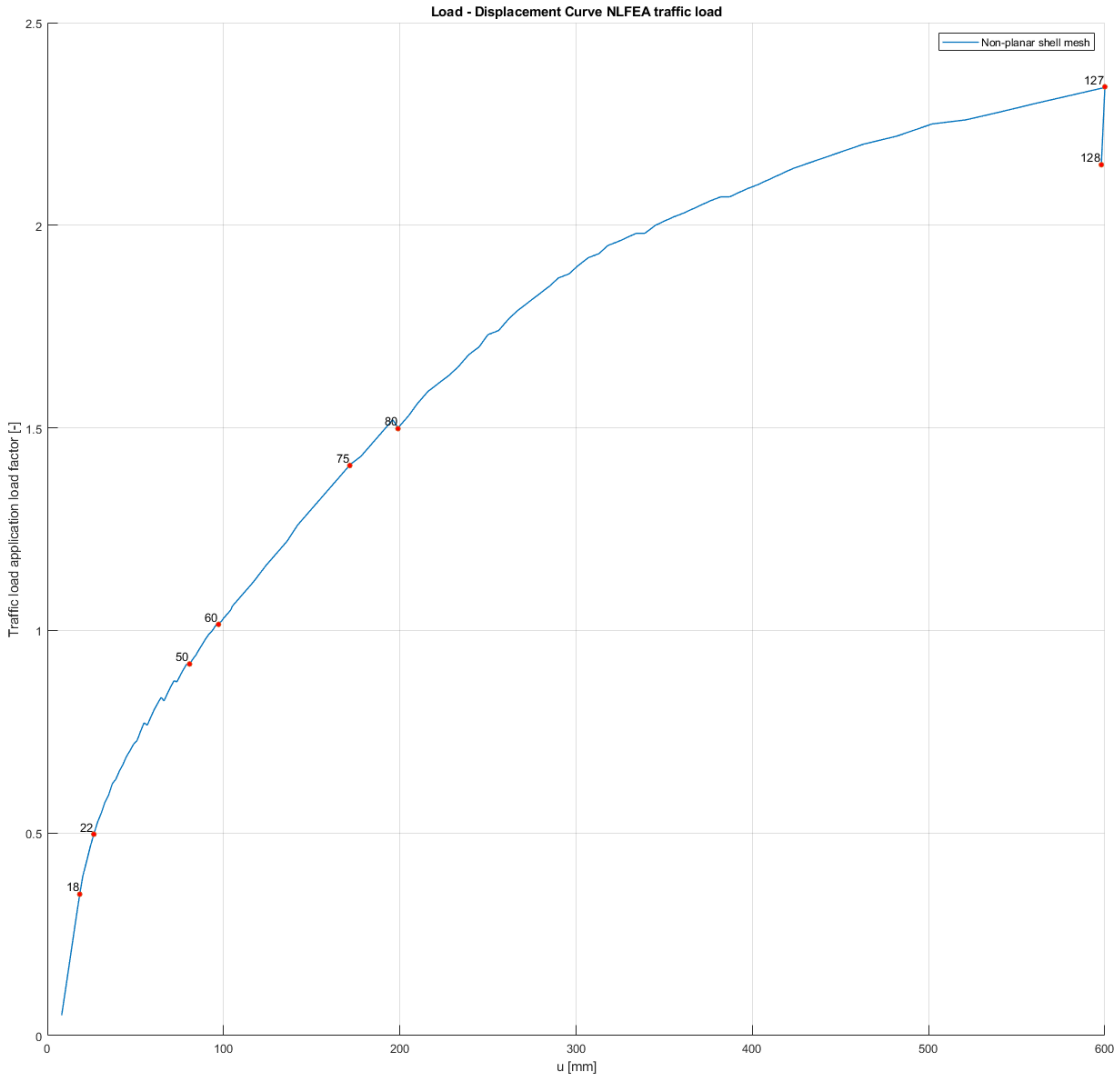

Figure 5.28: Load-displacement curve of the CDTL analysis

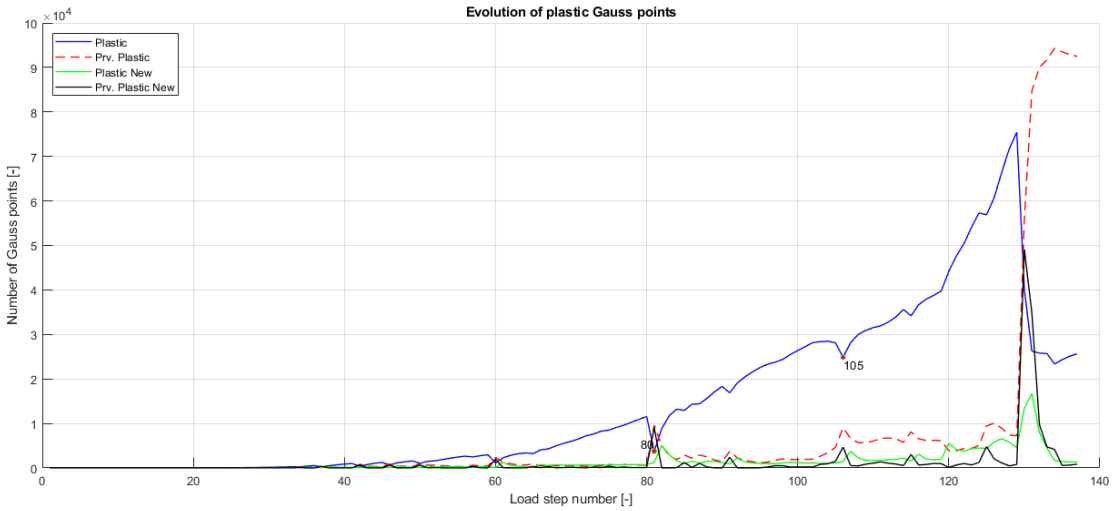

(a) Evolution of the number of Gauss points with (former) plastic behaviour (crushing or yielding)

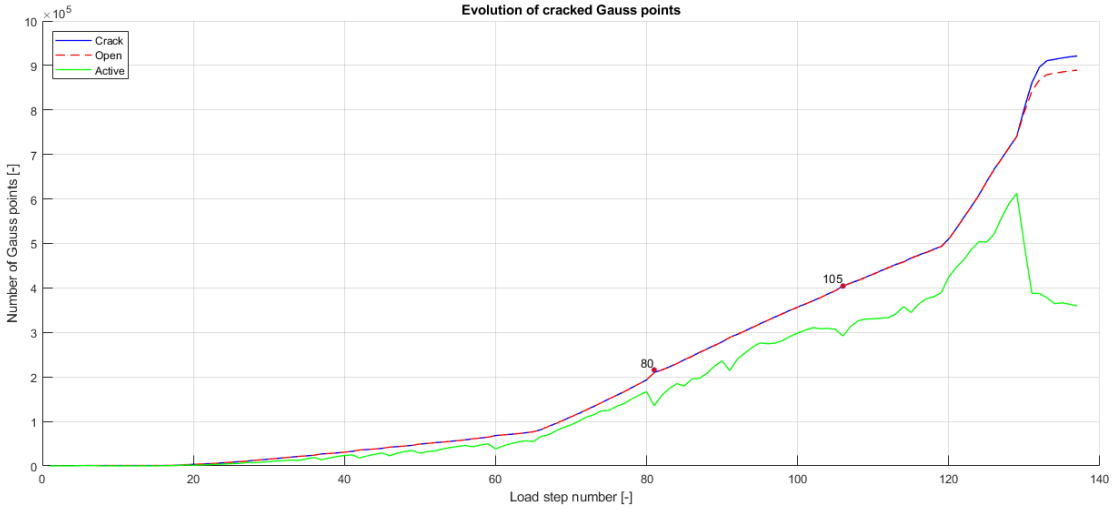

(b) Evolution of the number of cracked Gauss points

Figure 5.29: Gauss point statistics (CDTL)

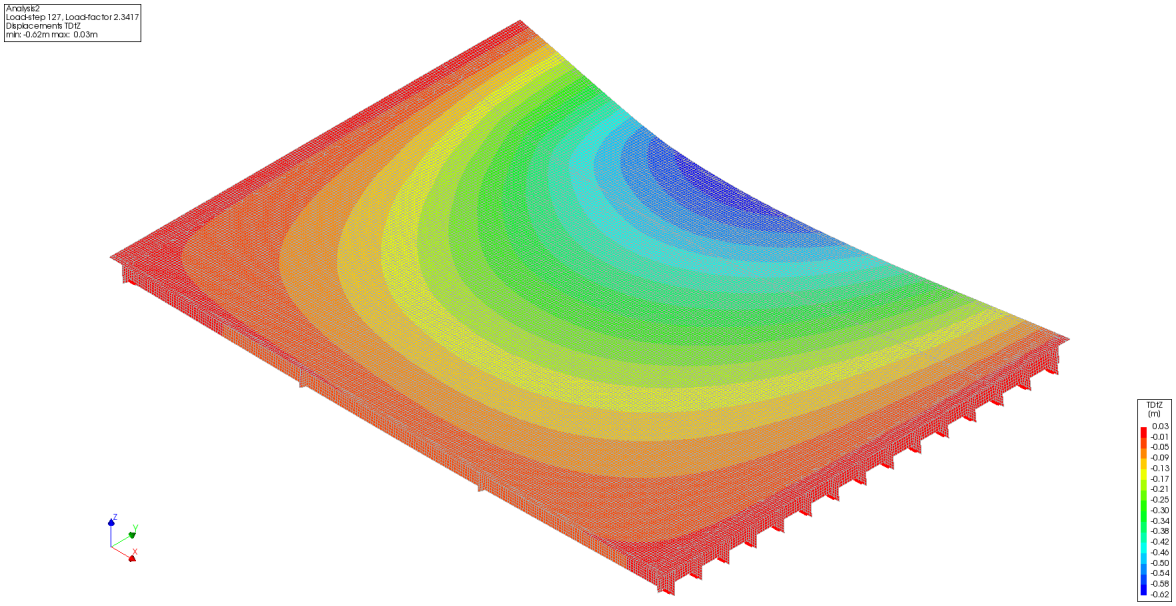

Figure 5.30: Vertical deformation at maximum load

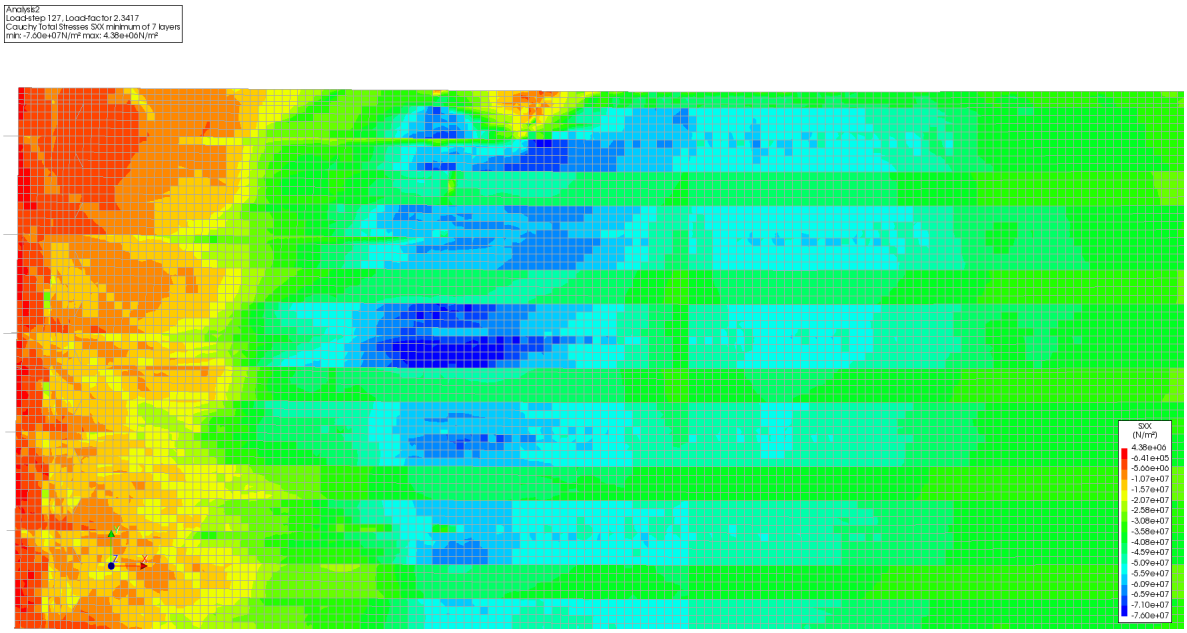

(a) Concrete stress SXX at maximum load

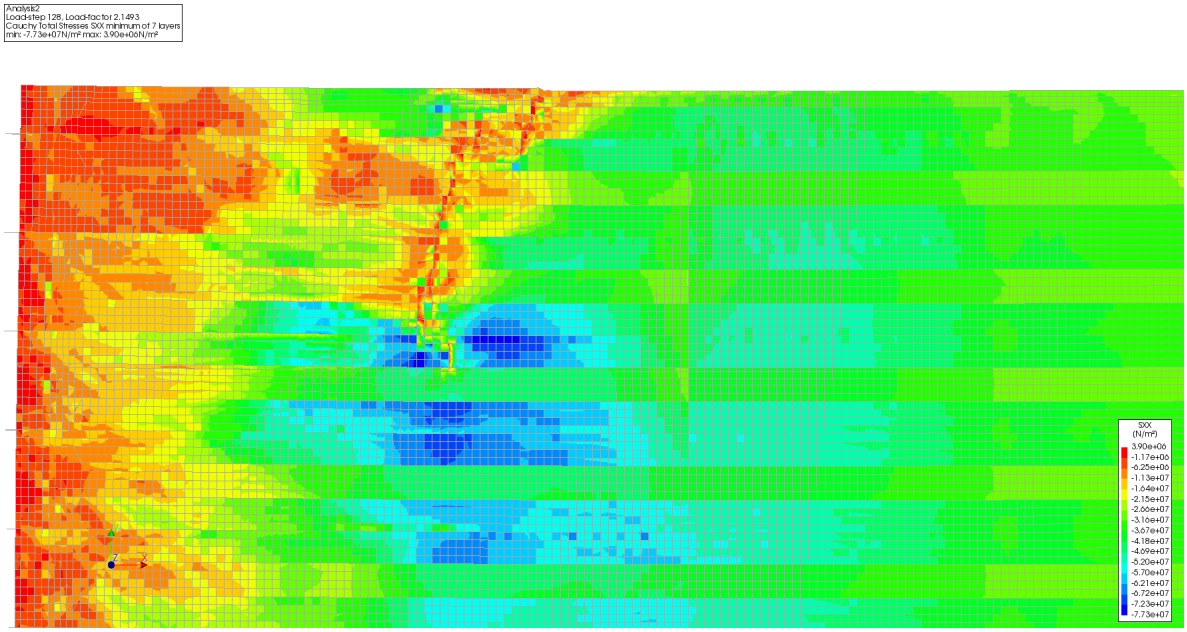

(b) Concrete stress SXX after collapse

Figure 5.31: Concrete stress SXX (CDTL)

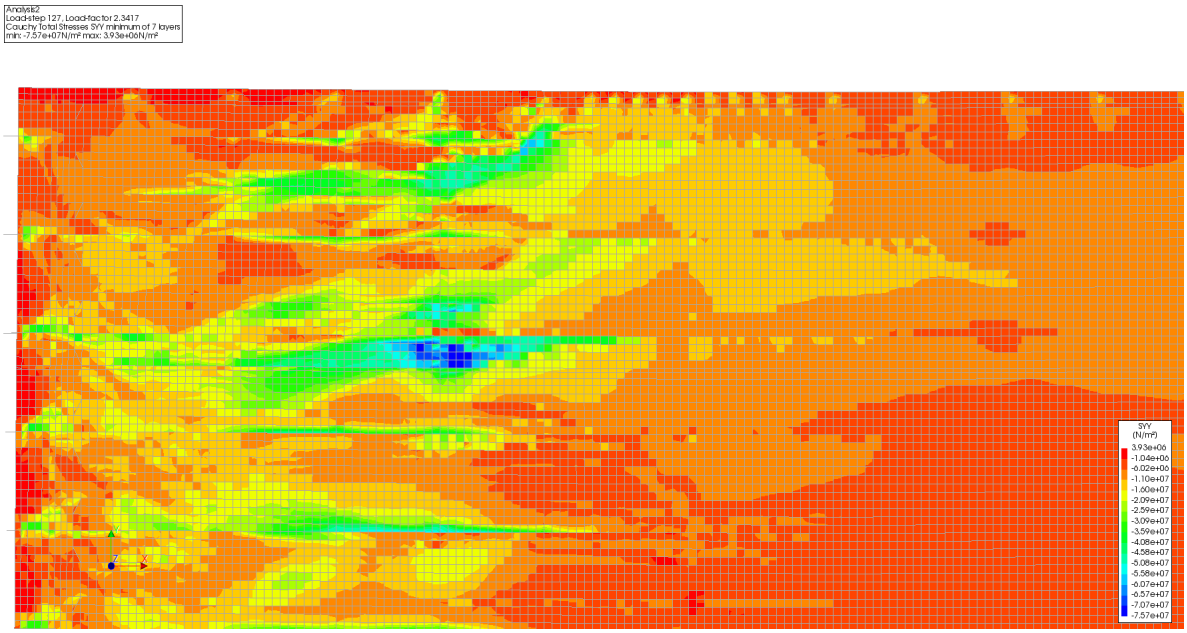

(a) Concrete stress SYY at maximum load

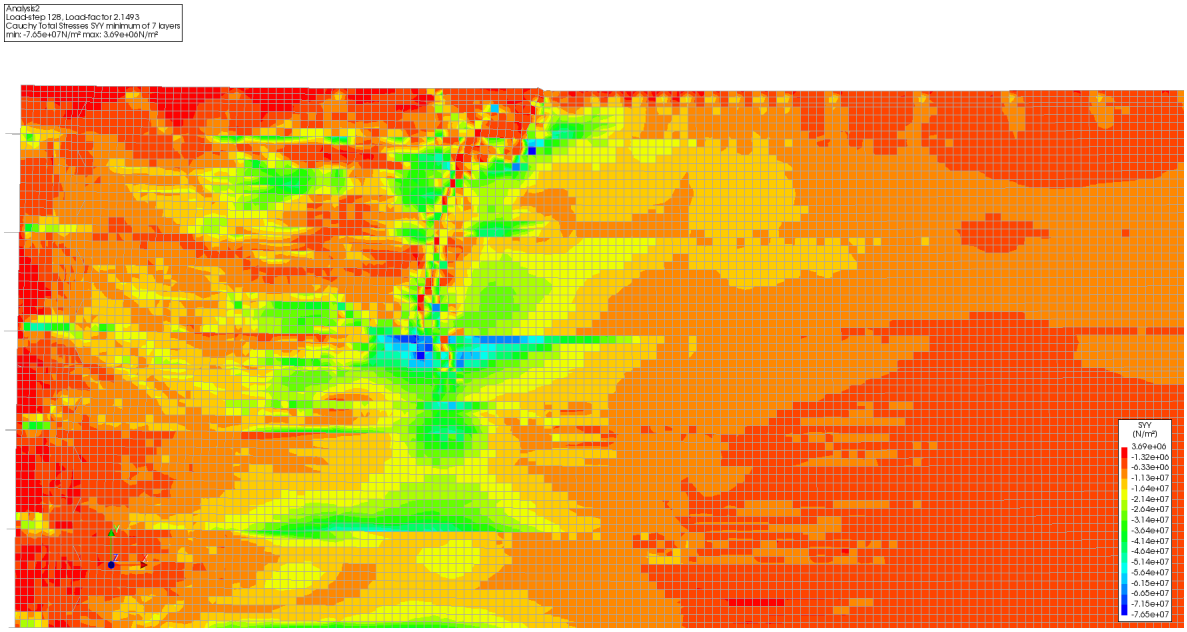

(b) Concrete stress SYY after collapse

Figure 5.32: Concrete stress SYY (CDTL)

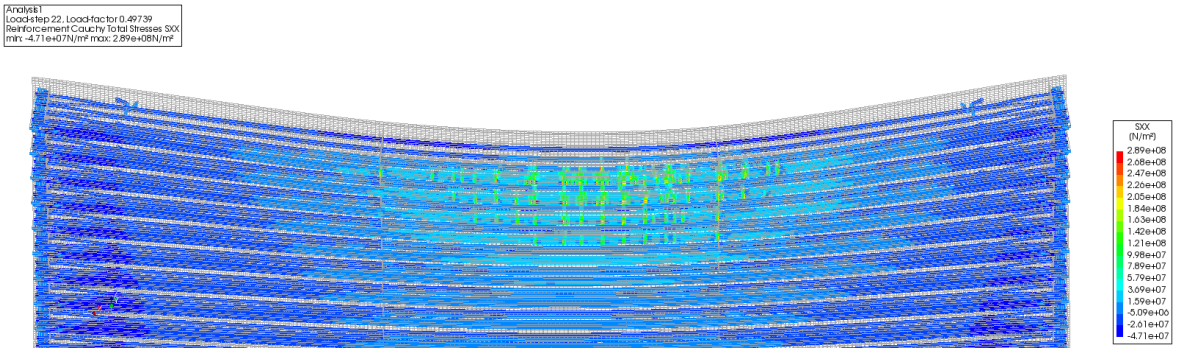

(a) Yielding of longitudinal rebars

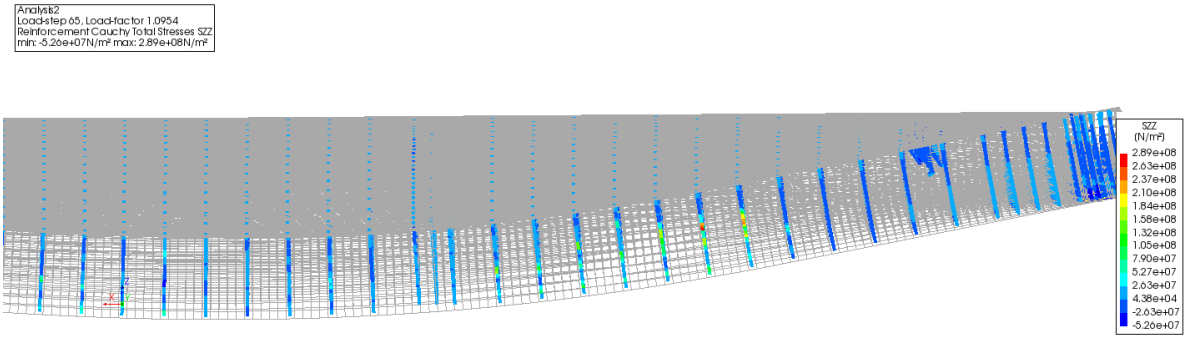

(b) Yielding of stirrups

Figure 5.33: Yielding of rebars (CDTL)

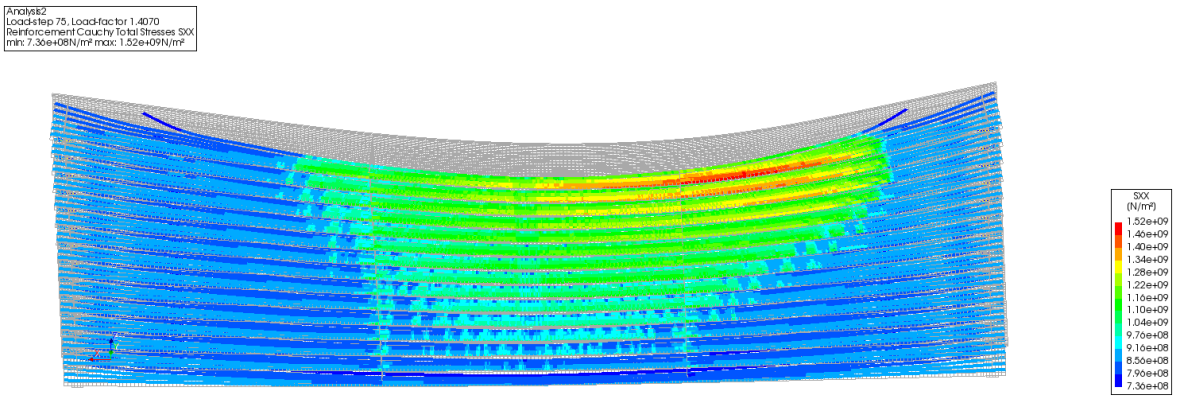

Figure 5.34: Yielding of the longitudinal tendons (CDTL)

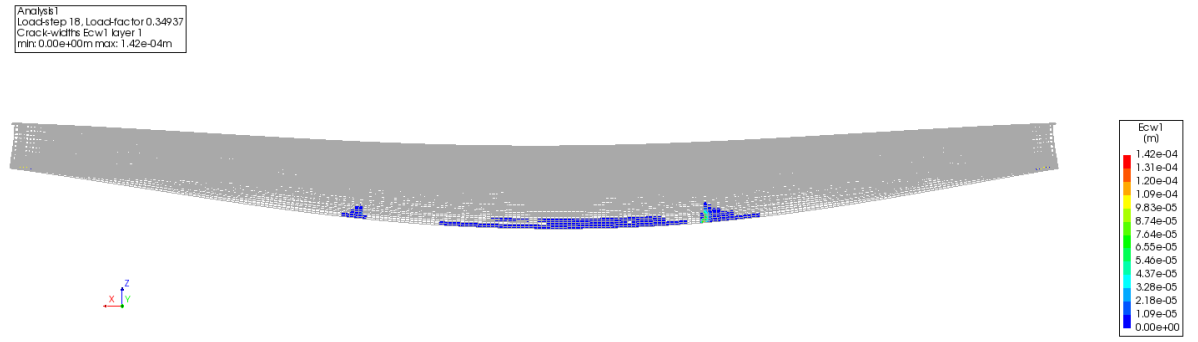

(a) Development of flexural crack

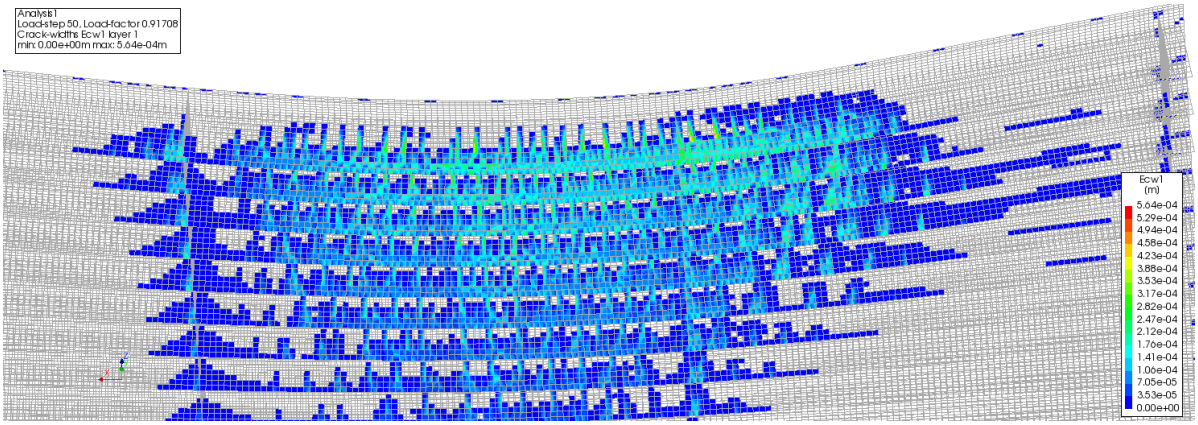

(b) Development of shear crack

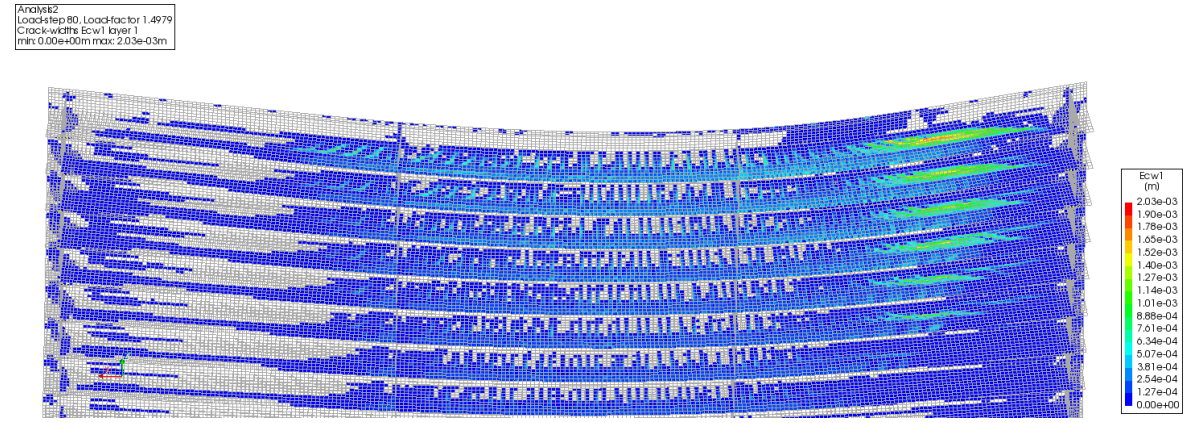

(c) Strain localization of shear cracks

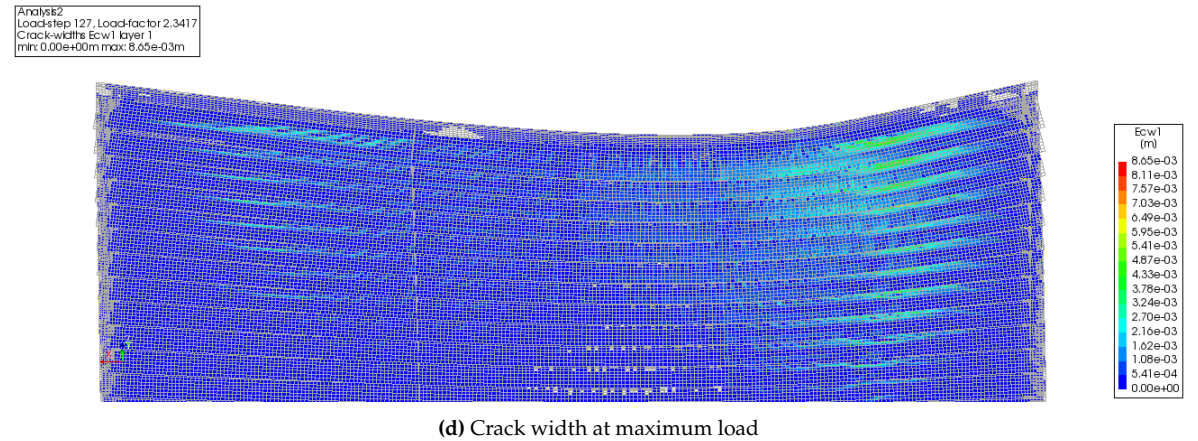

(d) Crack width at maximum load

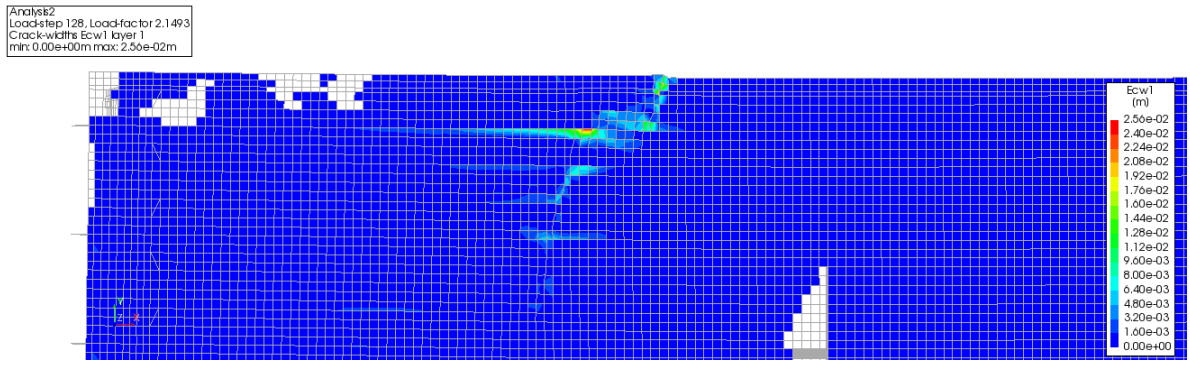

(e) Crack width post collapse

Figure 5.35: Crack width (CDTL)

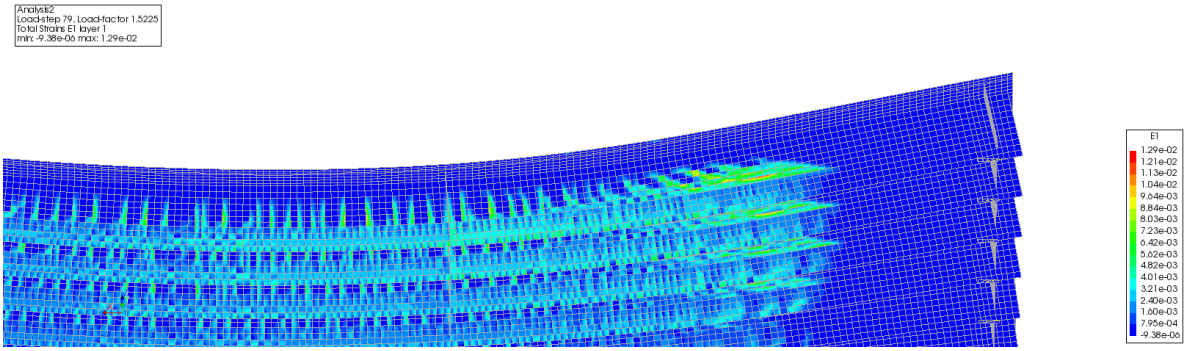

(a) Principal strain

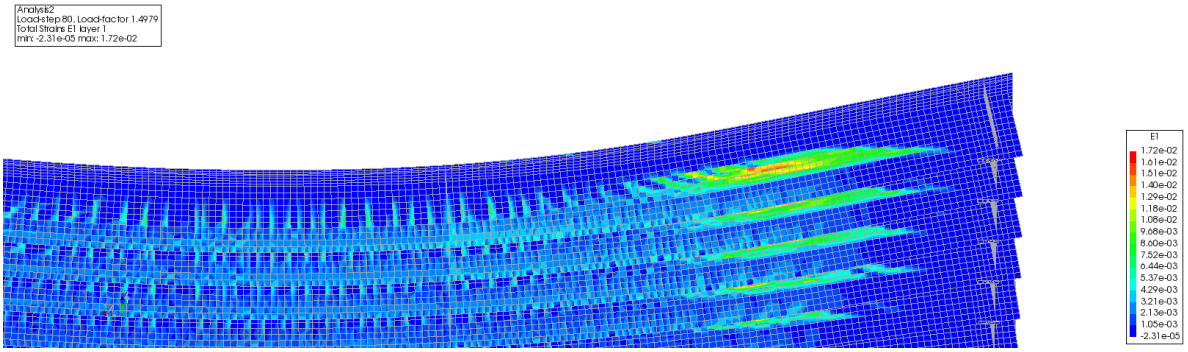

(b) Principal strain after strain localization

Figure 5.36: Principal strain localization (CDTL)

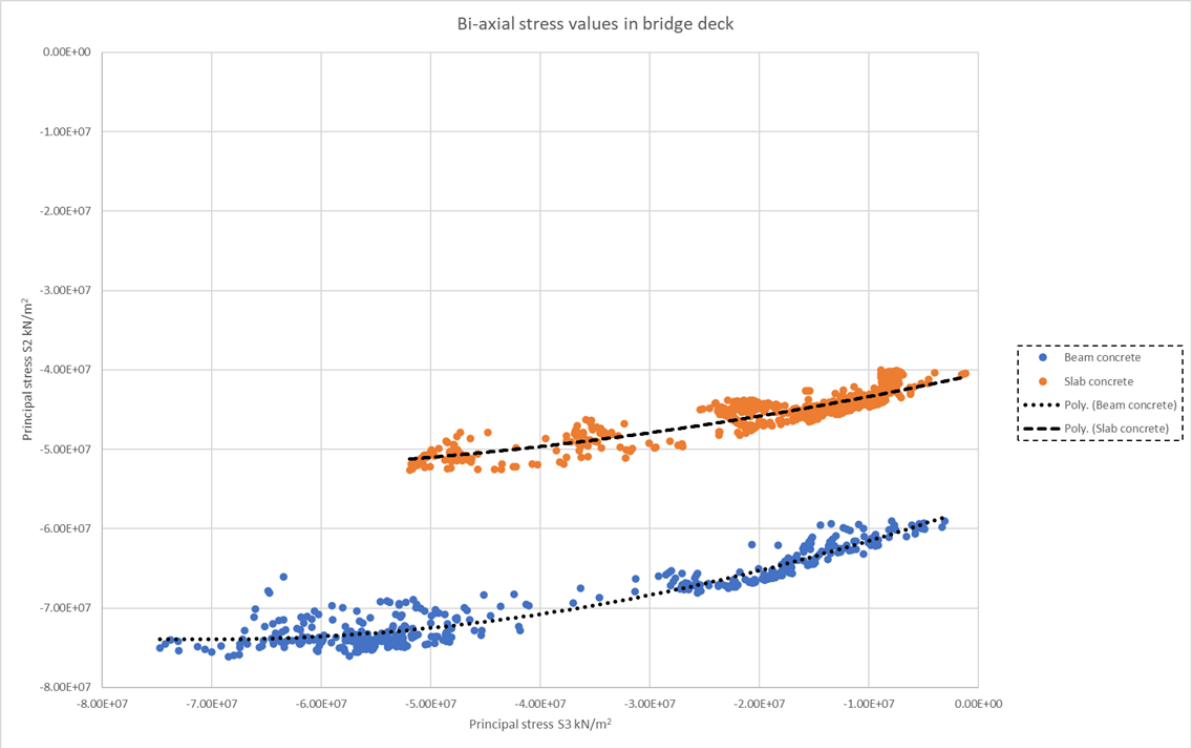

Figure 5.37: Principal stresses σ_2 and σ_3 exceeding the uniaxial compressive stress due to confinement

5.4. Discussion

5.4.1. Model IBCL

In this section the results of the numerical models are reviewed with the research questions in mind. The results of the first model (load-deflection) are compared to other NLFEA by Mustafa[21] and Ensink[12] in Figure 5.10 and Table 5.3. We can see that there is very little difference between the models with meshes consisting of different element types including 3d solid elements. The collapse load differs 5% at most and the displacement under 6%. Mustafa created numerical models of the collapse test 4 & 6 with the applied load at a distance of 2.25 m from the support compared to the 4.0 m of test 7. Figure 5.38 from his thesis[21] shows the results with different mesh types again being in agreement with each other.

We can assess the accuracy of the IBCL model by reviewing Figure 5.9 and Table 5.2. The departure from the linear-elastic branch is a little too sudden compared to test 7. From there the numerical results match the test data perfectly until load step 50 with a load factor of 0.88. From there on, the model does not match the reduction in stiffness from the collapse test and the numerical analysis overestimates the collapse load by 15%. We must take into account the unloading-reloading of the field test which more than likely yielded in a small reduction of the collapse load. Considering the deflection we can see that the numerical response is too ductile with with an overestimation of 18%. When we take another look at Figure 5.38 with the load-displacement curves for tests 4 & 6, we see that instead of an overestimation of the collapse load, we now have an underestimation of the collapse load for all element types for the recreation of test 6. We can see that both collapse tests show a more gradual departure from the linear elastic branch and then a higher rate of reduction of stiffness compared to the numerical models.

The crack pattern development resembles the real crack pattern quite well. The failure mode of the IBCL model was due to crushing of the concrete in the top flange but major shear crack was present as well. The measurement report[18] states that the failure mode was shear but the single photo also shows the crack continuing into the top flange and even the slab concrete meaning crushing of the concrete could have occurred in addition to the shear failure.

Test 7 resulted in a collapse load of 1022 kN. The field test report [10] shows in an analytical assessment that the collapse load is 751 kN with shear bending as the failure mode. An underestimation of the prestressing forces is suggested as a possible cause. The horizontal support reaction of $1.64e + 6$N shows that there is a lateral restraint equal to four prestressing tendons. Combined with the flexural cracks and the vertical displacement of the loading plate means evidence of the presence of arching.

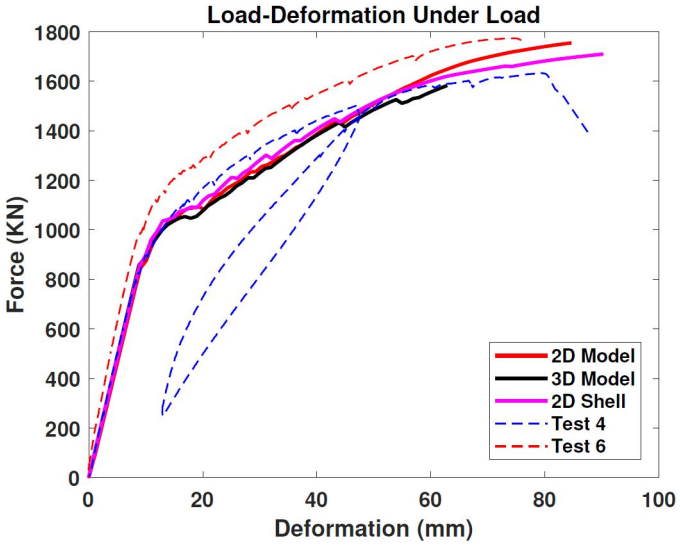

Figure 5.38: NLFEA Mustafa: Load-Deformation under load

5.4.2. Model CDCL

The development of the shear crack in the web towards the cross beam instead of towards the support is the most striking difference with the collapse test 1. However, the report of the field test[10] tells us that for both tests 1 and 2 a shear crack occurred towards the cross beam first and afterwards a new shear crack towards the support. No explanation was given in that report why this happened but it does mean that the initial crack pattern development in the CDCL model was correct. Also the second shear crack towards the support occurred in the numerical model as well (see Figure 5.18d) but it did not exceed the prior formed shear crack towards the cross beam in size through out the analysis.

No other NLFEA analysis of collapse test 1 is available so we can only verify our results with the collapse test which is done in Figure 5.20 and Table 5.5. The graph shows an underestimation of the stiffness from the start. If we consider Table 5.6 we see that the transverse load spreading in the numerical model is much too low which partly explain the lack of stiffness. The actual load spreading was also investigated by considering the vertical support reaction to the applied load relative to the loaded beam in section 5.2.3. It also showed that the spreading of the load was insufficient represented in the numerical model. This effect became more pronounced with increasing load application. The data of test 1 (see Figure 5.22) demonstrates this effect in the collapse test 1 as well. By comparing the measurements taken at the collapse test with the results of CDCL it also became apparent that the under representation of the lateral load spreading increased moving away from the loaded beam. This makes sense because the spreading of the load was compared to the loaded beam (number 11) and not to the adjacent beam.

However, the collapse load is reached after a deflection 56% greater than collapse test 1 has occurred with a measured strain below the applied load of 104% greater. The 'too late' failure can be explained by the way the prescribed deformation is applied on the mesh of shells. It is the same as in the single beam models of Mustafa[21] with a vertical oriented shell being pushed downward. This way, the punching shear failure of the field test cannot be realized and the analysis will be continued till the second failure mode is activated. Several attempts have been made to perform the analysis by loading a horizontal oriented shell or the use of a quadrilateral load combined with arc length control but were ultimately not successful.

In the two evaluated cross sections an increase in compressive normal force was detected in the longitudinal direction on either side of the loading plate. The left cross section closer to the support showed more than four times the increase than the right cross section. The size of the increase is quite low. However, the lateral restraint can also be provided with the continuous connection through the slab to the adjacent beams allowing for transferring horizontal shear forces. The occurrence of first flexural and then shear cracks allowed for vertical displacement of the loading plate.

Two cross sections in the two adjacent slabs on either side of the loading plate in the transverse were also evaluated for changes in normal force. Only the two closest slabs were loaded in compression and had a very high increase in normal force considering the width of the evaluated strip. No cracking was detected in the transverse direction, but the high amount of lateral restraint combined with the displacement shifting the the neutral axis of the loaded girder upwards we can say the presence of fixed boundary action was detected.

5.4.3. Model CDTL

No comparison to an existing analysis of verification with test data is possible for this model. Most importantly is that the shortcoming of the complete deck, the reduced transverse load distribution, will have a limited effect on the accuracy of the results. In the CDCL model all the load was concentrated at a single location. This is clearly not the case in the CDTL model since uniformly distributed loads are applied and the 12 points loads instead of a single one. The failure by crushing of the concrete in the top flange (see Figure 5.31b) occurs at several locations. Shear cracks do occur in the flanges but the largest cracks are this time in the deck. The load factor of the traffic load at failure of 2.34 proofs that the Vechtbrug was capable of carrying the traffic load defined in the current design codes.

6

Conclusions

To answer the main research question (To which extent can we a simulate the structural behaviour of a prestressed T-beam slab bridge deck using a non-linear finite element model with a 3D non-planar mesh of shell elements?) we compare the results of the performed NLFEA with the results of the respective collapse tests.

IBCL model

- Failure load of NLFEA exceeds field test by 15%
- Max deflection of NLFEA exceeds field test by 18%
- Failure mode of NLFEA in agreement with field test
- Cracking pattern mode of NLFEA in reasonable agreement with field test. The angle of the crack was steeper in the collapse test

CDCL model

- Failure load of NLFEA exceeds field test by 12%
- Max deflection of NLFEA exceeds field test by 56%
- Failure mode of NLFEA in disagreement with field test: punching shear failure is missed
- Cracking pattern mode of NLFEA of the beam's web in reasonable agreement with field test. The switch of the major shear crack from towards the cross beam to towards the support was not done in the numerical analysis.
- The transverse load distribution at the location of the applied load was 22% and 25% lower for the adjacent beams 10 and 12.

We can conclude that the IBCL model yields results approximate to the values of the collapse test and are acceptable from an engineering perspective in practice. However, the CDCL model gave partly inaccurate results. The transverse load distribution capacity was too limited in the numerical model. In addition, missing the punching shear is caused by an inaccurate method of load application resulting in loading the structure past the primary failure mode and overestimating the collapse load.

6.1. What are the benefits of model with a mesh of 3D solids compared to a non-planar mesh of shell elements?

The work of Mustafa [21] and Ensink [12] show that for the IBCL model with a non-planar shell mesh results can be achieved that are equally accurate with respect of maximum deflection and collapse load. However, the IBCL model required the use of a small amount of 3d solid elements to model the end cross beam which was loaded under torsion. That stress state and failure of that beam could not be represented using regular curved shell elements. In addition, both the mentioned models using 3d solid elements showed more accurate and realistic cracking patterns. The shell element lacks some flexibility compared to the 3d solid element which can be remedied by combining the two types of elements in the mesh and only use solid elements where there extra functionality is required.

6.2. What is the structural response of the bridge deck to a full ULS traffic load?

The results of the CDTL model show that collapse occurs after the load exceeds 234,2 % of the prescribed traffic load. The absence of significant damage to the Vechtbrug bridge during an active service life of approximately 60 years with increasing traffic load confirms the accuracy of the outcome of the results and shows the robustness of the design of the bridge deck. According to the report on the field test [10] the type of bridge used in this case study is *analytically found to be insufficient for shear*. Even with the point of application of the load chosen to maximize the shear forces in the structure, it failed in bending with crushing of the concrete of the top flange. The failure mode suggests that the collapse load is probably lower when the axel loads are applied midspan. However, given the results of the performed analyses it is safe to say that the bridge can withstand the ULS traffic load applied at any location.

6.3. What are the effects of transverse load distribution?

The effect of incorrectly modelling the capability for transverse load distribution has a great impact on the load-carrying capacity of the entire structure, especially in the case of concentrated loads. The results show that although FBA was activated in the transverse direction, the transverse distribution was insufficient present. This reduces the load-carrying capacity and by extension the collapse load of the structure.

In both the numerical analysis and collapse test 1 the transverse load distribution reduced with increasing applied load. This can partly be explained by an increased load-carrying capacity of the loaded beam caused by the manifestation of arch action, confinement of the concrete and an small increase in the tensile stress of the steel inside the girder due to hardening.

6.4. Can we demonstrate the presence of confinement, arch action or compressive membrane action?

Confinement

The presence of confinement is easily demonstrated by the values of the principal concrete compressive stress exceeding the maximum compressive concrete stress entered in the material properties (see Table 4.2). The relation between the principal stresses σ_1 and σ_2 for nodes where the confinement effect is active is shown in Figure 5.37. It occurs in all three models.

Arch action/CMA/FBA

The presence of arch action in the IBCL model was detected. A large lateral restraint at the support, crack formation under the loading plate combined with the downward displacement are all indications of activation of the arch action phenomenon. It was also detected in CDCL model, but the increase in normal force was much lower. The lateral restraint was probably generated by the shear forces in the slab between the adjacent girders. In the transverse direction the indicators of fixed boundary action were present in the slabs next to the loading plate. A very large increase in normal force was measured but no cracking in the longitudinal direction in the slab combined with a large downward displacement at the location of the loading plate.

6.5. Future research

The lower transverse load distribution has a major negative impact on the accuracy of the numerical results of this thesis. A numerical analysis of a small part of the structure can be performed with solid cross beams for verification.

Bibliography

[1] D Allaix. *On the application of the Global Resistance Factor (GRF) method*. 2019.

[2] Sana Amir. "Compressive membrane action in prestressed concrete deck slabs". PhD thesis. TU Delft, 2014.

[3] B Belletti et al. "Validation of the guidelines for nonlinear finite element analysis of concrete structures". In: *Part: Reinforced Beams* (2017).

[4] RD de Borst and LJ Sluijs. *Computational Methods in Non-linear Solid Mechanics*. 2013.

[5] D Brandsen. *RTD 1006:2013 Richtlijnen Beoordeling Kunstwerken 1.1*. 2013.

[6] Chris. *Vechtbrug Muiden 1965*. Mar. 2018. URL: https://www.wegenwiki.nl/images/Vechtbrug_Muiden_1965.jpg.

[7] D Den Boef. *Proof loading bridge "Vecht Bridge A1" - Material research concrete compressive strength (in Dutch)*. 2016.

[8] *EN 1991-2 Eurocode 1: Actions on structures - Part 2: Traffic loads on bridges*. 2015.

[9] *EN 1992-1-1 Eurocode 2: Design of concrete structures - Part 1-1: General rules and rules for buildings*. 2011.

[10] SWH Ensink et al. "Full-size field test of prestressed concrete T-beam bridge". In: *European Bridge Conference*. 2018.

[11] Denise Ferreira. *DIANA User's Manual - release 10.4*. 2020.

[12] M. A.N. Hendriks, S. W.H. Ensink, and C. van der Veen. "Non-linear analysis of prestressed concrete t-beams". English. In: *Advances in Engineering Materials, Structures and Systems*. Ed. by Alphose Zingoni. 7th International Conference on Structural Engineering, Mechanics and Computation, 2019 ; Conference date: 02-09-2019 Through 04-09-2019. CRC Press / Balkema - Taylor and Francis Group, 2019, pp. 1360–1365. ISBN: 9781138386969. DOI: 10.1201/9780429426506-235.

[13] Max AN Hendriks, Ane de Boer, and Beatrice Belletti. "Guidelines for nonlinear finite element analysis of concrete structures". In: *Rijkswaterstaat Centre for Infrastructure, Report RTD* (2020), pp. 1016–1.

[14] Max AN Hendriks, Ane de Boer, and Beatrice Belletti. "Validation of the Guidelines for Nonlinear Finite Element Analysis of Concrete Structures Part: Pre-stressed beams". In: *Rijkswaterstaat Centre for Infrastructure, Report RTD* (2017).

[15] Joop van Houdt. *A1 Eemnes-Naarden-Muiderberg,Diemen-Watergraafsmeer*. Apr. 2011.

[16] Shyi-Shing Hsieh, Wai-Fah Chen, and Edward C. Ting. "An Elastic-Fracture Model for Concrete". In: *Engineering mechanics* (1979), pp. 437–440.

[17] J. J. Doorgeest and H. Sliedrecht. *RTD 1006 Richtlijnen Beoordeling Kunstwerken*. 2022.

[18] RT Koekkoek. *Measurement Report Loading of Vechtbrug (25H-100). Stevin Report 25.05-17-03*. Delft University of Technology, Delft, the Netherlands, 2017.

[19] Helmut Kupfer, Hubert K Hilsdorf, and Hubert Rusch. "Behavior of concrete under biaxial stresses". In: *Journal proceedings*. Vol. 66. 1969, pp. 656–666.

[20] Jonna Manie. *DIANA User's Manual 9.4 - release 9.4*. 2010.

[21] Shozab Mustafa. "Analytical and Numerical Study of Arch Action in T-beam Bridges". In: (2019).

[22] "N 1009:1950 nl reinforced concrete requirements gbv 1950". In: (1950).

[23] *NEN EN 1990 Eurocode: Basis of structural design*. 2019.

[24] *NEN EN 1990 Eurocode: Basis of structural design, National Annex*. 2019.

[25] K Palacio. “Practical recommendations for nonlinear structural analysis in DIANA”. In: *TNO DIANA BV, Delft* (2013).

[26] Jörg-Rüdiger Sack and Jorge Urrutia. *Handbook of computational geometry*. Elsevier, 1999.

[27] R G Selby and F J Vecchio. “A constitutive model for analysis of reinforced concrete solids”. In: *Canadian Journal of Civil Engineering* 24.3 (1997), pp. 460–470. DOI: 10.1139/196-135. eprint: https://doi.org/10.1139/196-135. URL: https://doi.org/10.1139/196-135.

[28] “Voorschriften voor het Ontwerpen van Stalen Bruggen (VOSB 1963)”. In: (1963).